METAL-MODIFIED TANSITION METAL CARBIDES FOR ELECTROCHEMICAL APPLICATIONS

Qian Zhang

Submitted in partial fulfillment of the requirements for the degree of Doctor of Philosophy

in the Graduate School of Arts and Sciences

COLUMBIA UNIVERSITY

2018

ABSTRACT

Metal-Modified Transition Metal Carbides for Electrochemical Applications

Qian Zhang

Proton exchange membrane or anion exchange membrane water electrolyzers and fuel cells are still expensive for large-scale commercialization. It requires more investigation and research on finding more economical and efficient electrocatalysts for reactions in these devices. This thesis investigates the performance of metal-modified transition metal carbides on hydrogen evolution reaction (HER) and ethanol oxidation reaction (EOR). The catalysts screening principles for HER and EOR in acid and alkaline are examined and developed by correlating density functional theory (DFT) calculations with experimental results.

Metal-modified transition metal carbides can reduce the amount of platinum group metals required for HER, but it is unclear what descriptors are relevant for these materials for the HER under alkaline conditions. Several transition metal carbides (Mo_2C, NbC, TaC, WC, VC) thin films were synthesized and modified with monolayers of platinum or gold. The experimentally measured HER exchange current densities were compared with DFT calculations of adsorbed hydrogen and hydroxyl binding energies. The plot of HER activity versus hydrogen binding energy showed a volcano shape for catalysts in both acid and alkaline electrolytes, but the hydroxyl binding energy did not form a strong correlation with alkaline HER activity.

Relatively high surface area molybdenum carbide (Mo_2C) particles was modified with 5 wt % silver, copper, nickel, platinum, and palladium and subsequently assessed for their HER activity in alkaline and acid electrolytes. DFT-calculated hydrogen binding energies predicted

that Pt–Mo_2C and Pd–Mo_2C should be most active, which was confirmed with experimental results. Similar activity trends were observed at both high and low pH values, with Cu/Mo_2C being the least active. X-ray photoelectron spectroscopy (XPS) confirmed that metal particles remained on the sample before and after HER testing. Pt-modified nanocrystalline Mo_2C showed superior HER activity compared with Pt-modified commercial Mo_2C, making it a potential replacement for bulk Pt in alkaline membrane electrolyzers. The positive effect on the HER activity of the metal contact with non-passivated Mo_2C surfaces was also demonstrated.

Ethanol is an ideal fuel in low-temperature fuel cells. The EOR on platinum-modified tantalum carbide (TaC) was investigated using both model thin films and powder catalysts. The results demonstrated that the 1.5 wt% Pt-modified TaC catalyst obtained enhanced EOR activity compared to Pt. *In-situ* infrared reflection absorption spectroscopy (IRRAS) study revealed that the Pt surface was less poisoned by EOR intermediates and a higher CO_2 selectivity (7~9%) was achieved on the 1.5 wt% Pt/TaC catalyst, compared to the 40 wt% Pt/C. DFT calculations revealed that the binding energies of EOR intermediates on the Pt/TaC(111) surface a weaker than on Pt(111), suggesting an enhanced poison-tolerance from the adsorption of these intermediates. The combined experimental and theoretical investigations strongly suggested that Pt/TaC should be a promising electrocatalyst for EOR.

Palladium-modified tungsten carbide (Pd/WC) as an efficient catalyst was investigated for EOR through combined DFT, surface science and electrochemical measurements. Compared to the Pd(111) surface, DFT calculations suggested that the Pd/WC(0001) surface should be less poisoned by the ethanol decomposition intermediates, consistent with surface science results that desorption temperatures of the detected intermediates were lower on the Pd/WC surface. Electrochemical evaluation coupled with *in-situ* IRRAS measurements of 5 wt% Pd/WC/C

powder catalysts were then conducted. The EOR activity of the 5 wt% Pd/WC/C-op catalyst synthesized by the one-pot (op) method was noticeably enhanced, compared to the benchmark 40 wt% Pd/C and 5 wt% Pd/WC/C-iwi that was synthesized using a conventional incipient wetness impregnation (iwi) method. The IRRAS results showed that the EOR products were detected at a lower onset potential on 5 wt% Pd-WC/C-op than on 40 wt% Pd/C.

Overall, results from the current thesis demonstrated the feasibility of using metal-modified transition metal carbides as lower-cost and more efficient electrocatalysts for HER and EOR. These results identified descriptors that can be potentially used to design more cost-effective catalysts. Furthermore, results from this thesis also revealed the general similarities and differences of the activity and stability of carbide-based catalysts in acid and alkaline electrolytes.

TABLE OF CONTENTS

LIST OF FIGURES

LIST OF TABLES

ACKNOWLEDGEMENT

The most important person that I would love to give all my gratitude and appreciation to is my research advisor, Dr. Jingguang G. Chen. His extensive knowledge of catalysis has been instrumental in the pursuit of my research projects during my graduate studies. His patient and consistent efforts in providing detailed feedback on my research and writing have allowed me to learn from my own mistakes and have compelled me to be a better researcher and academic writer. He has always been there to provide constructive and strategic guidance on my work. He not only taught me how to do research, but also taught me how to be a better professional with higher work ethics. Other than being my research advisor, Dr. Chen has also been a caring mentor who has provided me with valuable advice for my career development. I know with certainty without his guidance and support during my graduate studies, it would not have been possible to make it this far.

I owe thanks to my curriculum advisor Dr. Ngai Yin Yip for providing logistical support, curriculum guidance during my graduate studies, and for writing feedback on my thesis. I would also like to thank Dr. Robert Farrauto, Dr. Ah-Hyung (Alissa) Park and Dr. Elizabeth J. Biddinger for serving on my thesis defense committee.

My dear colleagues in Dr. Chen's group have provided me with their wonderful assistance and we have established life-long friendship. I have had very intellectually-provoking interactions with Lea Winter, Elaine Gomez, Zhexi Lin and Weiming Wan. I want to specifically thank Brian Tackett for teaching me experimental techniques and assistance on experiments trouble-shooting and data interpretations. I also want to give credits to Dr. Zhao Jiang and Dr.

Shyam Kattel for their DFT calculations assistance. I am very grateful all of my colleagues for their open mindedness and for the life-long friendship that we have stablished.

Finally, I owe a palpable debt of gratitude to my family. I thank my mom and dad for their unconditional love and guidance. I also want to thank my boyfriend, Shahab Hadaegh, for his enormous encouragement and support along the way.

1. INTRODUCTION

1.1 Background of water electrolysis

1.1.1 Opportunities of water electrolysis

Exponentially increasing demand for energy, continued depletion of fossil fuel resources and rising environmental costs from ongoing dependence on fossil fuel-based energy have stimulated the development of alternative energy resources.[1–3] According to the International Energy Agency (IEA), solar energy capacity, as one of the renewable energy source, is expected to increase by approximately 1,200 gigawatts by 2040 and will account for one-fourth of global energy capacity.[4]Water electrolysis has been given tremendous attention for energy storage purposes.[5–9] It offers a unique opportunity for alleviating intermittency issues associated with renewable energy sources by converting excess renewable energy-generated electricity into storable hydrogen.[5–8]

At grid-scale, water electrolyzers-coupled power supply systems enhance the flexibility in the form of dispatchable power generation, electricity demand, and supply management.[10] The excess electricity, generated during periods of peak solar radiation, can be converted into electrolytic hydrogen instead of being curtailed. In the evening, the stored hydrogen can be converted back to electricity through hydrogen fuel cells.[11] At the distributed electricity generation level, water electrolyzers, coupled with solar power generation systems, promotes an individual household's autonomy from the electricity grid.

Lithium ion batteries serve as an alternative energy storage device with prices currently fifteen time cheaper than water electrolyzers and fuel cells[12]. However, batteries become less economically viable for larger-scale energy storage purposes because storage capacity is proportionally related to the size of the battery unit. Alternatively, storing excess energy in the

form of H_2 in a pressurized tank can be easily scalable by increasing gas pressure. Even at STP, the gravimetric energy density of lithium ions battery is more than 100 times lower compared to hydrogen energy density.[13]

Other than for energy storage purposes, hydrogen production from water electrolysis is more attractive for a large-scale use because the generated hydrogen is carbon-free and does not require gas separations. Unlike hydrocarbon steam reforming as the conventional industrial method for hydrogen production, hydrogen generated from centralized renewable energy through water electrolysis reduces the dependency on fossil fuel consumption and thus accelerates the carbon-free H_2 production process.[14] Moreover, the process is less energy intensive because gas separation in water electrolysis essentially requires no energy input.[15]

1.1.2 Fundamentals of water electrolysis

As shown in Fig. 1.1, there are two types of water electrolysis cells, acid polymer electrolyte membrane (PEM) water electrolysis cells and alkaline anionic exchange membrane (AEM) electrolysis cells. PEM water electrolysis cells are currently more technologically matured than alkaline anionic exchange membrane (AEM) electrolysis cells.[7,16] The hydrogen evolution reaction (HER), as a half reaction, occurs at the cathode by accepting electrons while oxygen evolution reaction (OER) occurs at the anode by producing and giving away electrons. The cathode and the anode are separated by a membrane. The membranes are sandwiched by anodic and cathodic catalyst layers followed by diffusion layers. The half-reactions are different, depending on the membrane type, as shown in Fig. 1.1.

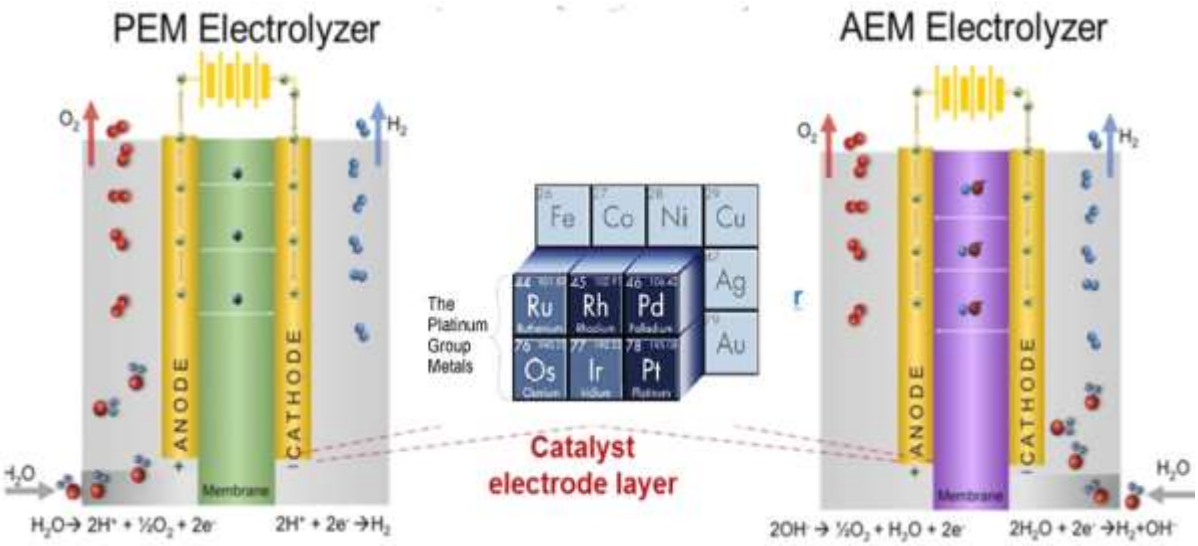

Figure 1.1 Acid polymer electrolyte membrane (PEM) water electrolysis cells (left) and alkaline anionic exchange membrane (AEM) water electrolysis cells (right).[17] HER and OER reactions for PEM and AEM cells are embedded. State-of-the-art electrocatalysts used in cells are primarily scarce and expensive platinum group metals.

Thermodynamically, water electrolysis is a non-spontaneous reaction because the change in Gibbs free energy is positive as shown in Fig. 1.2.

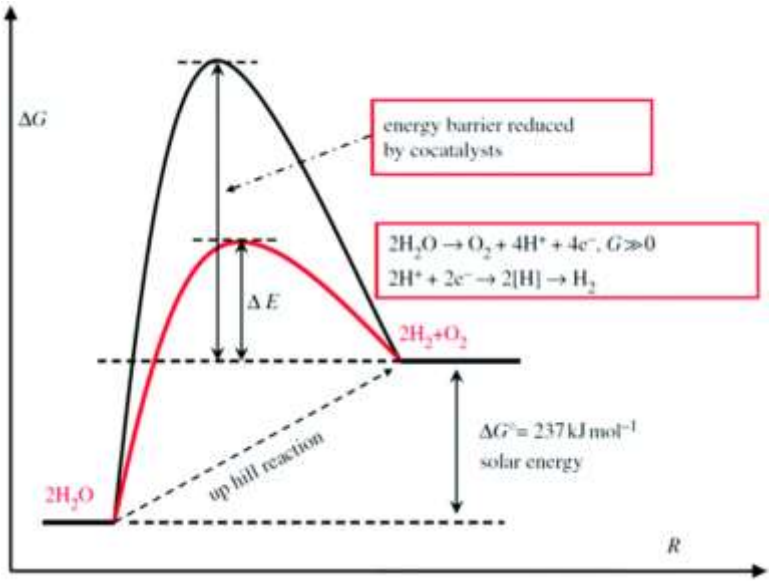

Figure 1.2 Schematic illustration of water electrolysis reaction energetics.

At standard temperature and pressure (STP), under thermodynamic equilibrium condition, the water electrolysis reaction requires 1.23 V, namely the reversible voltage (V_{rev}). However, to

achieve reasonable kinetics in water electrolysis cells for the commercial purpose, the actual energy consumption is usually greater than 1.23 V due to additional overvoltage, which is also often termed overpotential. Expressively, the electrolysis cell voltage (V_{cell}) is the sum of the reversible voltage and the additional overvoltage, shown below[10]:

$$V_{\text{cell}} = V_{\text{rev}} + V_{\text{ohm}} + V_{\text{act}} + V_{\text{con}},$$

where V_{ohm} is the overvoltage caused by ohmic losses due to the resistance of cell elements to the electrons flow, which is proportional to the electric current that flows through the cell. V_{act}, known as activation overvoltage, is the voltage required to overcome the energy barrier that the charge has to overcome to go from the reactants to the electrodes and vice versa. V_{act} depends on the catalytic performance of the catalysts. As shown in Fig. 1.2, a better catalyst will have lower V_{act}, which reduces the V_{cell} energy input and thus enhances the efficiency of the electrolysis cells. V_{con}, concentration overvoltage, is mainly caused by mass transport and is insignificant, relative to V_{rev} and V_{act}, in a chemically controlled regime.

1.1.3 Challenges for water electrolysis

Scarcity and high costs associated with materials for electrocatalysis are hurdles for commercial viability of these cells. State-of-the-art electrocatalysts used in cells are primarily scarce and expensive platinum (Pt) group metals (PGM), as shown in Fig. 1.1. If the targeted storage for 1200 gigawatts of solar energy target is fulfilled by water electrolysis by 2040, it will require 50% of total global consumption of IrO_2 (3 ton/year) as the anodic OER catalyst and significant amount of Pt (1.8 ton/year).[18] Therefore, to render water electrolysis and fuel cells scalable and economically viable, PGM loadings in these devices must be reduced.

Specifically, for cathodic HER reaction in water electrolysis cells, standard support for Pt electrocatalysts is Vulcan carbon, which is prone to be less stable in electrochemical reaction conditions and thus results in detachment of deposited PGM. The difference in electronic structure and chemical property between Pt and Vulcan carbon leads to the weak interaction between Pt and carbon, causing the PGM particles to undergo agglomerations during the reaction, so required PGM loadings on Vulcan carbon are very high.[19] Therefore, more stable catalysts have to be investigated and developed in these cells.

1.2 Identification of HER research objectives

The similar electronic structures between early transition metal carbides (TMCs) and Pt offer a unique opportunity to reduce Pt loadings and enhance Pt stability[20]. Also, TMCs are three orders of magnitude more abundant thus inexpensive.[21] Our group achieved similar acid HER activity for Pt monolayer-modified TMC compared to Pt bulk. In acid, on model thin films surfaces, the monolayer coverage represents approximately 95% reduction of Pt loading. The investigated TMCs for acid HER include tungsten carbides (WC and W_2C), molybdenum carbide (Mo_2C) and niobium carbide (NbC).[22] Moreover, the calculated hydrogen binding energy (HBE) for those carbides and the metal-modified carbides was found to closely correlate in a volcano-shape with acid HER activity for metal-modified TMCs thin films[18], indicating that HBE is an effective descriptor for acid HER activity.

However, Pt-like HER activity was mainly demonstrated on low surface area TMC thin film samples. It is important to expand these findings to industrially relevant high surface area powder catalysts. Therefore, the HER project in this thesis is dedicated to synthesizing high surface area metal-modified molybdenum carbide (Mo_2C) powder catalysts and correlating their

HER activity with their respective calculated HBE. The following questions are addressed in this project:

1) By how much do the high surface area powder Mo_2C reduce the Pt loadings?
2) For the purpose of investigating non-PGM catalysts, are there any non-PGM showing promising HER activity?
3) Is the HER activity trend for different metal-modified Mo_2C powder catalysts closely correlated with predicted results from DFT calculations?
4) How should we use DFT as a screening tool to predict HER activity for powder catalysts?

While acid HER is catalyzed by acceptably small loadings of Pt, water electrolysis at low pH is critically hindered by the requirement for expensive IrO_x catalysts for the oxygen evolution reaction (OER). In alkaline, OER is readily catalyzed by many non-precious metal oxides, notably Fe and Ni compounds.[23,24] However, in alkaline electrolyte, a state-of-the-art electrolyzer requires a twenty times higher Pt loading in order to match the OER reaction rate. It is therefore essential, from both fundamental and economic perspectives, to determine effective descriptor for alkaline HER activity as a fast screening tool for finding novel alkaline HER catalysts.

The HBE value is widely accepted as an effective descriptor for predicting acid HER activity.[18] However, due to the difference in reaction mechanisms for acid and alkaline HER, it is still under debate as to whether HBE is the sole descriptor for alkaline HER activity. Many argue that the hydroxyl group also plays an essential role in determining alkaline HER activity.[25–28] In order to provide insight into this debate and determine effective descriptor for alkaline HER, the second HER project primarily investigates the correlation between alkaline HER activity and HBE and hydroxyl binding energy (OHBE).

In this project, several types of metal-modified TMC thin films were synthesized and tested for their HER activity. Both HBE and OHBE on the examined catalytic surfaces were calculated by DFT. In this project, the questions listed below are addressed:

1) In acid, do HBE and experimental acid HER activity results for Pt- and Au-modified TaC and VC adhere to the established volcano plot?
2) In alkaline, is HBE or OHBE a more effective descriptor for alkaline HER activity based on the correlation between experimental results and DFT calculations for Pt and Au-modified TMCs?

1.3 Background of direct alcohol fuel cells (DAFC)

1.3.1 Opportunities of DAFC

H_2 is one of the energy carriers that can be produced from water electrolysis. However, according to Fig. 1.3, among all listed energy carriers, H_2 contains the lowest volumetric energy density, which prevents the gaseous H_2 from being practical. In order to make H_2 storable and transportable, H_2 must be compressed or cryogenically cooled. These extra processes are costly and impose safety concerns. Alternatively, small-chain alcohols (methanol and ethanol), containing higher volumetric energy density, are a liquid form at STP, which can be easily stored and transported. Also, oxygenates are more commercially favored due to their competitive market prices arising from mass production of non-fossil biomass[29–31] and their compatibility with the existing storage and transportation infrastructure[32]. Ethanol contains higher specific energy density by volume and is non-toxic when, compared to its competing fuel, methanol.

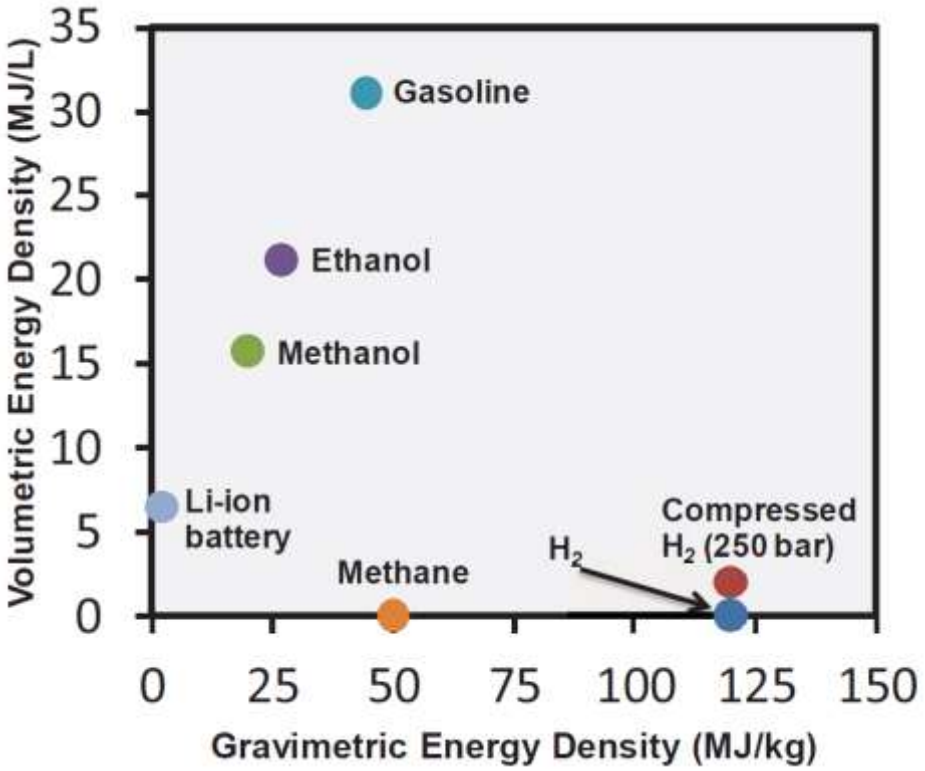

Figure 1.3 Comparison of gravimetric and volumetric energy density at standard temperature and pressure (STP) for various energy carriers.[13,33]

1.3.2 Fundamentals of DAFC for electrical energy generations

Fuel cells convert chemical energy into electrical energy for electricity generation through the electrochemical process while electrolyzers are opposite, consuming electrical energy and converting them into chemical molecules. The reactions occur in direct alcohol fuel cells (DAFC) as shown below:

$$CH_3CH_2OH + 3H_2O \rightarrow 2CO_2 + 12H^+ + 12e^- \qquad E_a^o = 0.085\ \text{V } vs.\ \text{SHE} \tag{1}$$

$$3O_2 + 12H^+ + 12e \rightarrow 6H_2O \qquad E_c^o = 1.229\ \text{V } vs.\ \text{SHE} \tag{2}$$

$$CH_3CH_2OH + 12OH^- \rightarrow 2CO_2 + 9H_2O + 12e^- \quad E_a^o = -0.74\ \text{V } vs.\ \text{SHE} \tag{3}$$

$$3O_2 + 6H_2O + 12e^- \rightarrow 12OH^- \qquad E_c^o = 0.40\ \text{V } vs.\ \text{SHE} \tag{4}$$

$$CH_3CH_2OH + 3O_2 \rightarrow 2CO_2 + 3H_2O \quad E^o = 1.14\ \text{V} \quad E_{eq}^{\circ} = E_{O_2}^{\circ} - E_{\text{alcohol}}^{\circ} \tag{5}$$

Where Eq. (1) and (2) occur in acid PEM DAFC while Eq. (3) and (4) are in alkaline AEM DAFC. The anodic half reactions, shown in Eq. (1) and (3), are ethanol oxidation reactions (EOR). Cathodic half reactions, Eq. (2) and (4), are oxygen reduction reactions (ORR). The overall reaction for DEFC is shown in Eq. (5) where SHE stands for standard hydrogen electrode. My research primarily focuses on EOR.

It is worth noting that the reaction, shown in Eq. (5), undergoes a total oxidation (C1) reaction pathway through a C-C bond breakage. In this pathway the consumption of one mole of ethanol produces twelve moles of electrons, which is considered as the most efficient reaction pathway. Unlike the total oxidation reaction pathway, ethanol primarily undergoes partial oxidation (C2) reaction pathways, in which only two or four moles of electrons are produced by consuming one mole of ethanol.

1.3.3 Challenges for DAFC

Pt-based catalysts are the most promising catalysts for alcohol electro-oxidation due to their high activity.[3] Other than scarcity and poor stability of conventional Pt/C[34], one of the major limitations for DAFC from being commercialized is the slow anodic kinetics of EOR resulting from Pt/C at low potentials. The reversible potential for EOR is approximately 0 V vs.

SHE and are governed by reaction thermodynamics. However, the kinetics are extremely low until the applied potentials are above 0.7 V (vs RHE).[35,36] This is because adsorbed intermediates of CO and carbonyl groups from ethanol decompositions bind to Pt active sites strongly at low potentials, causing Pt sites deactivations.[37]

Additionally, it is widely accepted that the presence of the oxygen-donating group, O and OH, in the vicinity of Pt sites facilitates the regeneration of poisoned sites by oxidizing adsorbed intermediates from ethanol decomposition. However, Pt is not active for generating oxygen donating groups (-O and -OH) at low potentials.[38] Nevertheless, at high potentials (> 0.7 V), selectivity towards the highest efficient C1 reaction pathways are extremely low, accounting for 2 ~ 3%. Therefore, Pt surface poisoning by CO and carbonyl intermediates, the inability of generating oxygen donating groups at low potential, and low selectivity towards the highest efficiency reaction pathways ultimately result in low voltage output and thus low efficiency for DAFC.

Confronted with these challenges, the designed catalytic surface should result in lower binding energy of CO and carbonyl intermediates, higher capacity for oxygen donating groups generations and higher selectivity towards the highest efficient reaction pathway. TMCs has been shown to have strong electron-affinity.[39] When Pt is deposited on TMCs, the presence of TMCs could potentially reduce the electron density of Pt. Pt-modified tungsten monocarbide (WC) catalyst was reported to be more resistant toward CO poisoning.[40–43] In order to enhance the capacity of generating the oxyen-donating species in the vicinity of the Pt sites, a second metal as the promotor for Pt, typically Ru or Sn, is introduced[44]. Alternatively, TMCs could be potentially considered as an oxophilic promotor because they have been reported to be thermodynamically favored for the formation of oxygen donating species[45]. Also, many groups

have investigated Pd -based[1,3,29,46,47] catalysts to enhance the EOR activity through a bifunctional mechanism by modifying Pd with other substrates and promotors. Among them, tungsten carbides (WC) -supported Pd has shown enhanced poisonous intermediate tolerance[48] for the methanol oxidation reaction[49].

Many studies have also investigated palladium (Pd) [1,50–52] catalysts as an alternative for Pt because Pd has a similar electronic structure as Pt but with one-fiftieth the cost.[1,51,53] Therefore, it is important to investigate whether Pd-modified WC is active towards EOR. Moreover, under the fast development of anion exchange membrane applied to alkaline electrolyte (high pH) fuel cells, investigating stable TMC in both acid and alkaline environment for EOR is essential. Unmodified TaC, as one of another TMC, was chosen for EOR study due to its high stability at its required potential in high pH ranges.[54]

1.4 Identification of EOR research objectives

Therefore, one of my EOR projects investigates the activity and stability of Pt-modified TaC on EOR in both acid and alkaline electrolyte. The following research questions are aimed to be answered:

1) Whether the Pt-modified TaC thin film and power catalysts show enhanced activity and stability relative to Pt?

2) What are the underlying explanations for enhanced EOR activity through *in-situ* infrared experiments and theoretical DFT calculations?

3) Based on experimental results and theoretical calculations, can intermediates binding energy from ethanol decomposition be used as effective descriptors for predicting EOR activity based on experimental results and theoretical calculations?

Based on identified EOR descriptors from the first EOR project, for my second EOR project, preliminary DFT calculations were conducted, suggesting palladium (Pd)-modified WC might be more active toward EOR than Pd. The calculated results were further supported by surface science experiments on single crystal samples. Therefore, Pd-modified WC power catalysts were then synthesized and examined for EOR. The research questions are as follows:

1) Can Pd-modified WC be considered as a promising EOR catalysts based on DFT calculations of effective EOR descriptors identified in the first EOR research project?
2) Does DFT calculations results are further supported by the surface science experiment results?
3) Whether synthesized Pd-modified WC powder catalyst shows enhanced EOR activity as suggested by DFT and surface science results?
4) By employing *in-situ* infrared experiment on powder catalyst, what mechanistic explanations can be revealed for enhanced EOR activity for Pd-modified WC?

1.5 Thesis scope and structure

The thesis consists of seven chapters beginning with the Introduction as chapter one. Chapter two describes the overall research methodology and experimental procedure used for the research including 1) synthesis techniques for making thin films and powder catalysts, 2) characterization techniques, 3) electrochemical measurements including *in-situ* infrared techniques and 4) surface science experimental techniques. Theoretical DFT calculations method is also discussed. Chapters three and four describe two projects for HER while Chapters five and six focuses on EOR. The main research questions and project objectives are described in their corresponding sections outlined above.

In general, Chapter three extends low surface area thin films to high surface area power catalysts for metal-modified Mo_2C. Five different metal-modified Mo_2C powder catalysts are synthesized and tested for HER activity in both acid and alkaline. Chapter four primarily investigates whether HBE would be an effective and sole descriptor for HER in alkaline. Unmodified TaC, Mo_2C, VC, WC and NbC thin films and their Pt or Au-modified ones are synthesized and tested for alkaline HER activity; both HBE and OHBE are calculated by DFT. The correlation between the calculated HBEs and OHBEs with their alkaline HER activity (i_o) are established to address the research questions.

Chapters five and six explore applications of metal-modified TMC for EOR. Chapter five investigates the activity and stability of Pt-modified TaC in both thin film and power forms for EOR. Chapter six describes theoretical predictions and experimental investigations of Pd-modified WC for EOR in alkaline.

Chapter 7 summarizes key findings and main contributions of my research work. A new direction for exploring transition metal nitride (TMN) is suggested, and preliminary results are illustrated to show feasibility of using TMNs for many electrochemical applications.

References

(1) Akhairi, M. A. F.; Kamarudin, S. K. *Int. J. Hydrogen Energy* **2016**, *41* (7), 4214–4228.

(2) Beyhan, S.; Coutanceau, C.; Léger, J.-M.; Napporn, T. W.; Kadırgan, F. *Int. J. Hydrogen Energy* **2013**, *38*, 6830–6841.

(3) Wang, Y.; Zou, S.; Cai, W.-B. *Catalysts* **2015**, *5* (3), 1507–1534.

(4) Energy Agency, I. *www.iea.org/t&c/* **2016**.

(5) Zeng, M.; Li, Y. *J. Mater. Chem. A* **2015**, *3* (29), 14942–14962.

(6) Lehner, M.; Tichler, R.; Steinm?ller, H.; Koppe, M. Springer International Publishing,

2014; pp 7–17.

(7) Carmo, M.; Fritz, D. L.; Mergel, J.; Stolten, D. *Int. J. Hydrogen Energy* **2013**, *38* (12), 4901–4934.

(8) Carmo, M.; Fritz, D. L.; Rgen Mergel, J.; Stolten, D. *Int. J. Hydrogen Energy* **2013**, *38*, 4901–4934.

(9) GRIGORIEV, S.; POREMBSKY, V.; FATEEV, V. *Int. J. Hydrogen Energy* **2006**, *31* (2), 171–175.

(10) Ursua, A.; Gandia, L. M.; Sanchis, P. *Proc. IEEE* **2012**, *100* (2), 410–426.

(11) Edwards, P. P.; Kuznetsov, V. L.; David, W. I. F.; Brandon, N. P. *Energy Policy* **2008**, *36* (12), 4356–4362.

(12) *INTERNATIIONAL ENERGY AGENCY* **2017**, *www.iea.or*.

(13) Etacheri, V.; Marom, R.; Elazari, R.; Salitra, G.; Aurbach, D. *Energy Environ. Sci.* **2011**, *4* (9), 3243.

(14) H2 Scale, D. of E. *Dep. Energy* **2017**, https://www.energy.gov/eere/fuelcells/h2-scale.

(15) Barelli, L.; Bidini, G.; Gallorini, F.; Servili, S. *Energy* **2008**, *33* (4), 554–570.

(16) Barbir, F. *Sol. Energy* **2005**, *78* (5), 661–669.

(17) Varcoe, J. R.; Atanassov, P.; Dekel, D. R.; Herring, A. M.; Hickner, M. A.; Kohl, P. A.; Kucernak, A. R.; Mustain, W. E.; Nijmeijer, K.; Scott, K.; Xu, T.; Zhuang, L. *Energy Environ. Sci.* **2014**, *7* (10), 3135–3191.

(18) Tackett, B. M.; Sheng, W.; Chen, J. G. *Joule* **2017**, *1*, 1–4.

(19) Shao-Horn, Y.; Sheng, W. C.; Chen, S.; Ferreira, P. J.; Holby, E. F.; Morgan, D. *Top. Catal.* **2007**, *46* (3–4), 285–305.

(20) Levy, R. B.; Boudart, M. *Science (80-.).* **1973**, *181* (4099), 547–549.

(21) Hurd, A. J.; Kelley, R. L.; Eggert, R. G.; Lee, M.-H. *MRS Bull.* **2012**, *37* (4), 405–410.

(22) Esposito, D. V.; Hunt, S. T.; Kimmel, Y. C.; Chen, J. G. *J. Am. Chem. Soc.* **2012**, *134* (6), 3025–3033.

(23) Trotochaud, L.; Young, S. L.; Ranney, J. K.; Boettcher, S. W. *J. Am. Chem. Soc.* **2014**, *136* (18), 6744–6753.

(24) McCrory, C. C. L.; Jung, S.; Peters, J. C.; Jaramillo, T. F. *J. Am. Chem. Soc.* **2013**, *135* (45), 16977–16987.

(25) Li, J.; Ghoshal, S.; Bates, M. K.; Miller, T. E.; Davies, V.; Stavitski, E.; Attenkofer, K.; Mukerjee, S.; Ma, Z.-F.; Jia, Q. *Angew. Chemie Int. Ed.* **2017**.

(26) Sheng, W.; Zhuang, Z.; Gao, M.; Zheng, J.; Chen, J. G.; Yan, Y. *Nat. Commun.* **2015**, *6*, 5848.

(27) Durst, J.; Siebel, A.; Simon, C.; Hasché, F.; Herranz, J.; Gasteiger, H. A. *Energy Environ. Sci.* **2014**, *7* (7), 2255.

(28) Intikhab, S.; Snyder, J. D.; Tang, M. H. *ACS Catal.* **2017**, 8314–8319.

(29) Moraes, L. P. R.; Matos, B. R.; Radtke, C.; Santiago, E. I.; Fonseca, F. C.; Amico, S. C.; Malfatti, C. F. *Int. J. Hydrogen Energy* **2016**, *41* (15), 6457–6468.

(30) Rousseau, S.; Coutanceau, C.; Lamy, C.; Léger, J.-M. *J. Power Sources* **2006**, *158* (1), 18–24.

(31) Xuan, J.; Leung, M. K. H.; Leung, D. Y. C.; Ni, M. *Renew. Sustain. Energy Rev.* **2009**, *13* (6), 1301–1313.

(32) Mahoney, E. G.; Sheng, W.; Cheng, M.; Lee, K. X.; Yan, Y.; Chen, J. G. *J. Power Sources* **2016**, *305*, 89–96.

(33) Thomas, G. *Annu. Rev.* **2000**, https://www1.eere.energy.gov/hydrogenandfuelcells/.

(34) Alonso, E.; Field, F. R.; Roth, R.; Kirchain, R. E. In *2009 IEEE International Symposium on Sustainable Systems and Technology*; IEEE, 2009; pp 1–6.

(35) Mellinger, Z. J.; Weigert, E. C.; Stottlemyer, A. L.; Chen, J. G. *Electrochem. Solid-State Lett.* **2008**, *11* (5), B63.

(36) Colmati, F.; Tremiliosi-Filho, G.; Gonzalez, E. R.; Berná, A.; Herrero, E.; Feliu, J. M. *Faraday Discuss.* **2008**, *140*, 379-97-37.

(37) Li, M.; Cullen, D. A.; Sasaki, K.; Marinkovic, N. S.; More, K.; Adzic, R. R. *J. Am. Chem. Soc.* **2013**, *135* (1), 132–141.

(38) Du, W.; Wang, Q.; LaScala, C. A.; Zhang, L.; Su, D.; Frenkel, A. I.; Mathur, V. K.; Teng, X. *J. Mater. Chem.* **2011**, *21* (24), 8887.

(39) Cui, G.; Shen, P. K.; Meng, H.; Zhao, J.; Wu, G. *J. Power Sources* **2011**, *196* (15), 6125–6130.

(40) Weigert, E. C.; Stottlemyer, A. L.; Zellner, M. B.; Chen, J. G. *J. Phys. Chem. C* **2007**, *111* (40), 14617–14620.

(41) Kelly, T. G.; Chen, J. G. *Chem. Soc. Rev.* **2012**, *41* (24), 8021.

(42) Stottlemyer, A. L.; Liu, P.; Chen, J. G. *J. Chem. Phys.* **2010**, *133* (10), 104702.

(43) Kelly, T. G.; Stottlemyer, A. L.; Yang, X.; Chen, J. G. *J. Electrochem. Soc.* **2014**, *161* (8), E3165–E3170.

(44) Wang, Q.; Sun, G. Q.; Jiang, L. H.; Xin, Q.; Sun, S. G.; Jiang, Y. X.; Chen, S. P.; Jusys, Z.; Behm, R. J. *Phys. Chem. Chem. Phys.* **2007**, *9* (21), 2686.

(45) Hwu, H. H.; Chen, J. G. *Chem. Rev.* **2005**, *105* (1), 185–212.

(46) Abdel Hameed, R. M. *J. Colloid Interface Sci.* **2017**, *505*, 230–240.

(47) Qin, Y.-H.; Xiong, Z.-Y.; Ma, J.; Yang, L.; Wu, Z.; Feng, W.; Wang, T.-L.; Wang, W.-G.;

Wang, C.-W. *Int. J. Hydrogen Energy* **2017**, *42* (2), 1103–1112.

(48) Mellinger, Z. J.; Weigert, E. C.; Stottlemyer, A. L.; Chen, J. G. *Electrochem. Solid-State Lett.* **2008**, *11* (5), B63.

(49) Mellinger, Z. J.; Kelly, T. G.; Chen, J. G. *ACS Catal.* **2012**, *2* (5), 751–758.

(50) Zhou, Z.-Y.; Wang, Q.; Lin, J.-L.; Tian, N.; Sun, S.-G. *Electrochim. Acta* **2010**, *55* (27), 7995–7999.

(51) Shen, P. K.; Xu, C. *Electrochem. commun.* **2006**, *8* (1), 184–188.

(52) Fang, X.; Wang, L.; Shen, P. K.; Cui, G.; Bianchini, C. *An in situ Fourier transform infrared spectroelectrochemical study on ethanol electrooxidation on Pd in alkaline solution*; 2010; Vol. 195.

(53) Antolini, E.; Cooper, B. H.; Trejo, J. M.; Mariscal, R.; Fierro, J. L. G.; Xin, Q.; Kwak, C.; Akins, D. L. *Energy Environ. Sci.* **2009**, *2* (9), 915.

(54) Kimmel, Y. C.; Xu, X.; Yu, W.; Yang, X.; Chen, J. G. *ACS Catal.* **2014**, *4* (5), 1558–1562.

2. RESEARCH METHODOLOGY AND EXPERIEMTNAL PROCEDURE

DFT calculations determine adsorbate binding energies of key chemical species on TMN surfaces, known to describe activity for HER and EOR. These values are called descriptors. The experimental observations and the DFT calculations are compared to create a trend between descriptors and activity. These types of correlations are used to guide research and discovery of new catalysts by identifying the optimal value for descriptors and using computation to search for materials that are close to that value.

Theoretical DFT calculation results can be better correlated with experimental data performed on ideal surfaces, single crystals and low surface area (LSA) thin films. Single crystal transition metal carbides (TMC) surfaces and metal-modified TMC are synthesized and examined by surface science experiments in the ultra-high vacuum (UHV) condition including UHV temperature programmed desorption (TPD) and high-resolution electron energy loss

spectroscopy (HREELS). DFT theoretical calculation results can be directly correlated and supported with surface science results, providing insights on reaction mechanisms and predictions on catalysts' activity for the reaction of interest.

LSA thin films of TMC and atomic thickness metal-modified TMC are synthesized by using tube furnace and physical vapor deposition (PVD) in the UHV chamber. Thin film samples are characterized by X-ray diffraction (XRD), X-ray photoelectron spectroscopy (XPS) and scanning electron microscope (SEM). The LSA thin films with well-controlled surfaces are investigated with electrochemical testing. Experimental results performed on LSA thin films are used to correlate with descriptors calculated by DFT. The correlation can determine whether the calculated descriptor is effective for governing activity of a reaction (in this case, the reaction is hydrogen evolution reaction). Once the effective descriptor is found, the preliminary catalyst screening can be done in a more efficient and effective way by the computer.

If preliminary data collected from ideal surfaces are promising, industrially relevant powder electrocatalysts are also synthesized and tested. Three powder synthesis techniques have been employed in my work and XRD, XPS and transmission electron microscope (TEM) were used to characterize the powder catalysts. *In-situ* infrared reflection absorption spectroscopy (IRRAS) on powder catalysts are used to provide the in-depth mechanistic explanation for observed enhanced activity.

2.1 Synthesis technique

Synthesis techniques employed in my research are categorized into two sections. The first section covers the synthesis methods for making LSA TMC and metal-modified TMC thin films. The second section focuses on synthesis techniques for making high surface area TMC and metal-modified TMC powder catalysts.

2.1.1 Thin film synthesis

2.1.1.1 Low surface area TMC thin films synthesis

Transition metals foils, such as tungsten (W), tantalum (Ta), molybdenum (Mo), niobium (Nb) and vanadium (V), are used for carbides thin films synthesis. Upon rinsing samples with DI water to remove surface grease and impurities, the foils samples are inserted into a quartz tube and connected to a furnace equipped with hydrogen (H_2), methane (CH_4) and passivation gas (1% O_2& 99% N_2) flow. For samples of W, Ta, Nb, and V, the carbonization process is carried out at 1273 Kelvin (K) for one hour in a gas flowing environment of 100 mL min^{-1} H_2 and 20 mL min^{-1} CH_4. The temperature is ramped down to 1123 K and CH_4 flow is turned off. The temperature is held at 1123 K for fifteen to thirty minutes with a flow of 100 mL $mins^{-1}$ H_2 to remove excess surface carbon depending on the samples. [1] The temperature is then ramped down gradually to room temperature (RT) in a reduced H_2 flow of 70 mL min^{-1} followed by the passivation for one hour in a 30 mL min^{-1} 1% O_2/99% N_2 gas environment at RT.

Temperature at which CH_4 is turned off and the length for the surface carbon removal are essential for determining carbide phase formations and thickness of surface carbon. The exposure to sufficient amount of time in H_2 rich environment is necessary for surface carbon removal and thus enhance carbides' catalytic activity. However, it has been reported in the literature, WC can be decarburize to metallic W at high temperature in H_2 environment.[2] Therefore, the appropriate amount of H_2 exposure time and temperature have to be determined for each carbide. The last passivation process will form a thin layer of oxide to prevent carbides from undergoing fast exothermal ignation.[3]

2.1.1.2 Physical Vapor Deposition (PVD) for metal deposition

PVD is performed in a UHV chamber by evaporating a metal wire of interest wrapped on tungsten wire, as shown in Fig. 2.1. Tungsten wire can be heated by DC power and thus metal depositions on LSA TMC are controlled by the deposition time and supplied current. The metal overlayers can be quantified by use of XPS.

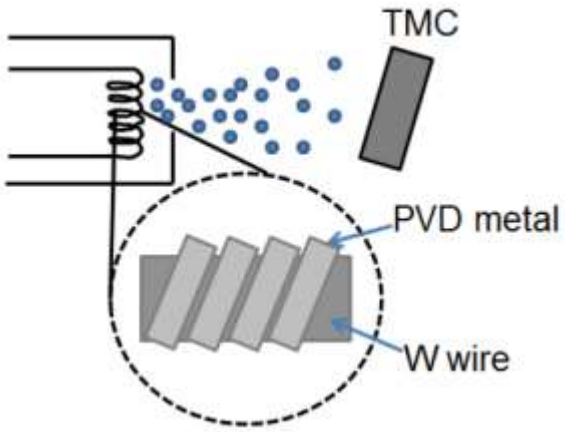

Figure 2.1 Physical vapor deposition of metal on the TMC thin film.

2.1.2 Powder catalysts synthesis

2.1.2.1 High surface area (HSA) TMC synthesis

HSA Mo_2C is made from its precursor ammonium molybdate tetrahydrate ($(NH_4)_6Mo_7O_{24}\cdot 4H_2O$) under a hydrogen flow of 122.5 mL min^{-1}. The temperature is raised gradually to 625 K and held for 12 h. Then methane gas is mixed into the flow (15% by volume) at 21.6 mL min^{-1} and the temperature is increased from 625 K to 940 K and held for 2 h. The sample was cooled to room temperature under the same gas environment. The flow was switched to argon at room temperature, without any passivation. It is worth pointing out that the surface area of passivated HSA Mo_2C has decreased by 80%. The detailed data and explanation can be found in chapter 3.

2.1.2.2 Wet impregnation of metals on HSA TMC

The wet impregnation is used to describe the process of mixing substrates into metal precursors solutions followed by vigorous stirring over multiple hours and thermal removal of precursor ligands. The synthesis method is used to synthesize metal-modified HSA Mo_2C, described in chapter 3 and to synthesize 1.5 weight percent (wt%) Pt on commercial TaC in chapter 5.

2.1.2.3 Incipient wetness impregnation (IWI) of metals on HSA TMC

In general, for IWI, the pore volume is determined by the minimum amount of deionized (DI) water used to saturate the calculated amount of catalysts. The amount of DI water is slowly dropped on the substrate until the point when the substrate is about to be fully saturated. The determined amount of water is then used to dissolve the metal precursor. Once the metal precursor is fully dissolved, the precursor solution is impregnated on the substrate in a drop-by-drop addition. Capillary forces drive the precursor solution into the support pores. Then the sample is heated in H_2 environment to remove ligands in the precursor. The IWI methods is used to synthesize Pd-modified tungsten carbides, described in Chapter 6.

2.1.2.4 One pot synthesis

One pot synthesis method is first to mix solutions of the metal precursor with the substrate precursor with rigorous stirring for over 10 hours. Then the solution is slowly evaporated followed by the thermal treatment. The substrate precursor is thermally carburized while the metal precursor ligands is simultaneously removed. The thermal treated process could result in strong chemical bonding between metals and carbides.[4] The synthesis method was used for preparing Pd-modified tungsten carbides, which was described in Chapter 6 .

2.2 Catalysts characterization techniques

Characterization techniques are frequently used at any stage of the research. X-ray diffraction (XRD)is used for species and crystal states identification. Unlike XRD as the bulk identification technique, X-ray photoelectron spectroscopy (XPS) is surface sensitive and reveals information about oxidation states of TMC. It is also used to quantify the deoposited metal overlayers. XPS and XRD provide provide insights of catalysts' stability and activity as well. Scanning Electron Microscope (SEM) and transmission electron microscope (TEM) reveals physical properties of the catalysts, such as morphology, topography and particles size distributions.

2.2.1 X-ray diffraction (XRD)

Symmetric XRD can reveal chemical properties of crystalline phase, crystalline orientation and crystal domain size. In my work, XRD is used to identify whether carbides was successfully formed after synthesis and whether carbide phase is single or mixed.

XRD spectra are formed due to the elastic scattering when a wavelength in monochromatic X-ray is consistent with crystals atomic distances within the sample. Bragg's law governs the constructive and destructive interference of the reflected X-rays based on symmetry and periodicity of atoms arragned in a crystal, illustrated by the equation below:

$$2d_{hkl}sin(\theta) = n\lambda$$

Where D_{hkl} is the distance between the diffraction planes, θ is the scattering angle with respect to the hkl plane, λ is the wavelength of the incident X-ray, and n is an integer. A visual illustration of Bragg's law is shown in Fig. 2.2.

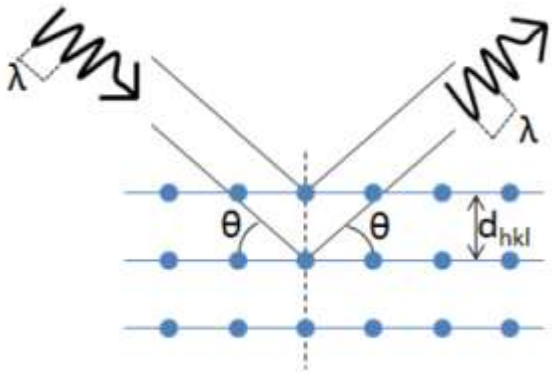

Figure 2.2 X-ray diffraction illustration.

2.2.2 X-ray photoelectron spectroscopy (XPS)

XPS is a surface sensitive technique and usually penetrate the surface within 10 nanometers. It has been extensively employed in my research to quantify the number of metal overlayers on carbides substrates and examine the oxidation states for pre and post electrochemical testing samples. The XPS results reveal important importation about the stability of deposited metals and carbides substrates.

2.2.2.1 Basics of XPS

In XPS, monochromatic x-ray sources, either Kα (1253.6 eV) or Al Kα (1486.7 eV) are used to bombard the sample. Core electron of the sample is ejected and detected. The XPS process is illustrated in Fig. 2.3. The kinetic energy that the ejected electron carries depends on the oxidation state of the element of interest. Although its kinetic energy was detected, the binding energy of the electron is useful for analysis. The calculation of its binding energy is shown as: $BE = h\nu - KE$

Where BE is photoelectron binding energy, hν is the X-ray source energy, which is either 1253.6 eV or 1486.7 eV, and kinetic energy is photoelectron kinetic energy.

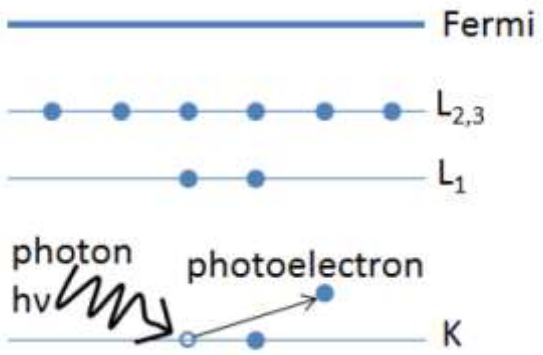

Figure 2.3 Schematic illustration of XPS process.

2.2.2.2 XPS applications for my research

In my work, specific binding energy of an element corresponds to its oxidation state, which can be used for surface phase identification and stability analysis. Moreover, the XPS peaks are used to quantify the metal atomic layers on TMC substrates. XPS peaks can be fitted using XPSPEAK version 4.1 software. Quantification process can be different depending on the elemental compositions within detected volume. If the detected volume only contains two elements. Atomic concentration can be calculated with respect to the other chemical species with the question shown as:

$$\frac{n_1}{n_2} = \frac{I_1/S_1}{I_2/S_2}$$

Where for the element x, n_x is the number of atoms for detected volume, I_x is the fitted peaks area and S_x is the atomic sensitivity[5].

In terms of metal-modified TMC samples, their surfaces usually contain more than two elements, so quantification method for calculating metal overlayers[6] is different, as shown below:

$$\frac{(I_O/S_O)}{(I_S/S_S)} = \frac{1-\exp[-\frac{d_O}{\lambda^O_{imfp}(E_O)\cos\theta}]}{\exp[-\frac{d_O}{\lambda^O_{imfp}(E_S)\cos\theta}]}$$

Where Inelastic mean free path(IMFP) indicates photoelectron penetration depth, which depends on the kinect energy of the photoelectron and type of solid medium. IMFP values for my calculations can be found in literature[6]. The subscript O represents overalyer and subscript S represents substrate. $\lambda^{o}_{imfp}(E_o)$ is the inelastic mean free path of electrons from element O, which is a function of the kinetic energy E_o of the photoelectrons from the overalyer. λ^{o}_{imfp} (E_s) is the inelastic mean free path of electrons from element O, which is a function of the kinetic energy E_s of the photoelectrons from the substrate. θ is used 54.7 degrees in our XPS set-up. d_o represents the thickness of the overalyer. In order to calculate the atomic layers of the deposited metals, one has to generate fitted peaks area of I_o and I_s and finding the values of the parameters describes above.

2.2.3 Electron microscopy

Electron microscopy that I used in my research are transmission electron microscopy (TEM) and scanning electron microscopy (SEM).

2.2.3.1 Transmission electron microscopy (TEM)

TEM uses high-energy electron beam (~ 300 keV) to transmit a sample to produce an image. Bright field imaging, as opposed to dark field imaging, was most common and used in my research for chemical composition and particle size distribution analysis of my samples. Bright field imaging is created by the passthrough of unadulterated beam through aperture at the focal plane while dark field imaging is produced by capturing diffracted beam. The bright image imaging was used in my research. In Bright field TEM imaging mode, lower atomic number elements shows in a lighter color compared to heavier atoms, which allow to differentiate metals from substrates.

2.2.3.2 Scanning electron microscopy (SEM)

Unlike TEM, eletron in SEM are not able to transmit through the sample. SEM rasters eletron beams with 1-40 keV across the sample. SEM images are created based on inelastic and elastic scattering of electrons off the surface. Secondary electron imaging uses inelastic scattering of low-energy electrons, which makes it very sensitive to differences in surface heights. Backscattered electron imaging uses elastic scattering of high-energy electrons which make it very sensitive to difference in atomic number. In my work, the SEM characterizes the morphology and topography of the samples, both powder and thin films. SEM imaging could also provide insights of the morphology changes after exposing the catalysts samples in electrochemical reaction conditions.

2.3 Electrochemical methods

Electrochemical testing is performed once catalyst samples are synthesized and characterized. Catalysts in thin films and powder forms are tested for their activity and stability for hydrogen evolution reaction (HER) and ethanol oxidation reaction in both acid and alkaline electrolytes.

2.3.1 Three-electrode electrochemical cell

The three-electrode electrochemical cell, as shown in fig. 2.4. is a glass-made cell that accommodates working, counter and reference electrodes, and aqueous acid electrolyte. The three electrodes are directly connected to the potentiostat for electroanalytical experiments. The cell is convenient to conduct electrocatalytic kinetics study for half electrochemical reaction, where three electrodes are placed in one cell without separation from a membrane. The working electrode is either catalyst thin films, carbon papers or rotating disk electrode (RDE) both with

powder catalyst ink. Counter electrode completes the circuit, which allow the electrons to freely flow through from the working electrode to the counter electrode. All published results are reported with respect to reversible hydrogen electrode (RHE) because RHE is independent of the solutions pH and thus allow easier comparison in activity for various catalysts.

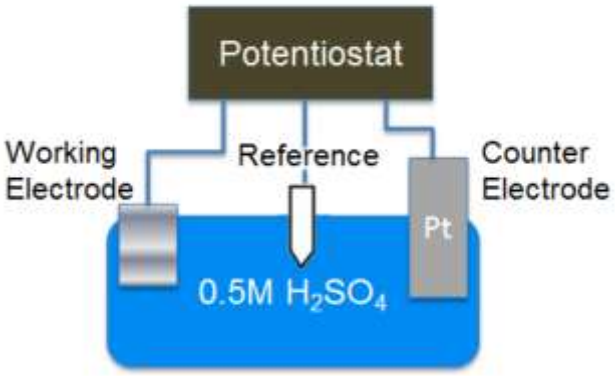

Figure 2.4 schematic illustration of three-electrode electrochemical cell in acid environment.

In order to minimize the transport effect, RDE, that powder catalyst ink can be deposited on, is used to to create laminar flow of the electrolyte over the electrodes to remove products and supply reactants to the RDE surface. For thin film working electrodes, magnetic stirrers are used to minimize the diffusion effect.

2.3.2 Electroanalytical technique

2.3.2.1 Linear scanning voltammetry (LSV)

LSV provides transient current (*i*) as a function of applied potential at a constant scan rate. The applied potential usually starts from the potential where activity is thermodynamically unfavorable to reversible potential, governed by Gibbs free energy, to an overpotential where high activity is expected. For HER reaction, LSVs are also used for Tafel analysis to reveal

exchange current density (i_o), which is reversible potential at thermodynamic equilibrium condition.

The Tafel analysis is to fit LSV data to the Tafel equation shown below:

$$\eta = m \log_{10}(|i|) + b$$

$$m = \frac{-2.303RT}{\alpha F}$$

$$b = -m \log_{10}(i_0)$$

Where i is current density, T is temperature, F is faraday constant, α is the symmetry factor, and η is overpotential. This equation is a simplification of the kinetics equation (Butler-Volmer equation) at the relative high-overpotential range, shown below:

$$i = i_0 \left(\exp\left[(1-\alpha) \frac{F}{RT} \eta \right] - \exp\left[-\alpha \frac{F}{RT} \eta \right] \right)$$

2.3.2.2 Cyclic Voltammetry (CV)

CV can be considered as a continuous LSV reversal scanning process between a set potential E_1 and the other set potential E_2 at a specific scan rate. CV scans can oxidize reactants during anodic scan and then products can be reduced during cathodic scan. In my work, CV is mainly used to electrochemical clean a catalyst' surface and remove impurities and oxides.

2.3.2.3 Chronoamperometry (CA)

CA is used to achieve steady-state current as a function time at an applied potential. CA is a more accurate measurement because it removes the current from capacitive effect. It is also used for testing a catalyst' stability.

2.3.2.4 Electrochemical surface area (ECSA) measurement

The electrochemical surface area (ECSA) of Pd-modified tungsten carbides is determined using cyclic voltammetry (CV) in an Ar-saturated 0.5M H_2SO_4 electrolyte. Instead of the Pd-H region, the Pd-O region had been reported to be more accurate to determine Pd ECSAs in carbon-supported Pd and Pd-based catalysts due to absorption of hydrogen atoms into Pd sublayers.[7] The monolayer charge of adsorbed oxygen, two times larger than the charge of the hydrogen monolayer (Q_H= 210 μC cm^{-2})[89], is 420 μC cm^{-2} is used for determining Pd ECSA.

Instead of CO chemisorption and hydrogen underpotential deposition (UPD) measurements, copper UPD is used to calculate ECSA of Pt-modified TaC surface. Because TMC substrates might absorb hydrogen as well. The atomic layer of copper is deposited on Pt atoms and then they are stripped off the surface. The ECSA was calculated by dividing Q with 420 μC/cm^{-2}.

2.4 *In-situ* infrared reflection absorption spectroscopy (IRRAS)

In-situ IRRAS is one type of IR spectroscopy that is used to detect the bonding configurations of reaction intermediates on catalyst surfaces and measure the concentrations of reactants and products in the gas and aqueous phases. In my work, the IRRAS is coupled with the potentiostate to allow LSV testing and IRRAS detections happen simultaneously. It is used to detect reactions intermediates and changes in concentration of reactions and final products for the ethanol electrooxidation reaction on Pt-modified TaC and Pd-modified tungsten carbides catalysts.

2.5 Density functional theory (DFT)

2.5.1 Fundamentals of DFT

DFT is a computationally low-cost method to obtain an approximately solution to the Schrödinger equation of a many-body system. The Schrödinger wave function is the fundamental of quantum mechanics[10]: $E\Psi = \hat{H}\Psi$

Where E is the energy, Ψ is the wave function and Ĥ is the Hamiltonian operator. Unfortunately, it is impossible to solve this equation for a N-body system.

Born-Oppenheimer approximation simplifies the Hamiltonian operator assuming no magnetic moments[11], as shown below:

$$\hat{H} = -\frac{1}{2}\sum_{i=1}^{n}\nabla_i^2 - \sum_{\mu=1}^{N}\sum_{i=1}^{n}\frac{Z_\mu}{r_{\mu i}} + \sum_{i=1}^{n-1}\sum_{j=i+1}^{n}\frac{1}{r_{ij}}$$

where the first term expresses the kinetic energy of the electrons, the second term express electron-nucleus interaction and the third term describes the electron-electron interactions. The calculation for individual electron-electron interactions is computationally expensive.

Since DFT emphasizes the electron density rather than individual electron-electron interactions, Kohn-Sham (KS) equations[12] were developed:

$$\left(-\frac{1}{2}\nabla^2 + v_{\text{eff}}(\mathbf{r}) - \varepsilon_j\right)\varphi(\mathbf{r}) = 0$$

Where the first term inside the bracket expresses the standard kinetic term and the third terms describes the energy of the orbital j. The second term expresses an effective external potential, which is further expressed in the equation[12] shown below:

$$v_{\text{eff}}(\mathbf{r}) = v(\mathbf{r}) + \int \frac{\rho(\mathbf{r}')}{|\mathbf{r} - \mathbf{r}'|}\mathrm{d}\mathbf{r}' + v_{xc}$$

where the first term on the right accounts for the electron-nucleus interaction and the second term accounts for the electron-electron Coulomb interaction and the third term is the exchange correlation potential. Among all terms, the exchange correlation potential has to be further approximately. Two major functionals are the local density approximation (LDA) and the generalized gradient approximation (GGA).[13] Once the exchange correlation potential is selected, the electron density ρ (r) expression is shown below:

$$\rho(\mathbf{r}) = \sum_{i=1}^{n} |\varphi_i(\mathbf{r})|^2$$

Then the ground state energy can be obtained by the following equation:

$$E[\rho] = -\frac{1}{2}\sum_{i=1}^{n}\langle\varphi_i|\nabla^2|\varphi_i\rangle + \frac{1}{2}\iint\frac{\rho(\mathbf{r})\rho(\mathbf{r}')}{|\mathbf{r}-\mathbf{r}'|}d\mathbf{r}d\mathbf{r}' - \int v(\mathbf{r})\rho(\mathbf{r})d\mathbf{r} + E_{xc}[\rho].$$

Where the first term accounts for the kinetic energy of the non-interacting system, the second term accounts the Coulomb electron-electron interaction, the third term accounts for the electron-nucleus interaction. the last term accounts for the other interactions and corrections including the difference between the kinetic energy of the non-interacting system and the exact kinetic energy, the electron exchange repulsions and correlation effects for both the exchange and Coulomb interactions.

2.5.2 the application of DFT in research projects

The open software Vienna ab-initio software package (VASP) is used for the DFT calculation. In the context of my research, DFT is used to calculate the adsorption strength of adsorbates on modelled surfaces. Intermediates binding energy on metals, TMC and metal-modified TMC were calculated based on the equation shown below:

$$BE = E_{adsorbate/surface} - E_{adsorbate} - E_{surface}$$

The results can be used to predict catalytic activity towards the reaction of interest by correlating with electrochemical testing results and shed lights on reaction mechanisms. In Chapter 4, to investigate effective descriptors for HER in acid and alkaline electrolytes, both hydrogen binding energy and hydroxyl binding energy on the catalytic surfaces were calculated and then correlated to experimental results of HER activity for these catalysts. For ethanol oxidation work (Chapter 5 and chapter 6), the calculated activation energy barrier for different reaction pathway provides in-depth understandings of enhanced catalytic activity. Also, the calculated binding energy of the possible reaction intermediates on catalytic surfaces of interest also provides predictions on the examined catalysts activity towards the ethanol oxidation reaction.

2.6 Surface science technique

Ultrahigh vacuum (UHV) equipment has been developed for catalysis research since 1960[s]. This field was recognized in the 2007 Nobel Prize in Chemistry, which was given to Gerhard Ertl for UHV studies of ammonia synthesis on iron surfaces. The surface chemistry can be well studied in UHV (~ $1*10^{-10}$) by excluding the pressure and reaction condition factors. The samples are used in surface science studies are model surfaces, such as Pt (111) and Pt (100) facets. Therefore, the effects of terrace and crystal defects are eliminated. Moreover, the UHV environment enables use of various spectroscopic techniques, which are essential to understand surface structure and reactivity.

UHV techniques in this work includes Auger electron spectroscopy (AES), mass spectrometry (MS) and high-resolution electron energy loss spectroscopy (HREELS). AES was used to characterize surface composition, similar to XPS function described above. For

Temperature programmed desorption (TPD) UHV chamber, MS and AES were used to analyze the gas-phase productions of chemical reactions as well as the reaction pathways of molecules. For HREELS UHV chamber, AES and HREELS are equipped to detect reactions intermediates and analyze the bond breaking sequence of molecules on surfaces.

2.6.1 Auger electron spectroscopy (AES)

AES was primarily used to determine surface cleanliness and composition. Figure 2.5 illustrate three electron process for AES. Incoming electrons with a kinetic energy, ranging from 2 to 9 keV, bombard the sample. An electron in a core level is ejected, creating a vacancy. This vacancy is filled by an electron from one of the outer levels. The energy liberated is transferred to another electron in the outer level, causing the electron on the outer level to escape beyond the vacuum level. The analyzer detects the escaped electron with the specific kinetic energy, which is particular to a certain element. The kinetic energy that the escaped electron is carried satisfies the following equation:

$$KE = E_K - E_{L_1} - E_{L_2}$$

In terms of the quantification of metal overlayers on TMC from the Auger signals, the analysis process is similar to that of XPS, described in the section 2.2.2.2.

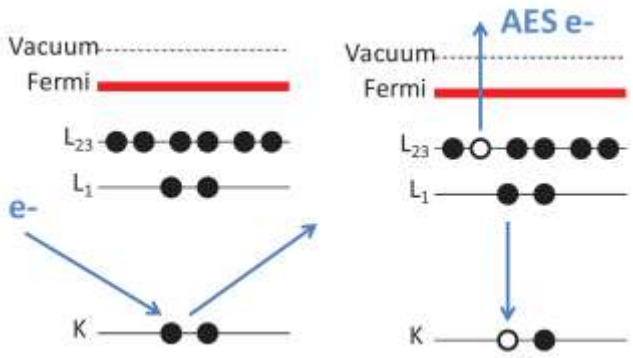

Figure 2.5 Schematic illustration of three electron Auger process.

2.6.2 High-resolution electron energy loss spectroscopy (HREELS)

HREELS is a vibrational spectroscopy used to detect adsorption configurations and reaction intermediates. HREELS is similar to reflectance infrared spectroscopy, but the UHV chamber allows HREELS to detect bond vibrations in the fingerprint region, which is below 600 cm^{-1}. In HREELS, electrons with a uniform energy of 6 eV bombard the adsorbates and catalytic surface with an 60^{o} angle and then scattered back and detected. Three types of scattering events can occur, which are dipole scattering, impact scattering and inelastic scattering via an negative ion resonance. Among all three scattering events, the dominant scattering event is dipole scattering. The dipole scattering is caused by the interactions between the field of the incident electron and the dynamic dipole of the adsorbate. In other words, a vibrational normal mode of an adsorbed molecule is excited and the oscillation of the electric dipole results in electric fields. These electric fields scatter the incident electron beam and results in an energy loss. The energy loss of scattered electrons can be expressed by the equation shown below:

$$E_{loss} = E_{elastic} - E_{dipole} = h\nu$$

Where E_{loss} is the energy lose by the scattered electron, $E_{elastic}$ is the energy for the elastic peak and E_{dipole} is the dipole scattered electron.

Impact scattering is caused by the interactions between the incident electrons and the localized atomic potential of the adsorbates. The impact scattering is a much shorter range occurring for the electrons close to the surface around 1Å while the dipole scattering occurs for the electrons 10~100 Å above the surface. The inelastic scattering is difficult to detect due to the short lifetime of electronic states.

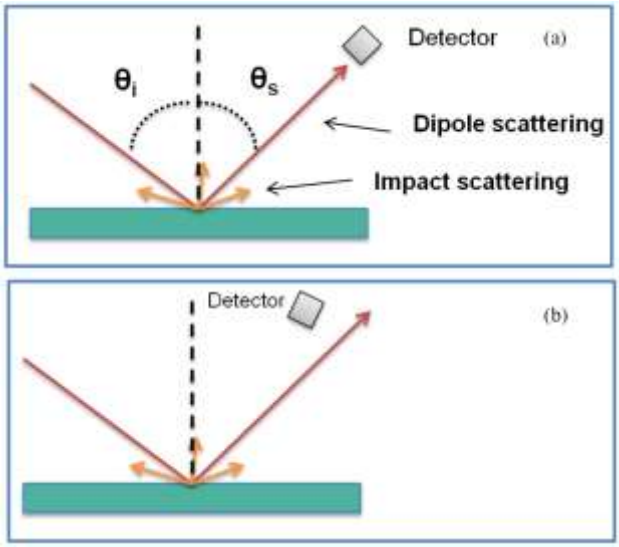

Figure 2.6 Schematic illustration of the HREELS process under the on-specular mode (a) and off-specular mode (b).

Between impact scattering and dipole scattering, impact scattering has an isotropic angular distribution while the dipole scattering has a narrow angular distribution. Therefore, When the HREEL spectroscopy operates in the on-specular mode, as shown in Fig. 2.5a, detectors mainly receive dipole scattering. When the spectroscopy operates in the off-specular mode, the impact scattering were mainly detected, as shown in Fig. 2.5b.

References

(1) Kimmel, Y. C.; Esposito, D. V.; Birkmire, R. W.; Chen, J. G. *Int. J. Hydrogen Energy* **2012**, *37* (4), 3019–3024.

(2) Durst, J.; Siebel, A.; Simon, C.; Hasché, F.; Herranz, J.; Gasteiger, H. A. *Energy Environ. Sci.* **2014**, *7* (7), 2255.

(3) Oyama, S. T. In *The Chemistry of Transition Metal Carbides and Nitrides*; Springer Netherlands: Dordrecht, 1996.

(4) Lin, L.; Sheng, W.; Yao, S.; Ma, D.; Chen, J. G. *J. Power Sources* **2017**, *345*, 182–189.

(5) Moulder William F Stickle Peter E, J. F.; Kennetlf Bomben, S. D. **1995**.

(6) Cumpson, P. J.; Seah, M. P. *Surf. Interface Anal.* **1997**, *25* (6), 430–446.

(7) Álvarez, G. F.; Mamlouk, M.; Scott, K. *Int. J. Electrochem.* **2011**, *2011*, 1–12.

(8) Breiter, M. W. *J. Electroanal. Chem. Interfacial Electrochem.* **1977**, *81* (2), 275–284.

(9) Rand, D. A. J.; Woods, R. *J. Electroanal. Chem.* **1971**, *31* (1), 29–38.

(10) Schrödinger, E. *Ann. Phys.* **1926**, *385* (13), 437–490.

(11) Born, M.; Oppenheimer, R. *Ann. Phys.* **1927**, *389* (20), 457–484.

(12) Kohn, W.; Sham, L. J. *Phys. Rev.* **1965**, *140* (4A), A1133–A1138.

(13) Ceperley, D. M.; Alder, B. J. *Phys. Rev. Lett.* **1980**, *45* (7), 566–569.

3. TRENDS IN HYDROGEN EVOLUTION ACTIVITY OF METAL-MODIFIED MOLYBDENUM CARBIDES IN ALKALINE AND ACID ELETROLYTES

3.1 Introduction

Water electrolysis coupled with renewable energy sources is an attractive way to produce CO_2-free hydrogen gas. Polymer electrolyte membrane electrolysis cells (PEMECs) produce high pressure, ultra-high purity hydrogen and can quickly shift across their entire operating capacity more easily than traditional liquid alkaline electrolysis.[1] Thus, PEMECs are well suited for decentralized renewable energy storage at the local level. On a larger scale, membrane electrolysis powered by centralized renewable energy could be used to provide hydrogen for Fischer-Tropsch synthesis of fuels and commodity chemicals. In order for electrolysis to be viable for either of these applications, however, the use of rare and expensive platinum group metals at the electrolyzer cathode and anode needs to be reduced or, ideally, eliminated.[2]

For proton exchange membrane electrolysis, the hydrogen evolution reaction (HER) at the cathode proceeds efficiently with as little as 0.05 mg_{Pt}/cm^2.[3] It is the anodic oxygen evolution reaction (OER) in acidic cells that requires the use of much greater amounts of expensive iridium or ruthenium metal.[4] Conversely, in an alkaline environment (i.e. a hydroxide exchange membrane cell) non-noble metals are stable under OER conditions and achieve similar activity as the precious metals.[4] But the HER on Pt catalyst in alkaline conditions is slower than in acid, and requires greater than 20 times the Pt loading compared to an acid environment to achieve the

same efficiency.[5] Developing novel inexpensive HER catalysts for alkaline membrane cells is therefore a promising path toward reducing the cost of water electrolysis.

Many efforts have been made to reduce the amount of platinum group metals needed for HER. Among them, our group has focused on utilizing transition metal carbides (TMCs) modified with atom-thick monolayers (ML) of Pt or other metals. The TMCs have bulk electronic structures similar to Pt,[6] and metal modification can tune the hydrogen binding energy, as calculated by density functional theory (DFT).[7] This hydrogen binding energy has been shown to correlate with acidic HER activity for monometallic[8] and metal modified TMC[9] surfaces via a volcano relation. It has also been shown that HBE on monometallic surfaces reveal a volcano trend with alkaline HER activity,[10] however the curve peak may be shifted.[11] Although we have demonstrated the HER activity on several metal modified carbide systems on thin film electrocatalysts in acid, it is important to extend these findings to industrially relevant high surface area powder catalysts in alkaline electrolyte.[7,9,12–14] It is also important to compare the trends in alkaline and acidic electrolytes to assess the applicability of the DFT screening method in both environments.

In the current manuscript, we explore the effects of adding metal nanoparticles to high surface area, nanocrystalline molybdenum carbide(Mo_2C) in order to develop trends in alkaline HER activity. We also compare these trends to those in alkaline electrolytes. Mo_2C was selected as the carbide substrate because it is easily synthesized as a high surface area powder at relatively low temperatures (<600°). Recent work also shows that Mo_2C is an effective HER catalyst on its own.[13,15,16] The metal was deposited on an un-passivated Mo_2C surface, a technique that improved activity for certain heterogeneous catalytic reactions.[17–19] We selected silver(Ag), copper(Cu), and nickel(Ni) transition metals to deposit on Mo_2C because they are inexpensive and often have good catalytic qualities. Pt and Pd were also chosen because they are good HER catalysts.

As mentioned above, DFT calculated hydrogen binding energy(HBE) is often a useful predictor of HER activity. Surfaces with binding energies near that of Pt at the peak of the volcano curve are most active. Higher HBE is unfavorable for product desorption, and lower HBE results in low surface coverage at low overpotentials. Both of these factors increase overpotential and decrease electrolyzer's efficiency. Table 3.1 displays the DFT calculated HBE for one monolayer of each metal on $Mo_2C(001)$. Values were calculated for overlayers on a Mo-terminated carbide. Compared with the previously calculated Pt(111) HBE of -0.46eV, Cu- and Ni-Mo_2C are most similar.[7] We therefore expected these materials to have the highest HER activity. Similarly, the high binding energies of unmodified Mo_2C and the low binding energies Ag-, Pd-, and Pt-Mo_2C were expected to be less active for the HER.

3.2 Experimental Section

3.2.1 DFT Calculations

The DFT calculations were similar to those in a previous study.[20] Briefly, spin polarized density functional theory (DFT) [21,22] calculations were performed using Vienna Ab-Initio Simulation Package (VASP) code.[23,24] A plane wave cut-off energy of 400 eV and $3 \times 3 \times 1$ Monkhorst-Pack grid were used for total energy calculations.[25] The interactions between electrons and nuclei were treated with all electron like projector augmented wave (PAW) potentials with the generalized gradient approximation (GGA) [26,27] using PW91 functionals.[28] Ionic positions were optimized until Hellman-Feynman force on each ion was smaller than 0.01 eV $Å^{-1}$.

The surfaces of $Mo_2C(001)$, both with and without monolayer (ML) Ag, Cu, Ni, Pd, or Pt were modeled using a four layer 3×3 surface slab. The Ag, Cu, Ni, Pd, and Pt /$Mo_2C(001)$ surfaces were modeled by adding a monolayer of Ag, Cu, Ni, Pd, and Pt on top of $Mo_2C(001)$ surfaces, respectively. A vacuum layer of ~12 Å thick was added in the slab cell along the direction perpendicular to the surface in order to minimize the artificial interactions between the surface and

its periodic images. During geometry optimization, atoms in the top two layers were allowed to relax while the atoms in the bottom two layers were fixed. The binding energy of hydrogen (HBE) is calculated as

$$\mathbf{HBE} = \mathbf{E_{slab+H}} - \mathbf{E_{slab}} - \frac{\mathbf{1}}{\mathbf{2}}\mathbf{E_{H_2}}$$

where E_{slab+H}, E_{slab}, and E_{H2} are the total energies of slab with adsorbed H, clean slab, and H2 molecule in gas phase, respectively.

3.2.2 Catalyst Preparation

The synthesis of 5 wt % metal (Pt, Pd, Ni, Ag, Cu) on non-passivated nanopcrystalline Mo_2C followed a procedure previously reported in the literature.[17] Briefly, 650 mg of ammonium molybdate tetrahydrate ($(NH_4)_6Mo_7O_{24}{\cdot}4H_2O$, Sigma Aldrich), sieved to 106-250 µm, was loaded into a ceramic boat in a horizontal quartz tube furnace under a hydrogen flow of 122.5 mL min^{-1}. The temperature was raised gradually to 350 °C and held for 12 h. Then methane gas was mixed into the flow (15% by volume) at 21.6 mL min^{-1} and the temperature was increased from 350 °C to 590 °C and held for 2 h. The sample was cooled to room temperature under the same gas environment. The flow was switched to argon at room temperature, without any passivation. Under an Ar blanket, the sample was transferred to a Ar de-aerated aqueous solution containing target amounts of Pt, Pd, Ag, Ni, or Cu metals precursors. The metal precursors used were H_2PtCl_6 (8 wt%inH_2O); $Pd(NO_3)_2{\cdot}2H_2O$; $Ni(NO_3)_2{\cdot}2H_2O$; $Ag(NO_3){\cdot}2H_2O$; $Cu(NO_3)_2{\cdot}3H_2O$ (Sigma Aldrich). The solution was continuously bubbled with Ar and agitated with a magnetic stirrer for 15 h in order to achieve sufficient interaction between metal precursor and the non-passivated Mo_2C powder. Then the solution dried at 80 °C for about 3 h. When most of the liquid evaporated, samples were transferred back into the furnace where they were further dried at 110 °C for 2 h under H_2. Once the samples were dried, they were calcined under flowing H_2 at 310°C for 4 h.

Samples were cooled down to room temperature and then passivated in 1% O_2 in N_2. Pt on passivated Mo_2C was made in a similar manner, but Mo_2C was passivated after initial carburization. Pt on commercial Mo_2C was synthesized using the same wet impregnation technique and the same calcination heating profile.

3.2.3 Electrode Preparation

Electrocatalyst ink was made with 50 mg of catalyst samples dispersed in 2.4 mL deionized (DI) water purified to a resistivity above 17 MΩ cm by a Barnstead-NAN-Opure filtration system, 2.4 mL isopropanol, and 0.05 mL Nafion 117 solution (Sigma Aldrich). The ink was then sonicated in an ice bath for 1 h. 2 mg electrocatalyst was dropped onto a 1 cm^2 carbon paper electrode (Toray TGH-H-060 30 wt % wet-proofing) directly after sonication. The electrode was air-dried overnight before electrochemical measurement.

3.2.4 Electrochemical Measurements

Electrochemical experiments were carried out at room temperature in 0.1 M potassium hydroxide (KOH) or 0.5 M sulfuric acid (H_2SO_4). Electrolytes made by dissolving desired amount of potassium hydroxide (Sigma Aldrich) with DI water or diluting concentrated sulfuric acid (Sigma Aldrich) with deionized water. The electrochemical measurements were conducted in a three-electrode set-up with a graphite (Sigma Adrich, 99.995% trace metal basis) counter electrode and either a reversible hydrogen electrode (Hydroflex) or double junction saturated Ag/AgCl electrode as a reference electrode. Princeton Applied Research Versa STAT 4 was used as potentiostat. In terms of conditioning the working electrode surfaces, twenty cyclic voltammetry (CV) scans between 0.05 and 0.5 V vs. RHE were conducted in Ar-saturated electrolyte at a scan rate of 100 mV s^{-1}. After CV, the electrolyte was purged with H_2 gas for 15 minutes. Then, LSV was used to measure the HER activity of prepared electrodes. LSV

was performed at a sweep rate of 10 mV s^{-1} starting at 0.1 V and going in the negative direction. The cell resistance was measured at the beginning of each LSV in hydrogen saturated electrolyte via electrochemical impedance spectroscopy (EIS). Electrochemical stability was tested by cycling samples between -0.5V and 0.5V 50 times at a scan rate of 10 mV s^{-1}.

3.2.5 Catalyst Characterization

Surface area and pore volume of the prepared catalysts were determined by the NOVA e-Series Surface Area Analyzer based on nitrogen physisorption. Approximately 0.1 g of catalyst was measured and degassed at 300 °C for 12 h, to obtain more accurate surface area and pore volume by removing trapped H_2O molecules in pores. N_2 adsorption was then performed with 30% N_2 and 70% He. the surface area was calculated based on the BET multiple point method and the pore volume was estimated based on the BJH desorption equation.[29]

The XRD patterns of fresh catalysts were obtained using a PANalystical X'Pert[3] Powder XRD apparatus with a Ni filtered Cu Kα X-ray source. The samples were scanned between 30° to 90° 2θ with a scan speed of 0.2188 degree s^{-1}. An operating potential of 40 kV and operating current of 40 mA cm^{-2} were used. The mean crystallite sizes (*ds*) for tested samples were calculated based on Scherrer's Equation[30] from the line broadening of the most intense reflections:

$$\boldsymbol{ds = \frac{K\lambda}{\lambda \cdot \beta \cos\theta}}$$

where β is the full width at half maximum of the selected peak, θ is the Bragg angle, λ the wavelength of the incident X-ray beam, and K=0.93 is the numerical constant.

Scanning Electron Microscopy (SEM) measurements were conducted with HATACHI S-4700 I Cold Field Emission Scanning Electron Microscope, with accelerating voltage of 20 kV,

emission current of 10 μA and working distance of 10 mm. Transmission electron microscopy (TEM) imaging was performed on a JEOL 2100F TEM operated at 200 kV.

XPS measurements were performed with a Phi 1600 XPS system with an Al X-ray source and hemispherical analyzer. Dry electrode samples were loaded into the chamber for analysis before and after electrochemical performance and durability testing.

3.3 Results and Discussion

3.3.1 DFT Calculations

As mentioned above, DFT calculated HBE is often a useful predictor of HER activity. Surfaces with binding energies near that of Pt at the peak of the volcano curve are most active. Higher HBE is unfavorable for product desorption, and lower HBE results in low surface hydrogen coverage. Both of these factors increase overpotential and decrease electrolyzer efficiency. Table 3.1 displays the DFT calculated HBE for one monolayer of each metal on Mo_2C(001). Values were calculated for overlayers on Mo-terminated and C-terminated carbides. The C-terminated surface was previously reported as the most stable and most probable surface, but Mo-terminated surfaces were also likely to be present as a result of the nanocrystalline structure of the synthesized catalysts.[31,32] Compared with the previously calculated Pt(111) HBE of -0.46 eV, Pt- and Pd- on C-terminated Mo_2C and Cu- and Ni- on Mo-terminated Mo_2C were most similar.[7] It was therefore expected that those materials would have the highest HER activity. Similarly, Ag-Mo_2C and unmodified Mo_2C were expected to have the lowest activity, because their HBE values for both Mo- and C-terminated carbide differ significantly from that of Pt(111).

Table 3.1 Hydrogen binding energy (eV) over metal modified Mo_2C (Mo- and C-terminated (001) surfaces). Difference (eV) from Pt(111) HBE in parentheses.

	C-terminated carbide	Mo-terminated carbide
Mo_2C	-1.52 (-1.06)	-1.08 (-.062)
Ag-Mo_2C	-0.04 (+0.42)	0.17 (+0.63)
Cu-Mo_2C	-0.15 (+0.31)	-0.40 (+0.06)
Ni-Mo_2C	-0.78 (-0.32)	-0.48 (-0.02)
Pt-Mo_2C	-0.45 (+0.01)	-0.11 (+0.35)
Pd-Mo_2C	-0.61 (-0.15)	-0.22 (+0.24)
Pt(111)	-0.46	

3.3.2 Catalyst Particle Characterization

XRD analysis revealed the phase of catalyst particles and the estimated crystallite size. Generally, two carbide phases were present in the samples. They were identified as β-Mo_2C (hcp crystal structure) and α-MoC_{1-x} (fcc crystal structure). This was consistent with previous results that used a similar synthesis method.[17] Figure 3.1 shows that unmodified Mo_2C was dominated by β-Mo_2C, but an increased amount of α-MoC_{1-x} was observed among all metal modified Mo_2C samples. The largest amount of the α-phase was found in Cu- and Ag-Mo_2C. There was no evidence of diffraction peaks related to molybdenum oxides on any sample. There was some amount of Mo-oxide phase present, however, as detected by X-ray photoelectron spectroscopy (Fig. 3.6). This oxide phase is caused by passivation of powders after metal impregnation and calcination. The passivation oxidized surface defect sites to prevent rapid exothermic bulk oxidation upon exposure to air. These surface oxides were not detected in the XRD bulk analysis. The crystallite size of Mo_2C was estimated to be less than 5 nm based on the Scherrer

equation. There were no sharp metallic peaks in the patterns, suggesting that the metals were well dispersed and nanocrystalline. For comparison, the patterns of commercial Mo_2C and 5% Pt-modified commercial Mo_2C are also shown in Figure 3.1. Only β-phase Mo_2C was present in these two samples, and the crystallite sizes were estimated to be approximately 90 nm – much larger than Mo_2C samples prepared in the current study.

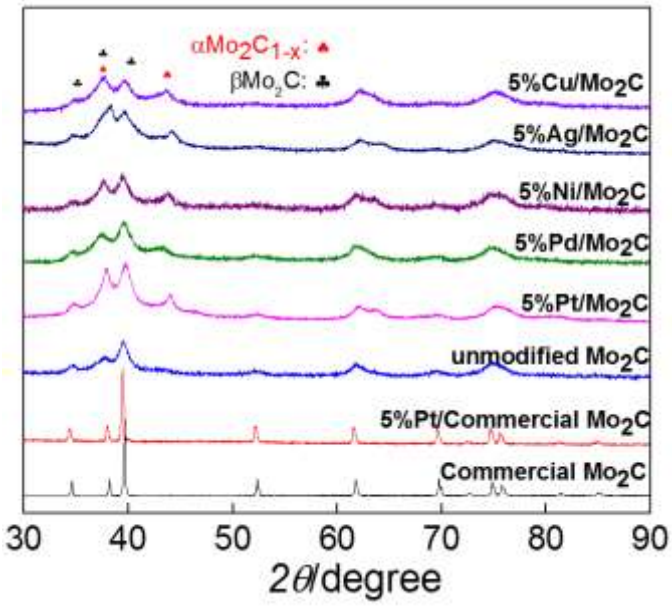

Figure 3.1 XRD patterns of metal modified and unmodified Mo_2C. The peaks at 34.8°, 38.4°, 39.8°, 52.5°, 61.9°, 69.6°, and 74.9° 2θ are attributed to the hexagonal β-Mo_2C. The peaks at 37.1°, 42.8°, 62.4°, 74.5° and 78.4° are attributed to α-MoC_{1-x}.[33]

Figure 3.2 shows the morphollogical changes of the catalysts throughout synthesis via scanning electron microscopy (SEM). After calcination of the Mo precursor, MoO_2 was obtained in the form of large extended platelets. After carburization, the β-dominated unmodified Mo_2C morphology mostly maintained the same rectangular platelet shape as the MoO_2, although broken platelet particles were also observed. This was possibly due to small amounts of α-MoC_{1-x} being formed. The metal modified Mo_2C, which had higher amounts of α-MoC_{1-x}, contained not only broken rectangular platelet shape particles, but more agglomerated isotropic particles.

Figures 3.2E and 2F show representative TEM images of 5% Pt- and Cu-Mo_2C, respectively. The nanocrystalline nature of the Mo_2C substrate made it difficult to obtain accurate metal nanoparticle size distributions. However, no large metal agglomerates were observed, and the distinguishable metal particles that were visible ranged between 5 and 7nm. Other metals on Mo_2C looked similar to the Cu- and Pt-Mo_2C images presented here. The TEM results confirm the presence of well dispersed nanoparticles on Mo_2C.

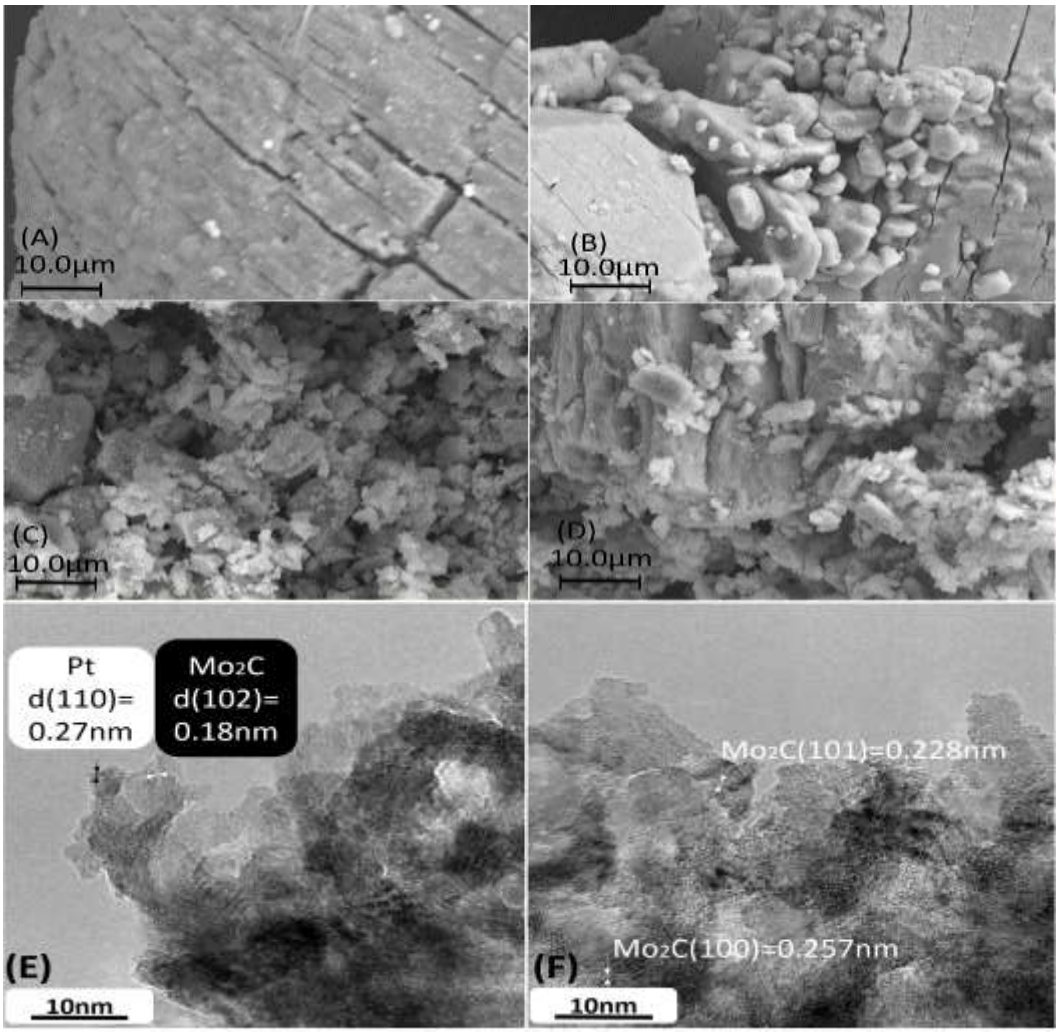

Figure 3.2 Scanning electron microscopy (SEM) images showing (A)MoO_2 (B) β dominated Mo_2C (C) Cu modified α&β-Mo_2C and (D) Pd modified α&β-Mo_2C. Transmission electron microscopy (TEM) images showing (E) 5% Pt-Mo_2C and (F) 5% Cu-Mo_2C.

3.3.3 Electrocatalytic Activity

Electrochemical performance of each metal-modified Mo_2C sample was investigated by linear scanning voltammetry (LSV) at a scan rate of 10 mV s^{-1}. All potentials are reported vs. the reversible hydrogen electrode (RHE) and corrected for uncompensated solution resistance using electrochemical impedance spectroscopy (EIS). The typical resistances for alkaline and acid electrolytes were around 20 Ω and 14 Ω, respectively.

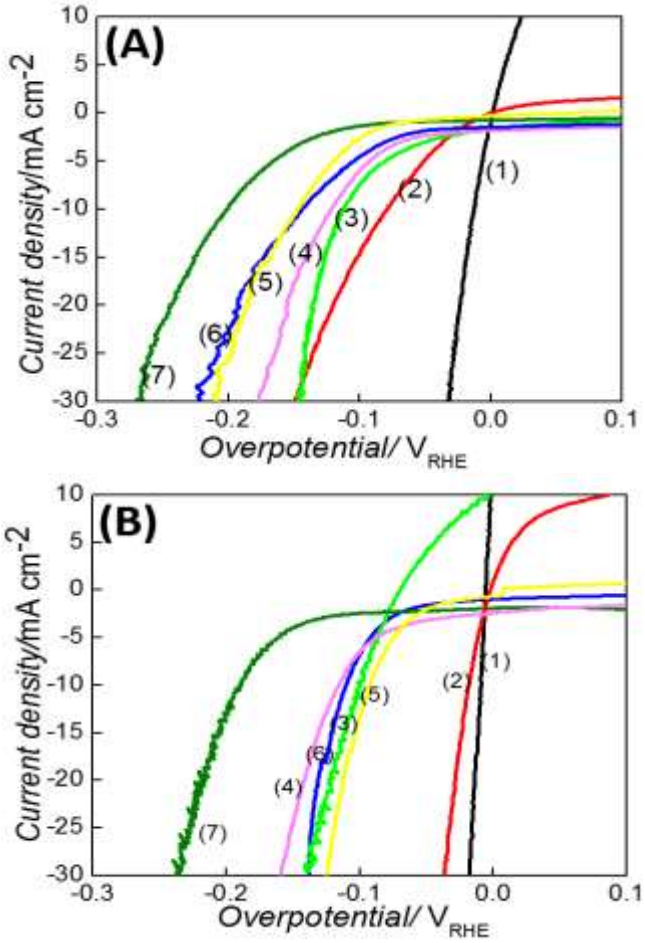

Figure 3.3 HER electrocatalytic performance comparison. (A) LSV comparison of prepared samples in 0.1M KOH electrolytes (B) LSV comparison of prepared samples in $0.5MH_2SO_4$. Both graphs include commercial 40% Pt on Vulcan carbon. The numbers within the parenthesis represent the following: (1) 40% Pt/C (black), (2) 5% Pt-Mo_2C (red), (3) 5% Pd-Mo_2C (neon green), (4) 5% Ni-Mo_2C (magenta), (5) unmodified Mo_2C (yellow), (6) 5%Ag-Mo_2C (blue), (7) 5% Cu-/Mo_2C (Green).

Figure 3.3 compares the HER activity of all samples in acid and alkaline electrolyte. The current densities reported were based on the geometric area of the electrode (1 cm^2). Anodic

currents at positive potentials are caused by hydrogen oxidation reaction in the H_2 saturated electrolyte. Although electrochemical surface area was not measured for the electrodes, the BET surface area for each sample was roughly the same (around 25 $m^2 g^{-1}$). Also, identical catalyst mass loading (2 mg cm^{-2}) was used for each electrode. This should allow for reasonably accurate comparison of electrochemical activity between different samples.

The 5% Pt, Pd, Ni, Ag, and Cu modified Mo_2C samples were studied for HER in 0.1M KOH (Fig. 3.3A) and in 0.5M H_2SO_4 (Fig. 3.3B) electrolytes. Alkaline HER activities were categorized into 3 groups based on the overpotentials (η) required for each sample to reach a given current density. Pertinent values from electrochemical testing are presented in Table 3.2 Pt- and Pd-Mo_2C were the most active. Pt-Mo_2C showed activity for hydrogen oxidation at positive potentials and had the lowest HER onset overpotential of 0 mV. Pd-Mo_2C had a higher onset overpotential but reached -30 mA cm^{-2} at about the same overpotential as Pt-Mo_2C. Unmodified Mo_2C, Ni- and Ag-Mo_2C were the next most active group. They had similar onset overpotentials in the range of 110 mV to 140 mV and required around 160 – 200 mV to achieve -20 mA cm^{-2}. The 5% Cu-Mo_2C was the least active among the samples in this study. It showed an onset overpotential near 190 mV and required around 240 mV to achieve -20 mA cm^{-2}. Thus, the HER activity trend observed in 0.1M KOH was: Cu-Mo_2C < Ag-Mo_2C, unmodified Mo_2C, Ni-Mo_2C < Pd-Mo_2C, Pt-Mo_2C. Further, similar mass loadings (2 mg cm^{-2}) of commercial 40% Ag, 20% Cu, and 20% Ni on Vulcan carbon were tested in alkaline electrolyte (not shown). Each of the pure metals required at least 200 mV larger overpotential to reach 20 mA cm^{-2} current densities compared to their nanoparticle modified Mo_2C counterparts. This shows that the metal-substrate interaction increases HER activity for alkaline electrolytes.

The same activity trend observed in alkaline electrolyte was observed in acidic conditions, with the exception of Pd-Mo_2C. Pd-Mo_2C produced positive current at negative applied overpotential. This was probably due to a well-known issue with hydrogen absorption into the palladium lattice that obscures the HER current in acid at low HER potentials.[34,35] This effect is not known to occur in the other metals analyzed here under the HER reaction conditions used (based on Pourbaix diagrams).[36] Otherwise, the activities in acid were again grouped into three categories. Cu-Mo_2C was least active, Ag-, Ni-, and unmodified Mo_2C were moderately active, and Pt-Mo_2C was the most active, resembling 40% Pt-C.

Table 3.2 Electrochemical performance comparison of all prepared samples including commercial 40%Pt/C in 0.5M H_2SO_4 electrolytes and 0.1M KOH electrolytes.

	0.1M KOH			0.5M H_2SO_4		
	Onset (V)	η (V)@ -10 mA cm^{-2}	η (V)@ -20 mA cm^{-2}	Onset (V)	η (V)@ -10mA	η (V) @ -20 mA cm^{-2}
40% Pt-C_(1)	0.00	-0.01	-0.02	0.00	-0.01	-0.01
5% Pt-Mo_2C_(2A)	0.00	-0.08	-0.12	0.00	-0.02	-0.03
5% Pt-Mo_2C_(2B)	-0.2	-0.5	–	0.05	-0.13	-0.18
5% Pd-Mo_2C_(3)	-0.08	-0.11	-0.14	--	--	--
5% Ni-Mo_2C_(4)	-0.10	-0.12	-0.16	-0.1	-0.13	-0.15
Mo_2C_(5A)	-0.12	-0.14	-0.18	-0.07	-0.09	-0.11
Mo_2C_(5B)	-0.42	-0.59	–	-0.2	-0.31	-0.39
5% Ag-Mo_2C_(6)	-0.14	-0.14	-0.19	-0.12	-0.11	-0.13
5% Cu-Mo_2C_(7)	-0.19	-0.2	-0.24	-0.18	-0.19	-0.22

The HER activity trend observed in both acid and base is somewhat consistent with the calculated HBEs for C-terminated Mo_2C. Pt- and Pd-Mo_2C had similar HBEs to Pt(111), which supported their high HER activity. The other samples had HBEs that deviated further from the HBE of Pt(111), consistent with the lower HER activities. However, within the lower activity groups, there appeared to be a lack of correlation with HBE. Unmodified C-terminated Mo_2C had

the highest binding energy by 0.4 eV, yet it was moderately active compared to the other tested samples. Cu-Mo_2C had favorable HBEs, but consistently showed the lowest HER activity among tested samples. Some of this might be explained by the co-existence of Mo- and C-terminated surfaces, but no clear trend beyond the high activity of Pt- and Pd-Mo_2C was apparent. The lack of strong correlation between HBE and HER activity could be caused by several factors. First, the HBE was calculated on the (001) surface of β-Mo_2C. This facet is likely to be representative of highly crystalline, pure phase β-Mo_2C powders, but significant amounts of α-phase carbide were present in the samples synthesized in the current study. This means that a significant portion of the HER active sites in the current experiments were not representative of the specific surfaces studied in the DFT calculations. More importantly, the DFT calculated HBE values for monolayer metal on the carbide substrate, but the synthesized powder catalysts were composed of metal nanoparticles dispersed on Mo_2C. Thus, there were bulk metal sites that were not accounted for by the monolayer DFT study. This illustrates the importance of using well-defined surfaces when establishing trends and the importance of developing well-controlled synthesis techniques in order to utilize DFT-predicted trends.

3.3.4 Synthesized vs. Commercial Mo_2C Comparison

The comparison of HER electrocatalytic activities between commercial and in-house synthesized Pt-Mo_2C and unmodified Mo_2C in acid and base is illustrated in Figure 3.4. The 5% Pt-modified commercial Mo_2C required around 400 mV more overpotential to reach -10 mA cm^{-2} than its in-house synthesized counterpart in the alkaline environment. The same comparison in acidic electrolyte showed only a 100 mV increase for 5% Pt-modified commercial Mo_2C, but the advantage of supporting Pt on nanocrystalline Mo_2C was evident. The activity increase in acid and base for the same Pt mass loading was likely due to an increase in electrochemical active surface

area. The in-house synthesized Mo_2C had BET surface area of around 25 $m^2 g^{-1}$ compared with the commercial Mo_2C, which was around 2 $m^2 g^{-1}$, and the crystallite size was much smaller for the synthesized Mo_2C (Figure 3.1). Thus, there were far more Mo_2C active sites upon which HER could occur. The higher surface area also likely promoted better Pt dispersion, which would also increase the number of Pt active sites. This higher activity per mass of Pt in base shows that Pt-modified nanocrystalline Mo_2C has potential to reduce the amount of Pt needed for alkaline electrolyzers.

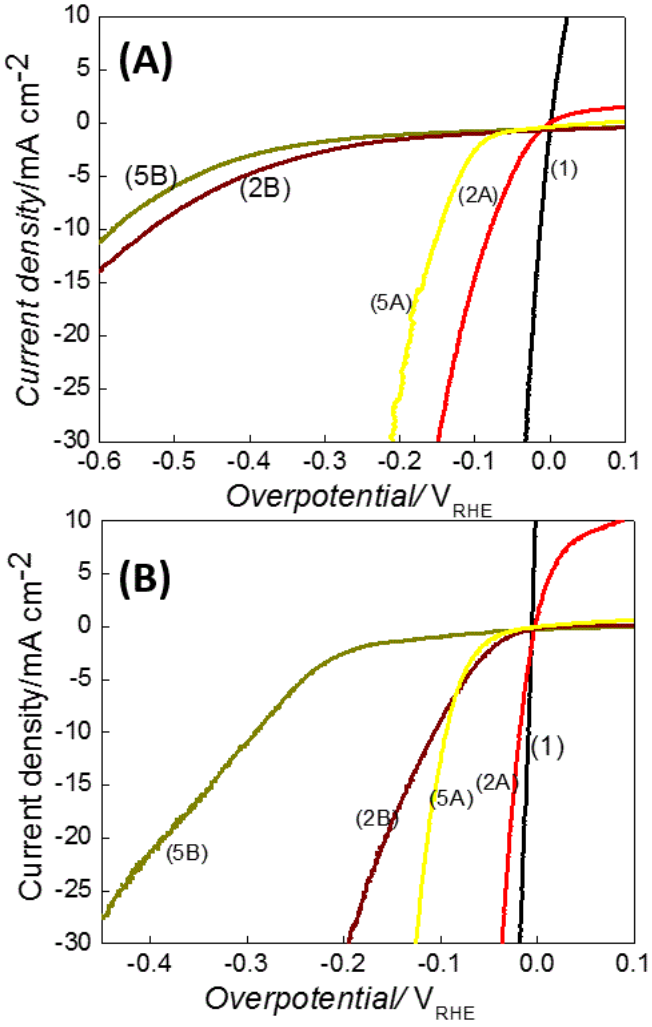

Figure 3.4 HER electrocatalytic performance comparison. (A) LSV of prepared unmodified Mo_2C and 5% Pt modified Mo_2C samples compared with commercial Mo_2C and 5% Pt modified commercial Mo_2C in 0.1M KOH electrolytes. Commercial 40% Pt on Vulcan carbon also included. (B) LSV comparison of the same catalysts in (A), but in

0.5MH_2SO4. The numbers within the parenthesis represents the following: (1) commercial 40% Pt/C (black), (2A) 5% Pt/Mo_2C (red), (2B) 5% Pt/commercial Mo_2C (dark red), (5A) unmodified Mo_2C(yellow) (5B) commercial Mo_2C (dark yellow).

The unmodified nanocrystalline Mo_2C showed similar activity improvements over commercial Mo_2C in both acid and base. Considering that both unmodified Mo_2C samples were mostly β-phase, the increase in activity for in-house synthesized Mo_2C was likely a result of higher surface area. Furthermore, the activity of the synthesized unmodified Mo_2C, which achieved -30 mA cm^{-2} current in about 120 mV in acid, appeared to compare favorably to the most recent Mo_2C nanorods and nanoparticles, which achieved current densities of -60 mA cm^{-2} at 200 mV.[15] A direct comparison was difficult, however, because the studies mentioned used only 0.2 mg cm^{-2} mass loading compared to 2 mg cm^{-2} in this study.

3.3.5 Passivated vs. Non-passivated Mo_2C Comparison

The deposited metals in this study were in direct contact with native (i.e. non-passivated) Mo_2C. This metal/substrate interaction was shown to increase activity for heterogeneous catalysis in comparison with metals deposited on passivated Mo_2C.[17–19] Here, comparison of Pt on passivated and non-passivated Mo_2C is presented to determine if this synthesis technique also improved the HER activity. Figure 3.5 displays characterization and electrochemical analysis of 5% Pt on passivated and non-passivated Mo_2C. In Figure 3.5A, the LSV plot clearly shows sluggish HER activity for Pt on passivated Mo_2C. In order to achieve -10 mA cm^{-2} current, more than 300 mV had to be applied, compared with 80 mV for Pt on non-passivated Mo_2C. The XRD provided insight into the decreased activity. Figure 3.5B shows increased crystallite size manifested by sharper peaks at the Pt(111) and Pt(200) facets. Although the principle Pt(111) peak (~40° 2θ) was convoluted with the β-Mo_2C peak at the same position, the increase in peak sharpness was obvious when inspecting the Pt(200) peak at 46.5° 2θ. For Pt on passivated Mo_2C, the crystallite size based on the full width at half maximum (FWHM) of the Pt(200) peak was

estimated to be about 15 nm, while crystallite size for the Pt on non-passivated Mo_2C was only 5 nm. The increased crystallite size in the passivated sample suggested the presence of large Pt agglomerates as opposed to dispersed nanoparticles. This result was consistent with the SEM analysis of Wyvratt et al. that revealed large Pt agglomerate formation on passivated Mo_2C.[19]

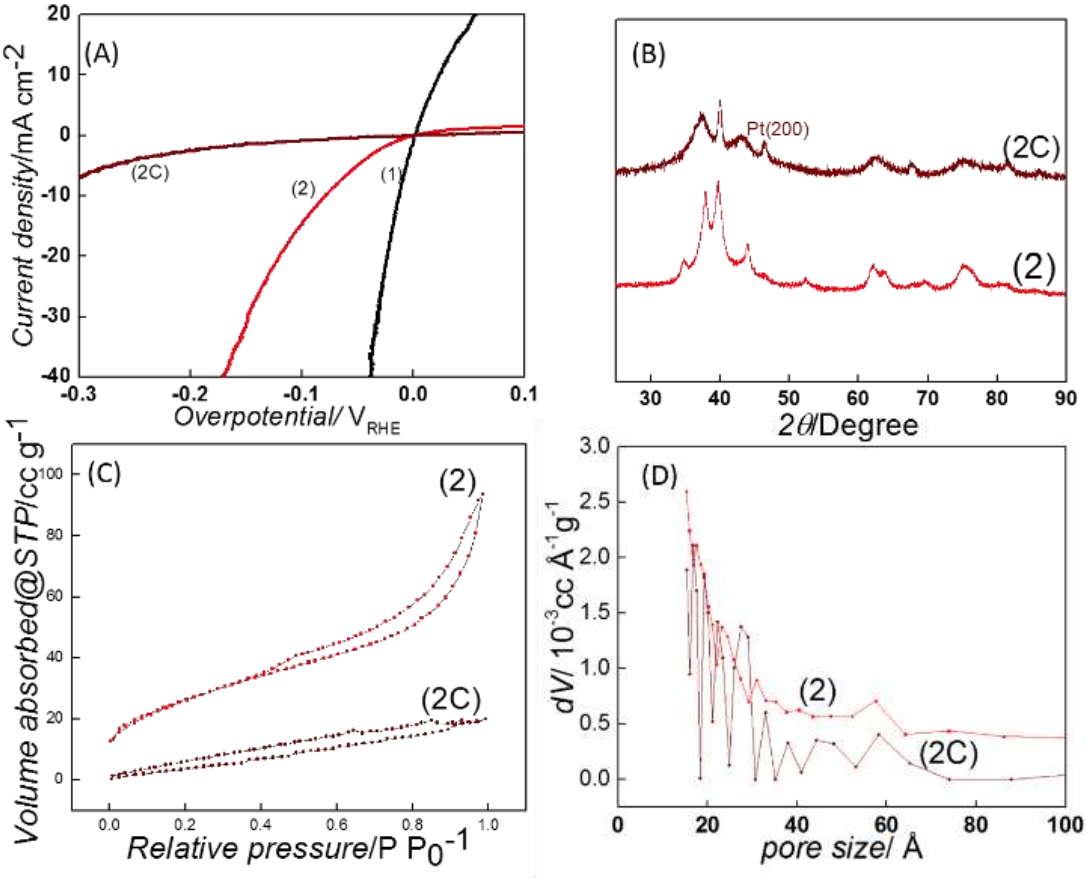

Figure 3.5 Comparison of the wet impregnation of platinum on non-passivated Mo_2C with that on passivated Mo_2C. (A) Linear Sweep Voltammetry (LSV) comparison of the prepared samples in 0.1M KOH electrolytes including commercial 40% Pt on Vulcan carbon. (B) XRD pattern of 5% Pt on non-passivated Mo_2C and on passivated Mo_2C. (C) Nitrogen absorption/desorption isotherm, (D) pore size distribution. The numbers within the parenthesis represent the following: (1) 40% Pt/C (black), (2) 5% Pt/Mo_2C (red), (2C) 5% Pt/Mo_2C after passivation (dark red).

Additionally, BET analysis in Figure 3.5C shows a dramatic decrease in the BET surface area for the 5% Pt on passivated Mo_2C sample (5.4 m^2 g^{-1}) as opposed to that on non-passivated Mo_2C (26.5 m^2 g^{-1}).[37] The pore size distribution based on the BGH equation illustrated that the

decreased surface area was mainly due to a significant shrinkage in pore volume at each pore size.[29] This can be related to the growth of thin oxide layer caused by passivation. Based on these results, it appears that the decreased pore volume and the oxide layer for the passivated sample inhibited Pt dispersion during calcination, causing Pt to agglomerate, which resulted in the decreased HER activity observed in Figure 3.5A.

3.3.6 Metal-modified Mo_2C Electrochemical Stability

Structural stability of the metal modified carbides are important to understanding their HER activity. Insights into metal stability and phase during HER can be obtained from thermodynamic Pourbaix diagrams, which show metal stability in different potential and pH regions. Ag, Pt, Ni, and Pd should all be in metallic phase in alkaline conditions at the HER potentials used, according to the diagrams.[36] Cu forms a stable passivated CuO_2 phase under HER potentials at high pH, which could contribute to the low Cu-Mo_2C HER activity. At low pH, Ag, Cu, and Pt should all be stable. Ni becomes oxidized and Pd forms the previously discussed hydride phase in acidic HER conditions.[36] These provide some insights into the behavior of pure metals, but the metal modified carbides studied here may have different structural stability under HER conditions.

To understand electrochemical stabilit, cyclic voltammetry (CV) was performed on the samples after LSV curves were recorded. For each sample, 50 CV cycles were performed between 0.5 and -0.5 V. There did not appear to be any change in HER activity during these cycles, which indicated good electrochemical stability.

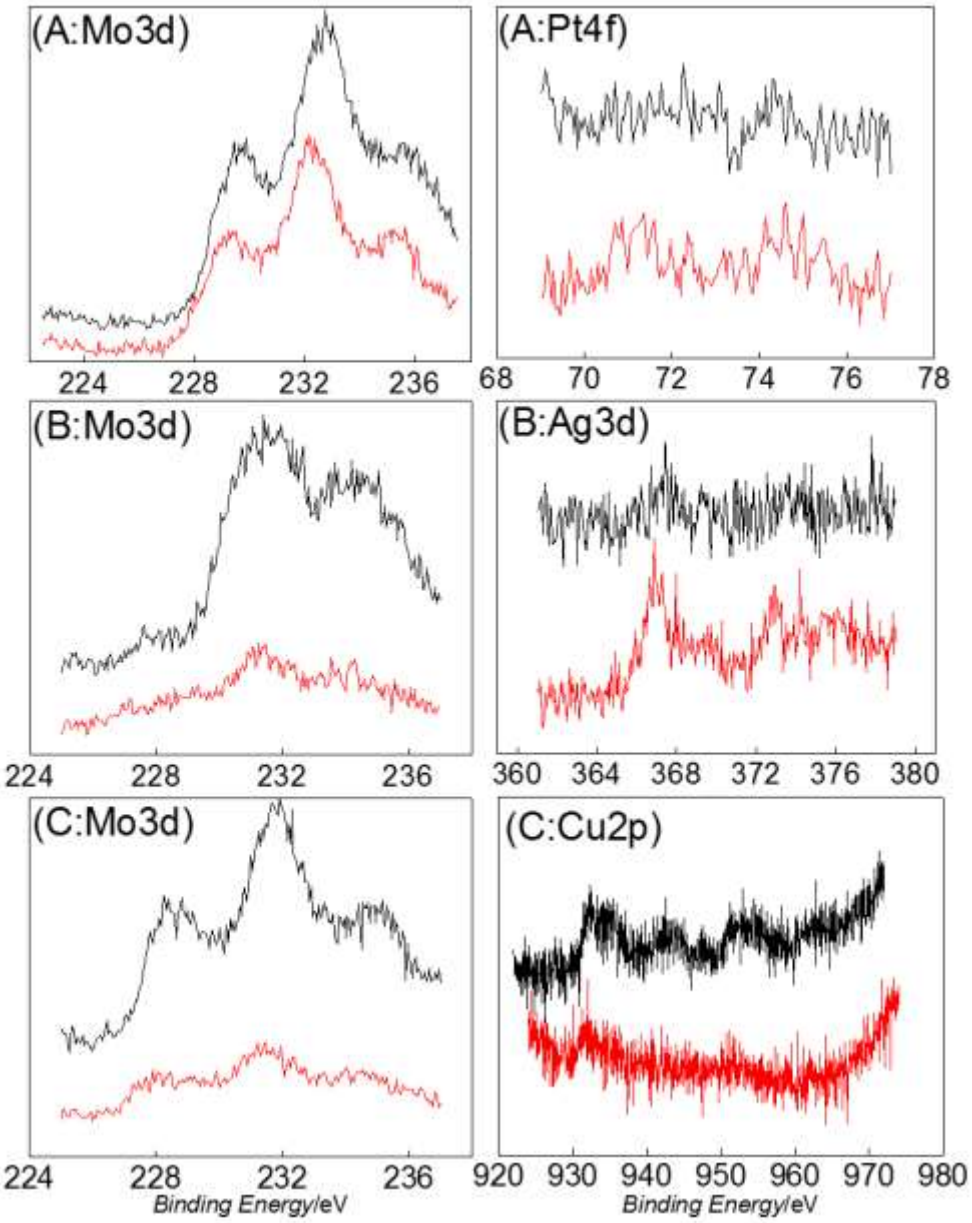

Figure 3.6 XPS results for samples on 30% wet-proof carbon paper before and after electrochemical testing in 0.1M KOH. 5% Pt-Mo_2C (A), 5% Ag-Mo_2C (B), 5% Cu-Mo_2C (C). Fresh (before HER) and spent (after HER) electrodes are indicated in black and red color, respectively.

To determine if metal particles were stable on Mo_2C throughout electrochemical testing, XPS measurements were taken on the electrodes. Figure 3.6 shows XPS results for Pt-, Ag- and Cu-Mo_2C samples before and after HER testing in 0.1M KOH. The Mo 3d peaks are shown for each sample, and the Pt 4f, Ag 3d, and Cu 2p peaks are shown for their respective samples. Compositional quantification was difficult due to the low metal mass loading (0.1 mg) and additive

species present (i.e. Nafion binder and polytetrafluoroethylene wet-proofing on the carbon paper) on each electrode. However, a qualitative analysis of the peaks revealed that Pt, Ag and Cu, were all present before and after HER testing. This is evidenced by the Pt $4f_{5/2}$ peaks at 75 eV, the Ag $3d_{5/2}$ peaks at 367 eV, and the Cu $2p_{3/2}$ peaks at 932 eV. In each case, the Mo 3d peak intensities decreased after HER testing. This could either be due to catalyst chemical instability and dissolution, or it could be due to screening of XPS metal intensities by adsorbed electrolytes. It is interesting to note that Metal/Mo peak ratios appeared to increase for Ag-Mo_2C after HER testing. This has been observed previously for metal modified carbides.[38] The Ag-Mo_2C sample had the most Mo-oxide phase present, indicated by large peaks at higher binding energies before HER. The Mo 3d oxide peaks for this sample decreased after HER. Thus it is possible that an overlayer of Mo-oxide was dissolved during HER testing, exposing higher relative amounts of Ag underneath. Overall, the presence of Cu, Pt, and Ag on the electrode before and after HER testing is consistent with results of the electrochemical stability CV testing. More quantitative studies will be needed to further understand the stability of metals on Mo_2C

3.4 Conclusions

In this study, we demonstrated successful synthesis of well-dispersed metal nanoparticles on high surface area nanocrystalline Mo_2C. The observed activity trend for metal modified Mo_2C catalysts (Cu-Mo_2C < Ag-Mo_2C, unmodified Mo_2C, Ni-Mo_2C < Pd-Mo_2C, Pt-Mo_2C) was consistent in both acid and alkaline environments. The acidic and alkaline HER mass activity of unmodified Mo_2C synthesized in this study greatly outperformed commercially available Mo_2C, due to the increased surface area of the in-house synthesized Mo_2C. Pt, Ag, and Cu metals were present on Mo_2C before and after alkaline HER testing, making their corresponding metal modified carbides potential candidates for hydroxide exchange membrane electrolysis cells.

Future work should focus on developing accurate trends for metal modified carbides in alkaline environments by using well-defined metal thin films over carbide substrates. Well-controlled synthesis methods, such as atomic layer deposition of metal on carbide nanoparticles, should also be explored in order to utilize established trends and DFT screening more effectively for the discovery of novel, high surface area HER catalysts.

References

(1) Ursua, A.; Gandia, L. M.; Sanchis, P. *Proc. IEEE* **2012**, *100* (2), 410–426.

(2) Lehner, M.; Tichler, R.; Steinmüller, H.; Koppe, M. *Power-to-Gas: Technology and Business Models*; SpringerBriefs in Energy; Springer International Publishing: Cham, 2014.

(3) Durst, J.; Simon, C.; Hasche, F.; Gasteiger, H. a. *J. Electrochem. Soc.* **2014**, *162* (1), F190–F203.

(4) McCrory, C. C. L.; Jung, S.; Peters, J. C.; Jaramillo, T. F. *J. Am. Chem. Soc.* **2013**, *135* (45), 16977–16987.

(5) Sheng, W.; Gasteiger, H. a.; Shao-Horn, Y. *J. Electrochem. Soc.* **2010**, *157* (11), B1529.

(6) Levy, R. B.; Boudart, M. *Science* **1973**, *181* (4099), 547–549.

(7) Esposito, D. V; Hunt, S. T.; Stottlemyer, A. L.; Dobson, K. D.; McCandless, B. E.; Birkmire, R. W.; Chen, J. G. *Angew. Chem. Int. Ed. Engl.* **2010**, *49* (51), 9859–9862.

(8) Nørskov, J. K.; Bligaard, T.; Logadottir, A.; Kitchin, J. R.; Chen, J. G.; Pandelov, S.; Stimming, U. *J. Electrochem. Soc.* **2005**, *152* (3), J23.

(9) Kimmel, Y. C.; Yang, L.; Kelly, T. G.; Rykov, S. A.; Chen, J. G. *J. Catal.* **2014**, *312*, 216–220.

(10) Sheng, W.; Myint, M.; Chen, J. G.; Yan, Y. *Energy Environ. Sci.* **2013**, *6* (5), 1509.

(11) Sheng, W.; Zhuang, Z.; Gao, M.; Zheng, J.; Chen, J. G.; Yan, Y. *Nat. Commun.* **2015**, *6*, 5848.

(12) Esposito, D. V.; Chen, J. G. *Energy Environ. Sci.* **2011**, *4* (10), 3900.

(13) Kelly, T. G.; Hunt, S. T.; Esposito, D. V.; Chen, J. G. *Int. J. Hydrogen Energy* **2013**, *38* (14), 5638–5644.

(14) Tackett, B. M.; Kimmel, Y. C.; Chen, J. G. Manuscript submitted for publication.

(15) Tang, C.; Sun, A.; Xu, Y.; Wu, Z.; Wang, D. *J. Power Sources* **2015**, *296*, 18–22.

(16) Scanlon, M. D.; Bian, X.; Vrubel, H.; Amstutz, V.; Schenk, K.; Hu, X.; Liu, B.; Girault, H. H. *Phys. Chem. Chem. Phys.* **2013**, *15* (8), 2847–2857.

(17) Schaidle, J. A.; Schweitzer, N. M.; Ajenifujah, O. T.; Thompson, L. T. *J. Catal.* **2012**, *289*, 210–217.

(18) Schweitzer, N. M.; Schaidle, J. A.; Ezekoye, O. K.; Pan, X.; Linic, S.; Thompson, L. T. *J.*

Am. Chem. Soc. **2011**, *133* (8), 2378–2381.

(19) Wyvratt, B. M.; Gaudet, J. R.; Thompson, L. T. *J. Catal.* **2015**, *330*, 280–287.

(20) Tackett, B. M.; Kimmel, Y. C.; Chen, J. G. *Int. J. Hydrogen Energy* **2016**, *41* (14), 5948–5954.

(21) Hohenberg, P. *Phys. Rev.* **1964**, *136* (3B), B864–B871.

(22) Kohn, W.; Sham, L. J. *Phys. Rev.* **1965**, *140* (4A), A1133–A1138.

(23) Kresse, G.; Furthmüller, J. *Comput. Mater. Sci.* **1996**, *6* (1), 15–50.

(24) Kresse, G.; Hafner, J. *Phys. Rev. B* **1993**, *48* (17), 13115–13118.

(25) Monkhorst, H. J.; Pack, J. D. *Phys. Rev. B* **1976**, *13* (12), 5188–5192.

(26) Kresse, G. *Phys. Rev. B* **1999**, *59* (3), 1758–1775.

(27) Blöchl, P. E. *Phys. Rev. B* **1994**, *50* (24), 17953–17979.

(28) Perdew, J. P.; Wang, Y. *Phys. Rev. B* **1992**, *45* (23), 13244–13249.

(29) Barrett, E. P.; Joyner, L. G.; Halenda, P. P. *J. Am. Chem. Soc.* **1951**, *73* (1), 373–380.

(30) Patterson, A. *Phys. Rev.* **1939**, *56* (10), 978–982.

(31) Shi, X.-R.; Wang, S.-G.; Wang, H.; Deng, C.-M.; Qin, Z.; Wang, J. *Surf. Sci.* **2009**, *603* (6), 852–859.

(32) Politi, J. R. dos S.; Viñes, F.; Rodriguez, J. A.; Illas, F. *Phys. Chem. Chem. Phys.* **2013**, *15* (30), 12617–12625.

(33) Ma, Y.; Guan, G.; Shi, C.; Zhu, A.; Hao, X.; Wang, Z.; Kusakabe, K.; Abudula, A. *Int. J. Hydrogen Energy* **2014**, *39* (1), 258–266.

(34) Łukaszewski, M.; Czerwiński, A. *J. Solid State Electrochem.* **2011**, *15* (11–12), 2489–2522.

(35) Durst, J.; Simon, C.; Hasche, F.; Gasteiger, H. A. *J. Electrochem. Soc.* **2014**, *162* (1), F190–F203.

(36) Pourbaix, M. *Atlas of electrochemical equilibria in aqueous solutions*, 2d English.; Houston, TX, 1974.

(37) Brunauer, S.; Emmett, P. H.; Teller, E. *J. Am. Chem. Soc.* **1938**, *60* (2), 309–319.

(38) Kimmel, Y. C.; Yang, L.; Kelly, T. G.; Rykov, S. A.; Chen, J. G. *J. Catal.* **2014**, *312*, 216–220.

4.THE CORRELATION BETWEEN ALKALINE HYDROGEN EVOLUTION REACTION WITH THE GIBBS FREE ENERGY CHANGE OF ADSROBED HYDROGEN FOR METAL-MODIFIED TRANSITION METAL CARBIDES

4.1 Introduction

Water electrolysis can provide CO_2-free hydrogen for energy storage and chemical synthesis that is crucial for enabling increased solar energy capacity[1] and CO_2 utilization technologies[2,3]. As such, the hydrogen evolution reaction (HER) has been extensively studied over the past decade, with emphasis on conditions relating to the compact and versatile polymer electrolyte membrane (PEM) cells. While acidic (proton transport membrane) HER is catalyzed by acceptably small loadings of Pt, water electrolysis at low pH is critically hindered by the requirement for expensive IrO_x catalysts for the oxygen evolution reaction (OER). To circumvent this problem, alkaline (hydroxide transport membrane) OER is readily catalyzed by many non-precious metal oxides, notably Fe and Ni compounds.[4,5] However, alkaline HER kinetics are slower than in acid, increasing the Pt loading requirement. Thus, recent research has been devoted to both discovering an inexpensive replacement for the Pt HER catalyst and understanding the cause of slower HER kinetics at high pH.

Understanding atomic descriptors can provide insight on reaction mechanisms and help screen for new active catalysts. For example, Norskov et al.[6] used the well-established experimental correlation between a metal's M-H bond energy and its HER activity[7] to develop a database of density functional theory (DFT)-calculated hydrogen binding energies (HBEs) for monometallics. This resulted in a volcano curve when plotted with experimental exchange current. Their work provided new thermodynamic data about the adsorbed hydrogen intermediate involved in the acidic Volmer-Heyrovsky-Tafel HER mechanism (Eq. 1- 3), which consists of the Volmer step followed by either the Heyrovsky or the Tafel step. This approach also allowed the DFT-calculated HBE to be used as a screening tool for other acid HER catalysts. This was especially useful for developing low-cost electrocatalysts with single atom-thick layers (monolayers) of Pt supported on transition metal carbides (TMCs).[8,9] Later, Sheng et

al. showed that a similar volcano correlation exists between DFT-calculated HBEs and experimental alkaline HER activity on monometallic catalysts.[10] The correlation showed that HBE was important for alkaline HER, but it did not explain why alkaline HER is slower than in acid. It is also unclear whether such DFT calculations will be useful for Pt-modified TMCs, which are important for reducing Pt loading in alkaline HER.

In this work, we first aim to extend the DFT-calculated HBE correlation to metal-modified TMCs to determine the utility of HBE for this class of materials in alkaline HER. We then explore the relationship between DFT-calculated hydroxyl binding energy (OHBE) and alkaline HER activity on metal-modified TMCs. The hydroxyl group appears in the alkaline Volmer step (Eq. 4) and Heyrovsky step (Eq. 5), so it likely impacts HER kinetics more than in the acidic case. As stated above, alkaline HER is not completely described by HBE alone, and recent studies have aimed to describe the exact role of the hydroxyl for alkaline HER (mostly on Pt surfaces). Some conclude that adsorbed OH directly participates in the Volmer step,[11] while others state that hydroxyl only indirectly impacts HER kinetics through competitive adsorption[12] or hydrogen stabilization.[13,14] Whatever the case, clearly hydroxyl binding energy should be understood to describe alkaline HER. This is especially true for TMC surfaces, which are typically more oxophilic than Pt.

Volmer Step	$H^+ + * + e^- \leftrightarrow H*$	Eq. 1
Heyrovsky Step	$H* + H^+ + e^- \leftrightarrow H_2 + *$	Eq. 2
Tafel Step	$H* + H* \leftrightarrow H_2 + 2*$	Eq. 3
Alkaline Volmer Step	$H_2O + * + e^- \leftrightarrow H* + OH^-$	Eq. 4
Alkaline Heyrovsky Step	$H* + H_2O + e^- \leftrightarrow H_2 + OH^- + e^-$	Eq. 5

Thin films of molybdenum (Mo), tungsten (W), niobium (Nb), tantalum (Ta) and vanadium (V) carbides were synthesized, and they were also modified with monolayers (MLs) of Pt or Au. HER electrochemical testing was performed to obtain HER activity, specified by their exchange current density (i_o). DFT is used to calculate the adsorbed free energy change of hydrogen or the hydroxyl group ($\Delta G_{H,}$ ΔG_{OH}) for each surface, directly correlating to HBE or OHBE. To ensure the validity of the obtained HER activity, sample stability is examined by electrochemical stability testing coupled with XPS characterization before and after electrochemical testing. The correlation is then established between the calculated HBEs and OHBEs and their acid and alkaline HER activity (i_o).

4.2 Experimental and theoretical methods

4.2.1 DFT calculations

The Density functional theory (DFT) calculations were carried out using the Vienna Ab initio Simulation Package (VASP)[15]. The plane-waves were conducted with an energy cutoff of 400 eV using projector augmented-wave (PAW) potentials[16]. The Perdew-Wang-91 (PW91) functional with the generalized gradient approximation (GGA) was used to deal with the electronic exchange and correlation energies[17]. For all metal surfaces, a 3×3 (111) unit cell with four layers was used. The transition metal terminated TMC surfaces were modeled using a 3×3 surface slab cell with four bilayers (a bilayer contains a unit of one TM layer and one C layer) of atoms. For the Pt-, Pd-, Au-, Ag-TMC surfaces ((111) surfaces for NbC, TaC, TiC, and VC and (0001) surfaces for WC, W_2C and Mo_2C), the Pt-, Pd-, Au-, Ag-monolayer was deposited on the TMC surfaces. These calculations were done with a 3×3×1 k-point mesh. The bottom two layers of the slab were fixed, and the top two layers were allowed to relax. The Gibbs free energy

change of adsorbed hydrogen (ΔG_H) and the adsorbed hydroxyl group (ΔG_{OH}) were calculated using the equations shown below:

$$\Delta G=\Delta E+\Delta ZPE-T\Delta S$$

where E is the total energy of a species from DFT calculations and defined in the equation below; ZPE and S are the zero point energy and entropy of a species. T=298.15 K.

$$E = E(\text{H-slab}) - E(\text{slab}) - 0.5 \times E(H_2),$$

where E(H–slab) is the total energy of the slab with 1/9 monolayer (ML) hydrogen adsorbed, E (slab) is the total energy of the slab in a vacuum, and $E(H_2)$ is the total energy of hydrogen in the gas phase.

4.2.2 TMC thin films synthesis

All metal foils of tungsten (W), molybdenum (Mo), tantalum (Ta), niobium (Nb), and vanadium (V) (Alfa Aesar, 99.95%) were first cut to correct sizes of 1 cm*1.5 cm. The sized foils were then preconditioned to remove surface grease and oxides.[18] The samples were first sonicated in acetone for fifteen minutes at which point they were cleaned with deionized (DI) water followed by being soaked in 0.3 M NaOH for thirty minutes . Upon rinsing samples with DI water to remove pre-conditioning solutions, the foils samples were immediately inserted into a quartz tube and connected to a furnace equipped with hydrogen (H_2), methane (CH_4) and passivation gas (1% O_2& 99% N_2) flow. For samples of W, Ta, Nb, and V, the carbonization process was carried out at 1273 Kelvin (K) for one hour in a gas flowing environment of 100 mL min^{-1} H_2 and 20 mL min^{-1} CH_4. The temperature was ramped down and held at 1123 K for thirty minutes with a flow of 100 mL $mins^{-1}$ H_2 to remove excess surface carbon. [19] The temperature was then ramped down gradually to room temperature (RT) in a reduced H_2 flow of 70 mL min^{-1} followed by passivation for one hour in a 30 mL min^{-1} 1% O_2/99% N_2 gas environment at RT.

The detailed temperature ramping procedure and steps for reducing surface carbon have been previously described in detail[20]. Regarding the carburization procedure for Mo, the procedure was followed as prescribed in previous literature[21]. In general, unlike ramping to 1273 K, the temperature was only elevated to, and held, at 1123 K for one hour in a gas environment of 42 mL min^{-1} CH_4 and 85 mL min^{-1} H_2. CH_4 was then turned off with reduced H_2 flow of 70 mL min^{-1} during the cooling process followed by the same passivation as described above.

4.2.3 Physical vapor deposition (PVD) of Pt and Au on TMCs

The deposition of Pt, or Au, monolayers (MLs) on prepared TMC thin films were conducted by a PVD method in ultra-high vacuum (UHV) conditions. PVD started with resistively heating tungsten filaments wrapped with 99.99% pure metal sources of Pt, or Au. The metal sources were evaporated and deposited on TMC substrates. The desired number of metal MLs was achieved as a function of deposition time. More specifically, before conducting PVD of Pt, or Au, on TMC surfaces within the UHV chamber, prepared TMCs were dipped in 0.3 M NaOH for fifteen minutes to remove passivated oxide layers, which allowed direct interaction of deposited metals with native TMC surfaces. After unmodified TMC's thin film samples were rinsed with DI water and air dried, they were mounted on a home-made sample holder and loaded in an ultra-high vacuum (UHV) chamber at a pressure of $5*10^{-9}$Torr. The surface characterization and determination of a growth of Pt monolayers were done by x-ray photoelectron spectroscopy (XPS) with an Al X-ray source. The detailed XPS procedure can be found in literature[20]. The fitting procedure for determining these peak areas was explicitly described in our previous work performed on ML Pt-modified WC[22].

4.2.4 Electrochemical measurement

Electrochemical tests were performed at RT both in acid (0.5M H_2SO_4) and alkaline (0.1MKOH) electrolytes in a three-electrode electrochemical cell set-up with graphite (Sigma-Aldrich, 99.995 % trace metal basis) as a counter electrode and a reversible hydrogen electrode (RHE) as a reference electrode. Princeton Applied Research Versa STAT 4 was used as a potentiostat to conduct linear scanning voltammetry (LSV), cyclic voltammetry (VC) and electrochemical impedance spectroscopy (EIS) testing. Thin film samples, as working electrodes, were covered with electroplating tape in a such way that only a 1 cm^2 geometric surface area was exposed to the electrolyte. The electrolyte was purged with Argon (Ar) for fifteen minutes. All electrodes were first cleaned in Ar-saturated acid and alkaline electrolyte with 10 CV cycles between 0.05 and ~ 0.5 V vs. RHE using a scan rate of 100 mV s^{-1}. For Pt and Pd polycrystalline thin films, the CV scan range was set from 0.05V to 1.4 V vs. RHE. Next, the electrolyte was purged with ultra-high purity H_2 gas for twenty minutes. Cathodic LSV testing was conducted starting from 0.15V v.s RHE at a scan rate of 20 mV s^{-1}. Cell resistance was measured at the beginning of each LSV testing using electrochemical impedance spectroscopy (EIS). All reported potentials were obtained after cell resistance correction. The LSV tests were usually performed three times to ensure the reproducibility of the LSV results, and the last LSV curve was used for further data analysis. The total testing time was approximately one hour. After testing, the samples were rinsed in DI water and then air dried for post-HER XPS testing.

The $\log_{10}(i_o)$ of unmodified Pt and Au-modified TMCs were obtained from extrapolation of Tafel plots within the range of current densities between -1 mA cm^{-2} to -4 mA cm^{-2}. The detailed methodology for acquiring i_o was followed as described in literature[23]. Due to extremely fast HER kinetics on the Pt polycrystalline foil, the $\log_{10}(i_o)$ of the HER was obtained from fitting the currents of the HER to the Butler-Volmer equation as suggested in a previous study[10].

4.3 Results and discussion

4.3.1 HER activity for Pt- and Au-modified carbides in acid

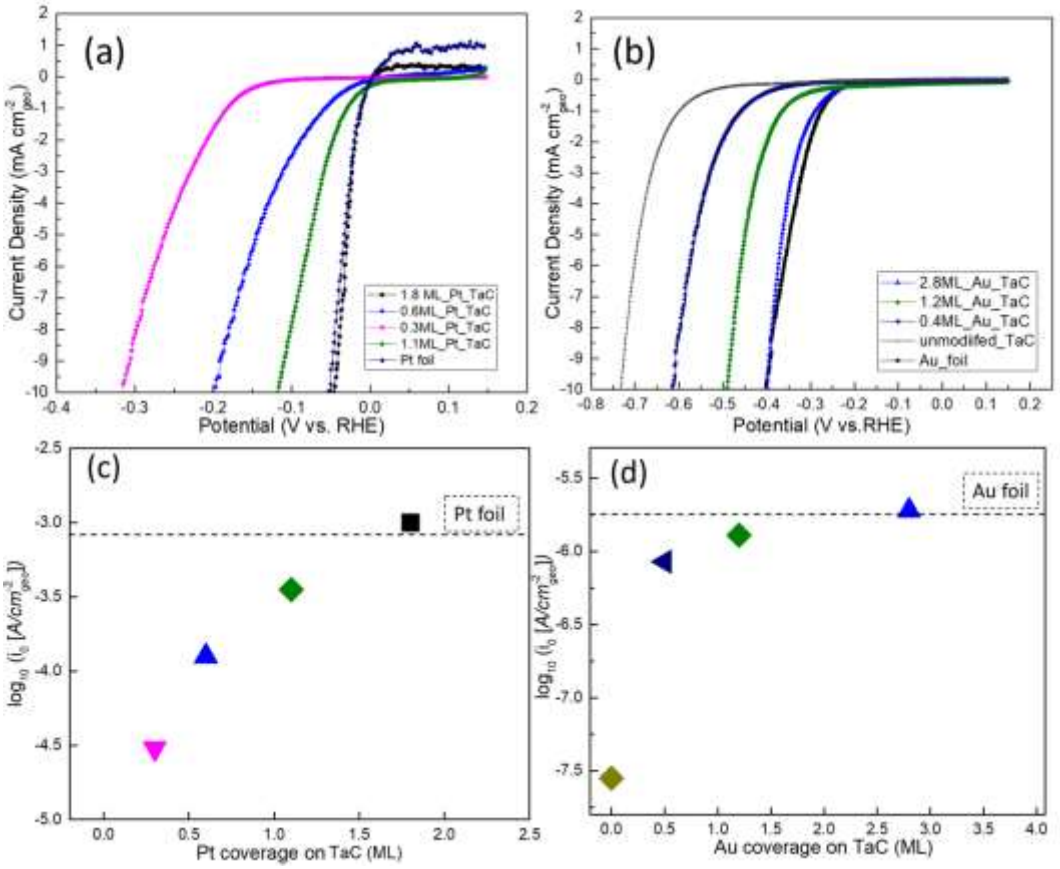

Figure 4.1 Acid HER LSV curves for various MLs Pt-modified TaC (a) and Au-modified TaC (b) in H_2-saturated 0.5 M H_2SO_4; Acid HER activity for Pt and Au foils samples incorporated; LSVs after cell resistance correction at RT and collected at a scan rate of 20 mV s^{-1}; The acid HER activity indicated by $\log_{10}(i_o)$ as a function of the different number of Pt or Au MLs coverage on the TaC substrates shown in (c) and (d), respectively; The current density was normalized by the geometric surface area of the each tested sample.

Many metal-modified carbide thin films have been evaluated experimentally for acid HER and have shown good correlation with DFT-calculated HBEs[24]. Metal-modified TaC and VC thin film HER experiments have not been previously reported and were used here to validate the experimental procedure. Fig. 4.1 illustrates HER current density for various coverage of Pt on TaC (a) and Au on TaC (b) in 0.5 M H_2SO_4 electrolyte. Unmodified TaC was the least active for HER and required more than 650 mV vs. RHE applied potential to reach 5 mA cm^{-2}. As the

Pt and Au coverage increased, the overpotentials required to achieve the same current density decreased. The LSV curve for the 1.8 ML Pt/TaC overlapped with the Pt foil LSV, and the 2.8 ML Au/TaC LSV matched well with the Au foil LSV.

The $\log_{10}(i_o)$ values were obtained from Tafel plots of the LSV data and plotted as a function of Pt coverage (Fig. 4.1c) and Au coverage (Fig. 4.1d) on TaC. These plots show an increase in $\log_{10}(i_o)$ with increased Pt and Au coverage. There was a plateau at the Pt coverage of 1.8 MLs and Au coverage of 2.8 MLs, where i_o was similar to Pt and Au foils. This result is expected, because the DFT-calculated HBEs for Pt/TaC and Au/TaC are similar to that of bulk Pt and bulk Au, respectively. This behavior is similar to previous reports for various metal-modified carbides[25–28]. The same trends were also observed for Pt- and Au-modified VC in acid (see SI). Acid HER $\log_{10}(i_o)$ for the tested samples are summarized in Table 4.1 along with a complete list of acid HER $\log_{10}(i_o)$ for metals, carbides, and metal-modified carbides reported in literature[24]. Bold-face values are from literature, normal font values are experimental observations from this work.

Table 4.1 The summary of $\log_{10}(i_o)$ in 0.5 M H_2SO_4 and in 0.1 M H_2SO_4;The values in italics were from published results summarized in literature[24].

catalyst	**$\log_{10}(i_o$ [A cm^{-2}]) in 0.5 M H_2SO_4**	**$\log_{10}(i_o$ [A cm^{-2}]) in 0.1 M KOH**
Ag	***-6.3***	
Ag/NbC	***-6.3***	
Au	***-5.75***	-5
Au/Mo_2C	***-5.6***	-5.47
Au/NbC		-6.73

Au/TaC	-6.1	-5.81
Au/VC	-6.15	
Au/WC	***-5.1***	
Mo_2C	***-6.1***	-5.66
NbC	***-6.8***	-6.2
Pd	***-3.2***	-4.12
Pd/Mo_2C	***-4***	
Pd/NbC	***-4.4***	
Pd/WC	***-3.7***	
Pt	***-3.1***	-3.72
Pt/Mo_2C	***-3.2***	-4.5
Pt/NbC	***-3.5***	-4
Pt/TaC	-3.41	-4.52
Pt/TiC	***-3.15***	
Pt/VC	-3.65	-4.6
Pt/W_2C	***-3.5***	
Pt/WC	***-3.3***	-4.1
TaC	-7.55	-7.03
TiC	***-5.8***	
VC	-7.11	-6.09
W_2C	***-5.75***	
WC	***-5.75***	-5.63

4.3.2 HER activity and stability for metal-modified carbides in alkaline

In alkaline electrolyte, the HER activity and stability were examined for five different TMCs, including TaC, VC, Mo_2C, WC and NbC with these surfaces modified with Au, Pt and Pd overlayers. Pt/TaC and Au/TaC are first examined to determine if the procedures demonstrated for acid HER are applicable to alkaline HER. The alkaline HER curves for Pt-modified TaC (Fig. 4.2a) fell increasingly closer to the Pt foil with increasing Pt coverage. The trend was similar for Au-modified TaC in alkaline HER, as shown in Fig. 4.2b. Figure 4.2c and 2d show acquired $\log_{10}(i_o)$ values for different MLs of Pt or Au on TaC. They are consistent with the trend indicated by the LSV curves. It should also be noted that, compared to acid, the Pt foil in alkaline illustrated slower HER kinetics, indicated by the LSV curves and $\log_{10}(i_o)$ values. To achieve alkaline HER current density of 5mA cm^{-2}, Pt foil required the overpotential of approximately 130 mV (Fig. 4.2a) with $\log_{10}(i_o)$ of -3.8 (Fig. 4.2b), while it only required 25 mV (Fig. 4.1a) with $\log_{10}(i_o)$ of -3.1 (Fig. 4.1c) in acid. These results are similar to the literature[27]. The metal-modified TaC results in alkaline are similar to those in acid, so the same metal modification procedures were used to evaluate alkaline HER activity for other metal-modified carbides.

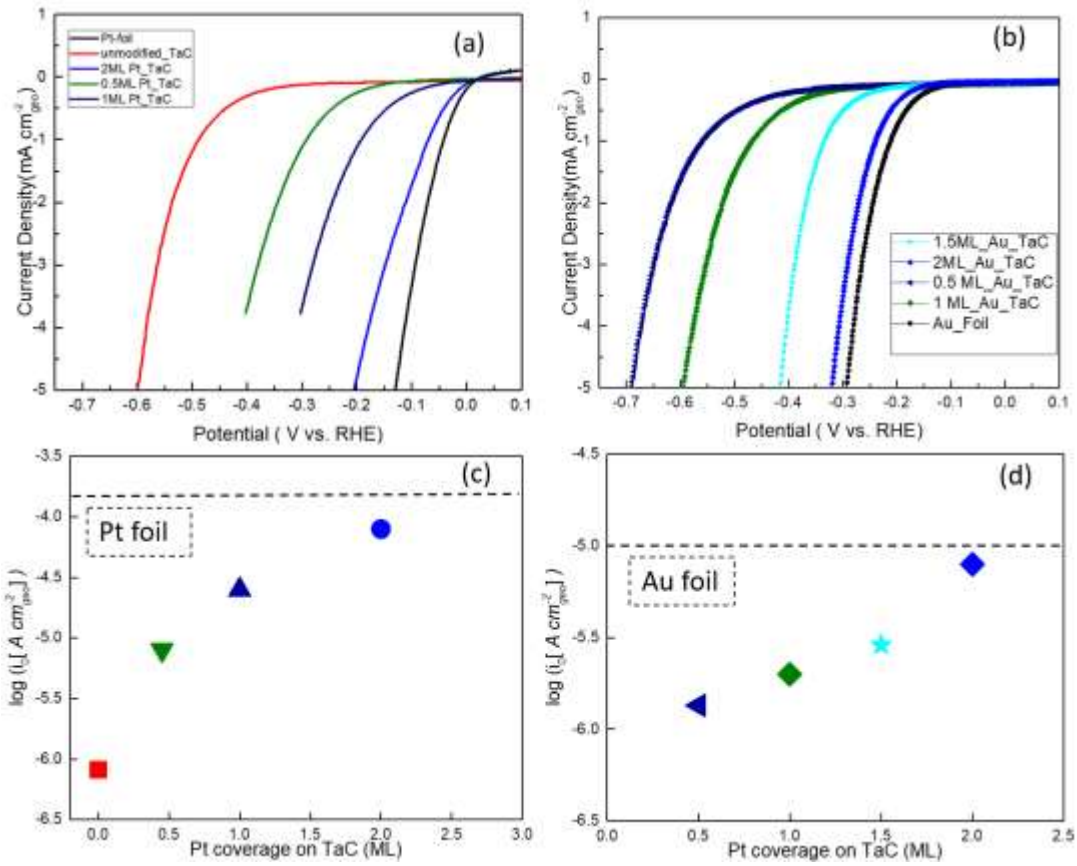

Figure 4.5 Alkaline HER LSV curves for various MLs Pt-modified TaC (a) and Au-modified TaC (b) in H_2-saturated 0.1 M KOH; Alkaline HER activity for Pt and Au foils samples incorporated; LSVs after cell resistance correction at RT and collected at a scan rate of 20 mV s^{-1}; The alkaline HER activity indicated by $\log_{10}(i_o)$ as a function of the different number of Pt or Au MLs coverage on the TaC substrates shown in (c) and (d), respectively; The current density was normalized by the geometric surface area of the each tested sample.

Catalyst stability during alkaline HER testing was examined by XPS measurements before and after electrochemical testing. All Pt-modified TMCs and Au-modified TMCs were considered as stable catalysts during alkaline HER tests. Ta4f and Pt4f XPS spectra for Pt-modified TaC, is shown as an example in Fig. 4a. The Pt/Ta signal ratios decreased by approximately 20% after one-hour test in alkaline, shown in Fig. 4.3c. The signal decrease could be either attributed to Pt overlayer dissolution or agglomeration[29]. To determine the metal coverage reduction mechanism, an additional hour of HER testing containing CV cleaning with three repeating LSV measurements was further performed on the spent 1 ML Pt/TaC sample. If the Pt dissolution resulted in the decrease in the Pt/Ta4f signal ratio, continuing decrease in the

ratio from one-hour testing to two-hour testing should be detected[29]. However, Fig. 4.3a revealed that no further decrease in Pt/Ta signal ratios, indicating the decrease in the XPS ratios more likely due to Pt agglomerations.

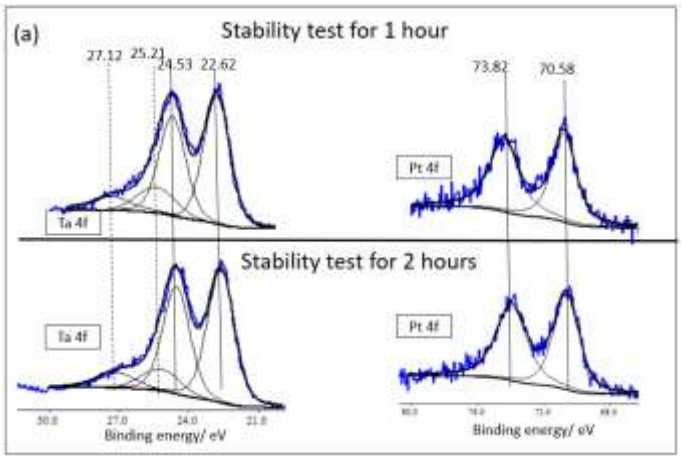

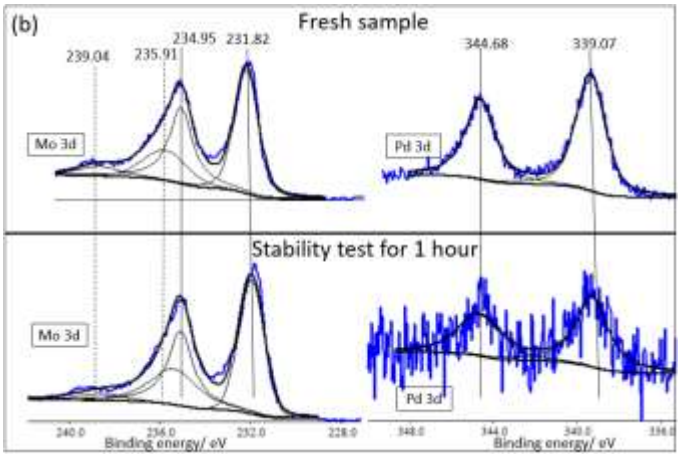

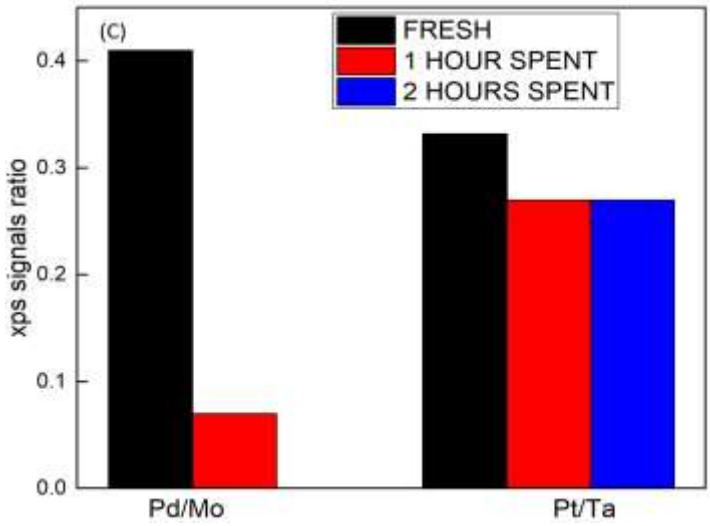

Figure 4.6 XPS 4f signals for Ta4f and Pt4f after one hour and two hours HER testing in alkaline for 1 ML Pt-modified TaC shown in (a); XPS 4f signals for Mo3d and Pd3d of the fresh sample and after one hour HER testing in alkaline for 1 ML Pd-modified Mo_2C shown in (b); Pd/Mo and Pt/Ta XPS signal ratios before and after alkaline HER testing for Pd-modified Mo_2C and Pt-modified TaC in (c), respectively.

Unlike Pt-modified TaC, XPS results indicated that Pd-modified Mo_2C was not stable during alkaline HER test (Fig. 4.3b), substantiated with more than 80% decrease in Pd/Mo signal ratios (Fig. 4.3c). These results were typical for all Pd-modified TMCs. Therefore, for alkaline HER activity, only Pt/TMCs and Au/TMCs were used to calculate $\log_{10}(i_0)$. The alkaline HER $\log_{10}(i_0)$ values for stable samples are summarized in Table 4.1.

4.3.3 Correlation between HER activity and possible descriptors in acid and alkaline

Table 4.2 DFT calculations of ΔG_H on Pt, Pd, Au, Ag-modified carbides, Pt(111), Pd(111), Au(111), Ag(111) and unmodified carbides surfaces.

Category	Surfaces	ΔG_H (eV)	ΔG_{OH} (eV)
Pt/carbides	Pt/Mo2C(0001)	0.01	-2.39
	Pt/NbC(111)	−0.28	-2.41
	Pt/TaC(111)	−0.07	-2.51

	Pt/TiC(111)	−0.03	
	Pt/VC(111)	0.02	-2.26
	Pt/W2C(0001)	0.09	
	Pt/WC(0001)	−0.13	-2.81
Pd/carbides	Pd/Mo2C(0001)	−0.03	
	Pd/NbC(111)	−0.19	
	Pd/WC(0001)	−0.19	
Au/carbides	Au/Mo2C(0001)	0.48	-2.39
	Au/NbC(111)	0.57	-2.31
	Au/TaC(111)	0.47	-2.51
	Au/VC(111)	0.51	
	Au/WC(0001)	0.14	
Ag/carbides	Ag/NbC(111)	0.44	
Bulk metals	Ag(111)	0.37	
	Au(111)	0.36	
	Pd(111)	-0.36	-2.34
	Pt(111)	-0.26	-2.21
Unmodified-carbides	Mo2C(0001)	−0.75	-4.6
	NbC(111)	−0.90	-4.85
	TaC(111)	−0.99	-4.96
	TiC(111)	−0.96	
	VC(111)	−0.84	-4.91
	W2C(0001)	−0.60	

WC(0001)	−0.81	-4.19

The Gibbs free energy change of adsorbed hydrogen (ΔG_H) was calculated by DFT, as shown in Table 4.2. Based on previously published results[13,24,28] , HBE had been reported as an effective descriptor for a catalyst's HER activity in acid. It was demonstrated through a volcano shaped correlation between the HER activity for examined catalysts with the respective calculated HBE. Figure 4.3 shows a volcano shaped relationship between acid HER activity (summarized in Table 4.1) on the vertical axis and ΔG_H (Table 4.2) on the horizontal axis. Newly synthesized catalysts including unmodified TaC, VC and their Pt- and Au-modified counterparts fit well on the volcano plot, as shown in Fig. 4.3 These results are expected, because the acid HER trend is well-established for metal-modified carbides.

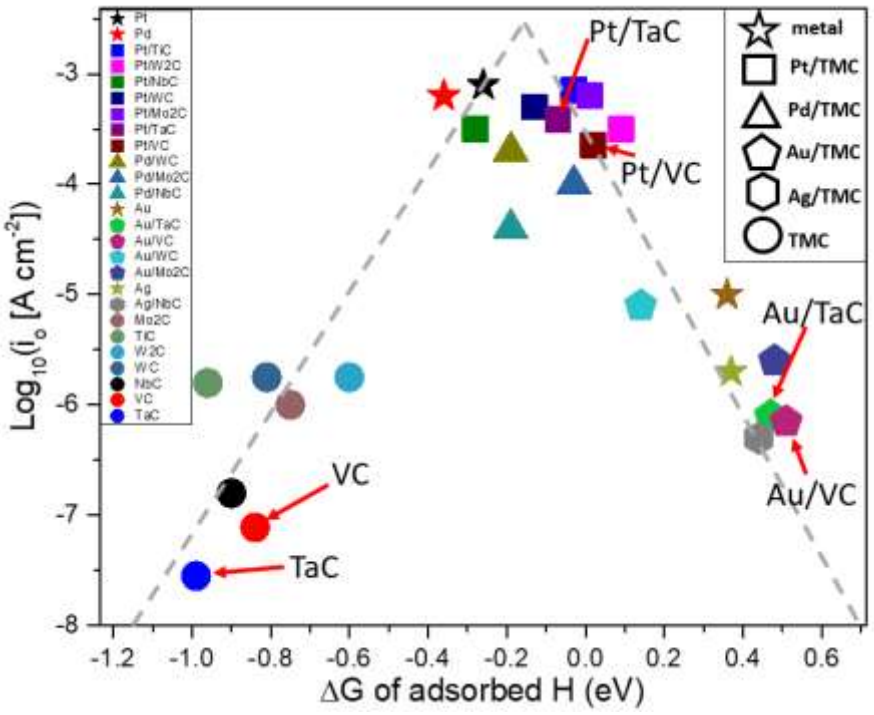

Figure 4.4 $\log_{10}(i_o)$ for unmodified, metals-modified TMCs and monometallic metals as a function of corresponding ΔG_H in 0.5 M H_2SO_4; Arrow pointed data were measured for this manuscript and other $\log_{10}(i_{0s})$ results were from published results summarized in literature[24].

The descriptor for alkaline HER has been under debate due to the differences in proposed mechanism for acid and alkaline electrolyte, as discussed in the introduction. Therefore, the Gibbs free energy change of the adsorbed hydroxyl group (ΔG_{OH}) was calculated and summarized in Table 4.2. Since Pt and Au-modified TMCs were shown to be stable in alkaline HER conditions (Fig. 4.3), they were used to examine possible correlations between alkaline HER activity ($\log_{10}(i_o)$) and either ΔG_H (Fig. 4.5a) or ΔG_{OH} (Fig. 4.5b). The alkaline HER activity for metal-modified carbides forms a volcano-shaped relationship with ΔG_H, as shown in Fig. 4.5a. This indicates that ΔG_H is, indeed, an important descriptor for alkaline HER activity on metal-modified carbides. According to Fig. 4.5a, the best HER activity in alkaline, obtained on the Pt surface, should correspond to the most appropriate ΔG_H, locating at the apex. Based on the Sabatier principle[30], when hydrogen atoms were bound to surfaces more strongly than Pt (ΔG_H<Pt) , the desorption process was less favored thus causing the decrease in HER activity. The trend was illustrated by unmodified TaC, Mo_2C, NbC, VC, and TaC. When hydrogen atoms were bound to surfaces less strongly than Pt (ΔG_H>Pt), the hydrogen surface coverage was relatively lower. As a result, higher energy (higher overpotential) was required to reach the same alkaline HER activity. The trend was formed by the electrocatalysts of Au-modified NbC, TaC and Mo_2C.

Unlike the volcano-shaped relationship formed with ΔG_H, ΔG_{OH} has a much weaker correlation with alkaline HER activity (Fig. 4.5b). The correlation between the alkaline HER activity and ΔG_{OH} appeared to a triangle shape. Au-modified carbides have similar OHBEs as Pt and Pt-modified carbides, but the Au/TMCs alkaline exchange current densities are 2 or 3 orders of magnitude lower than their Pt counterparts. This indicates that OHBE is not a good descriptor for alkaline HER on carbides and metal-modified carbides. It also suggests that the adsorbed

hydroxyl group does not play a direct role in the rate determining step of alkaline HER kinetics on these surfaces. To conclude, compared to ΔG_H, ΔG_{OH} should be considered as a less effective descriptor for alkaline HER of examined TMC-based catalysts. Thus, the decreased HER activity for metal-modified carbides in alkaline compared to acid cannot be determined by HBE and OHBE alone. Instead it is likely that the alkaline environment influences the water structure or hydrogen stability, as suggested by some other studies on Pt surfaces.[12–14]

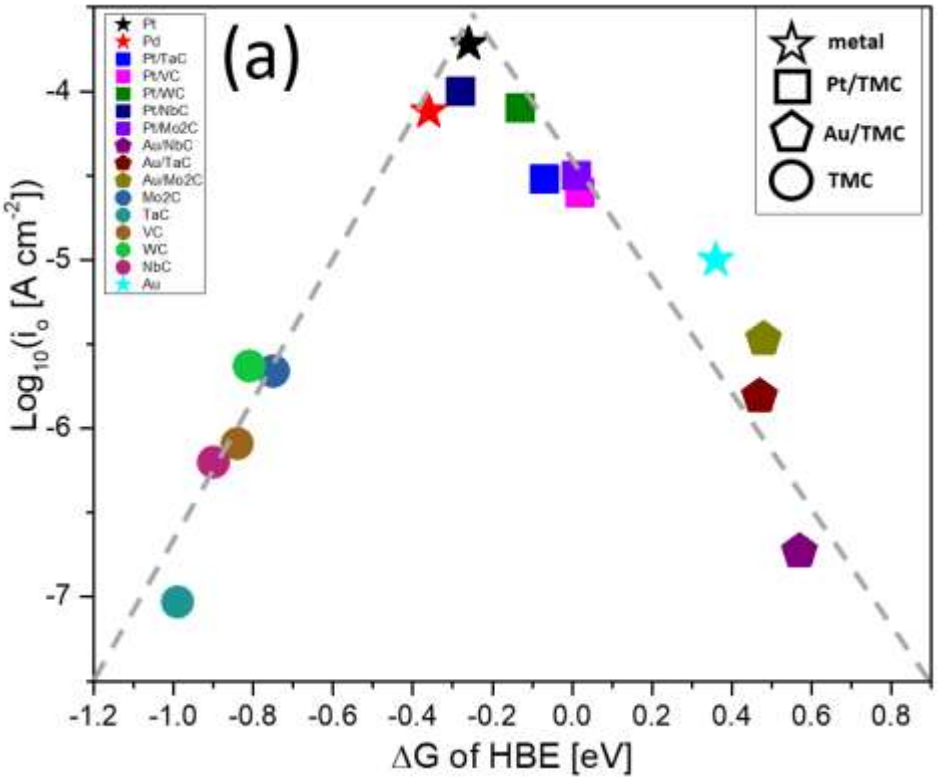

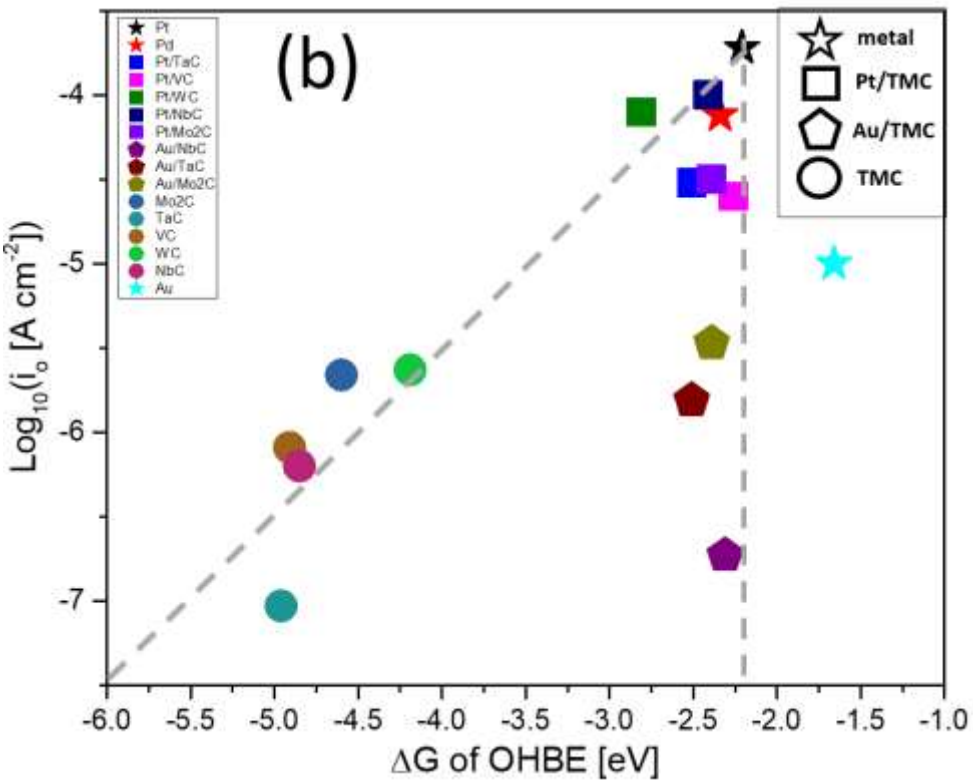

Figure 4.5 $\log_{10}(i_o)$ for unmodified, Pt- or Au-modified TMCs, Pt and Pd as a function of respective ΔG_H (a) or ΔG_{OH} (b) in 0.1 M KOH.

4. Conclusions

Pt- and Au-modified TaC and VC catalyst are active and stable catalysts for acid HER, and they closely adhere to the previously established acid HER volcano curve. The same synthesis techniques were used to test a variety of metal-modified carbides under alkaline HER conditions, and the results correlated strongly with DFT-calculated HBE. This is the first example of a volcano trend on metal-modified carbides for alkaline HER, and it shows that HBE is a good descriptor for this class of materials under both alkaline and acid conditions. The hydroxyl binding energy on metal-modified carbide surfaces was also calculated, but there was a weak correlation between those values and measured alkaline HER activity. This suggests that the adsorbed hydroxyl group does not directly participate in the rate determining step of the alkaline

HER. To understand the difference in alkaline versus acid HER activity, future studies should aim to describe the influence of alkaline electrolyte on the hydrogen binding energy.

References

(1) Tackett, B. M.; Sheng, W.; Chen, J. G. *Joule* **2017**, *1* (2).

(2) Porosoff, M. D.; Yan, B.; Chen, J. G. *Energy Environ. Sci.* **2016**, *9* (1), 62–73.

(3) Olah, G. A.; Goeppert, A.; Prakash, S. G. K. *Beyond Oil and Gas: The Methanol Economy, Second updated and enlarged edition*; Wiley-VCH Verlag GmbH, 2009.

(4) Trotochaud, L.; Young, S. L.; Ranney, J. K.; Boettcher, S. W. *J. Am. Chem. Soc.* **2014**, *136* (18), 6744–6753.

(5) McCrory, C. C. L.; Jung, S.; Peters, J. C.; Jaramillo, T. F. *J. Am. Chem. Soc.* **2013**, *135* (45), 16977–16987.

(6) Nørskov, J. K.; Bligaard, T.; Logadottir, A.; Kitchin, J. R.; Chen, J. G.; Pandelov, S.; Stimming, U. *J. Electrochem. Soc.* **2005**, *152* (3), J23.

(7) Trasatti, S. *J. Electroanal. Chem. Interfacial Electrochem.* **1972**, *39* (1), 163–184.

(8) Esposito, D. V; Hunt, S. T.; Stottlemyer, A. L.; Dobson, K. D.; McCandless, B. E.; Birkmire, R. W.; Chen, J. G. *Angew. Chem. Int. Ed. Engl.* **2010**, *49* (51), 9859–9862.

(9) Wan, W.; Tackett, B. M.; Chen, J. G. *Chem. Soc. Rev.* **2017**, *46* (7).

(10) Sheng, W.; Myint, M.; Chen, J. G.; Yan, Y. *Energy Environ. Sci.* **2013**, *6* (5), 1509.

(11) Li, J.; Ghoshal, S.; Bates, M. K.; Miller, T. E.; Davies, V.; Stavitski, E.; Attenkofer, K.; Mukerjee, S.; Ma, Z.-F.; Jia, Q. *Angew. Chemie Int. Ed.* **2017**.

(12) Intikhab, S.; Snyder, J. D.; Tang, M. H. *ACS Catal.* **2017**, 8314–8319.

(13) Sheng, W.; Zhuang, Z.; Gao, M.; Zheng, J.; Chen, J. G.; Yan, Y. *Nat. Commun.* **2015**, *6*, 5848.

(14) Durst, J.; Siebel, A.; Simon, C.; Hasché, F.; Herranz, J.; Gasteiger, H. A. *Energy Environ. Sci.* **2014**, *7* (7), 2255.

(15) Kresse, G.; Hafner, J. *Phys. Rev. B* **1993**, *47* (1), 558–561.

(16) Kresse, G.; Joubert, D. *Phys. Rev. B* **1999**, *59* (3), 1758–1775.

(17) Perdew, J. P.; Chevary, J. A.; Vosko, S. H.; Jackson, K. A.; Pederson, M. R.; Singh, D. J.; Fiolhais, C. *Phys. Rev. B* **1992**, *46* (11), 6671–6687.

(18) Weidman, M. C.; Esposito, D. V.; Hsu, I. J.; Chen, J. G. *J. Electrochem. Soc.* **2010**, *157* (12), F179.

(19) Kimmel, Y. C.; Esposito, D. V.; Birkmire, R. W.; Chen, J. G. *Int. J. Hydrogen Energy*

2012, *37* (4), 3019–3024.

(20) Kimmel, Y. C.; Xu, X.; Yu, W.; Yang, X.; Chen, J. G. *ACS Catal.* **2014**, *4* (5), 1558–1562.

(21) Weidman, M. C.; Esposito, D. V.; Hsu, Y.-C.; Chen, J. G. *J. Power Sources* **2012**, *202*, 11–17.

(22) Esposito, D. V.; Hunt, S. T.; Kimmel, Y. C.; Chen, J. G. *J. Am. Chem. Soc.* **2012**, *134* (6), 3025–3033.

(23) Sheng, W.; Myint, M.; Chen, J. G.; Yan, Y. *Energy Environ. Sci.* **2013**, *6* (5), 1509.

(24) Wan, W.; Tackett, B. M.; Chen, J. G. *Chem. Soc. Rev.* **2017**, *46* (7), 1807–1823.

(25) Esposito, D. V.; Hunt, S. T.; Kimmel, Y. C.; Chen, J. G. *J. Am. Chem. Soc.* **2012**, *134* (6), 3025–3033.

(26) Esposito, D. V.; Chen, J. G. *Energy Environ. Sci.* **2011**, *4* (10), 3900.

(27) Tackett, B. M.; Kimmel, Y. C.; Chen, J. G. *Int. J. Hydrogen Energy* **2016**, *41* (14), 5948–5954.

(28) Zhang, Q.; Tackett, B. M.; Wu, Q.; Chen, J. G. *ChemElectroChem* **2016**.

(29) Tackett, B. M.; Kimmel, Y. C.; Chen, J. G. Manuscript submitted for publication.

(30) Medford, A. J.; Vojvodic, A.; Hummelshøj, J. S.; Voss, J.; Abild-Pedersen, F.; Studt, F.; Bligaard, T.; Nilsson, A.; Nørskov, J. K. *J. Catal.* **2015**, *328*, 36–42.

5. PT-MODIFIED TANTALUM CARBIDE AS AN EFFICIENT ELETROCATALYST FOR ETHANOL OXIDATION IN ACID AND ALKALINE ELETROLYTES

5.1 Introduction

Increasing energy demand and environmental concerns of continuous fossil fuel consumption have stimulated alternative energy research.[1–3] Low-temperature fuel cells have attracted extensive attention due to their high efficiency and broad applications in the transportation sector.[4] Although hydrogen fuel cells have been studied extensively,[5] the utilization of hydrogen faces challenges in storage and transportation.[6] Oxygenates, such as methanol and ethanol, can generate energy in direct alcohol fuel cells (DAFCs). They are more commercially favored over hydrogen due to the compatibility with the existing storage and transportation infrastructure.[7] Ethanol has several advantages over methanol, including higher specific

energy density and non-toxicity. Ethanol also has competitive market prices due to mass production from a variety of feedstocks. [8–10]

The most promising and active catalysts for the ethanol oxidation reaction (EOR) in DAFCs are Pt and Pt-based alloys (e.g. Pt-Ru).[3] However, the carbonyl-containing and/or carbon monoxide (CO) intermediates bind strongly to Pt surfaces and poison the catalysts at low potentials (e.g., below 0.6 V vs. RHE).[11,12] Higher operating potentials can avoid poisoning but decrease the cell efficiency. Additionally, the scarcity of Pt-group metals potentially prevents Pt-group catalysts from being commercialized on a large scale.[13] Supporting Pt on transition metal carbides (TMC) has shown promise in alleviating these problems. For example, monolayer (ML) Pt supported on tungsten carbide (WC) has shown an enhanced CO tolerance by reducing the CO binding energy on Pt/WC through electronic structure modification,[14–17] which would potentially enhance the EOR activity. ML Pt/TMCs can also significantly reduce the Pt loading in electrocatalysts.[18,19]

Although ML Pt/WC has shown good EOR performance in acid[17], WC would be oxidized at higher voltages in alkaline electrolyte[20], making it unsuitable for alkaline EOR. Given the fact that EOR activities on Pt are reported to be several orders of magnitude higher in alkaline than in acid [21,22], it is important to explore stable Pt-modified TMC catalysts for alkaline EOR. Tantalum carbide (TaC) is a qualified candidate due to its higher stability than WC in alkaline.[20] It is possible that TaC increases the hydroxyl adsorption capacity and thus facilitates the oxidation of CO with adsorbed OH. It has been reported in literature that the formation of adsorbed hydroxyl over TMC is thermodynamically favored in both experiments and DFT calculations.[23–25] In this work, EOR activity of ML Pt/TaC thin films and 1.5 wt% Pt/TaC powder catalysts were measured by electrochemical methods. The stability was examined by X-ray photoelectron spectroscopy (XPS) measurements for pre- and post- testing thin film samples. The EOR mechanism on Pt/TaC was further investigated by *in-situ* infrared reflection absorption spectroscopy (IRRAS) and density functional theory (DFT) calculations.

5.2 Experimental and theoretical methods

5.2.1 Synthesis of ML Pt/TaC thin films

Ta foils (Alfa Aesar, 0.25 mm thick annealed 99.95%) were rinsed in acetone and deionized (DI) water followed by being soaked in 0.3 M NaOH for 15 minutes to remove impurities. They were inserted into a quartz tube furnace in a gas flowing environment of 100 mL min^{-1} H_2 and 20 mL min^{-1} CH_4. The Ta foils were slowly heated to 1273 K and kept at the temperature for one hour to carburize the foils, using a temperature ramping procedure described in literature [20]. After the carburization, the temperature was held at 1123 K for 30 minutes with a flow of 100 mL min^{-1} H_2 to remove excess surface carbon.[26] The furnace was gradually cooled down for eight hours in a reduced flow of 70 mL min^{-1} H_2 followed by the passivation in a flow of 30 mL min^{-1} 1% O_2/99% N_2 for one hour at room temperature. Pt physical vapor deposition (PVD) on TaC thin films was performed in an ultra-high vacuum ($5x10^{-9}$Torr) system equipped with XPS. The Pt PVD process and XPS fitting procedures for peak integrations were described in previous work.[19]

5.2.2 Synthesis of 1.5wt% Pt/TaC catalyst

The wet impregnation method was used to synthesize 1.5 weight percent (wt%) Pt on commercial TaC (Sigma-Aldrich) catalyst. A target amount of $Pt(NH_3)_4(NO_3)_2$ (Tetra-ammine-platinum(II)nitrate from Sigma-Aldrich) as the Pt precursor were dissolved in 10ml of DI water. The solution was then agitated at room temperature (RT) for five hours with a magnetic stirrer. Then 200 mg commercial TaC powder were added slowly while the solution continued stirring. After twelve hours, the solution was dried on the stirrer at 383 K in air for five hours followed by calcination in a 40 mL min^{-1} H_2 flow environment. The temperature was raised to 673 K with a ramping rate of 2 K min^{-1} and held for one hour. The sample was cooled to RT under the same gas environment and then passivated in 1% O_2/99% N_2.

5.2.3 Electrochemical measurements and stability tests

Regarding working electrode preparation for thin films, 1 cm^2 geometric surface area was defined with electroplating tape with the backsides completely covered. In preparation of working electrodes from powder catalysts for electrochemical testing, 1.5 wt% Pt/TaC electrocatalyst ink was made with 29.16 mg of catalyst samples dispersed in 2.47 mL DI water, 2.47 mL isopropanol, and 0.0252 mL Nafion 117 solution (Sigma–Aldrich). The ink was then sonicated in an ice bath for one hour. For the ink of commercial 40 wt% Pt/Vulcan carbon, 17.5 mg commercial 40 wt% Pt/Vulcan carbon powder was dispersed in 2.458 mL DI water, 2.458 mL isopropanol and 0.0252 mL Nafion 117 solution.

Electrochemical testing for ethanol oxidation were carried out at RT in acid (0.05M H_2SO_4) and alkaline (0.1MKOH) electrolytes. Princeton Applied Research Versa STAT 4 was used as a potentiostat to conduct cyclic voltammetry (CV) and chronoamperometry (CA) testing. Electrochemical measurements were carried out with, and without 1M ethanol (CH_3CH_2OH) in a three-electrode, single-cell set-up with graphite (Sigma-Aldrich, 99.995 % purity) as a counter electrode and a reversible hydrogen electrode (RHE, Hydroflex) as a reference electrode. The working electrode was first cycled in Ar-purged pure acid or base without the presence of ethanol in a cyclic voltammetry (CV) between 0.1 and 1 V vs. RHE using a scan rate of 50 mV s^{-1}. The purpose of the CV scans in pure high or low pH electrolyte was to clean the electrode surface. Then EOR CV testing was conducted in the presence of ethanol at a scan rate of 50 mV s^{-1} for 5 scans in the range of 0.1 to 1 V vs. RHE. It was immediately followed by chronoamperometry (CA) testing at a potential of 0.6V vs. RHE for one hour. The cell resistance was measured at the beginning of the CV scan by using electrochemical impedance spectroscopy (EIS). All reported potentials were corrected by the cell resistance accordingly. After the thin film surfaces were tested,

it was taken out from the solution and cleaned with DI water. After being dried, the post-testing samples were put into the UHV system for XPS measurements.

The electrochemical linear scanning voltammetry (LSV) for working electrodes made from powder samples was conducted in acid and alkaline ethanol electrolyte at the scan rate of 50 mV s^{-1}. CA testing followed the same procedure as described above for model thin films. The rotation rate of 1000 rotations per mins (rpm) was used for on glassy carbon electrode with deposited powder ink. The current densities for the powder catalysts were corrected by the cell resistance and normalized by their respective ECSA based on copper UPD.

5.2.4 In-situ infrared reflection absorption spectroscopy (IRRAS)-LSV

In-situ IRRAS-LSV measurements were carried out with a Nicolet iS50 FT-IR spectrometer equipped with an A-type MCT detector cooled with liquid nitrogen. *In situ* IRRAS studies were carried out with a Nicolet iS50 FT-IR spectrometer equipped with an A-type MCT detector cooled with liquid nitrogen. An unpolarized light beam was used with a resolution of $4cm^{-1}$ and averaged 288 scans for each spectrum. Absorbance was defined as $A= -\log(R/R_o)$ where R and R_o are the reflected IR intensities of sample and reference single beam spectrum, respectively. A ZnSe hemisphere was used as the IR window that the working electrodes were pressed against. In order to minimize the effect of artifacts on the collected IR spectra, the detecting chamber and spectrometer were purged with Argon for at least two hours until the intensity of gaseous CO_2 dropped below $1e^{-4}$ and stabilized at that level.

The working electrode were made from depositing the appropriate amount of 1.5 wt% Pt/TaC catalyst ink or commercial 40 wt% Pt/C ink on glassy plates. Pt loading were kept the same on the glassy plates for fair comparisons. Electrolytes contained either 0.05M H_2SO_4/1M ethanol or 0.1M KOH/1M ethanol. In both acid and alkaline electrolytes, sample spectra were collected from 0.05 V to 1 V vs. RHE at a scan rate of 1 mV s^{-1}.

5.2.5 DFT calculations

DFT calculations were carried out using the Vienna *Ab-Initio* Simulation Package (VASP) code[27]. The electronic ion interaction was modeled by the projector augmented wave (PAW) method[28]. The Perdew-Wang-91 (PW91) functional[29] with the generalized gradient approximation was employed to deal with the electronic exchange and correlation. The kinetic wave cutoff energy was set at 400 eV to describe the electronic wave functions. The Brillouin-zone integration was sampled using a 3×3×1 Monkhorst-Pack k-points grid with a Gaussian smearing of 0.1eV. The Pt(111) and Pt/TaC(111) surfaces were modeled by a four-layer 3×3 super-cell with the coverage of selected adsorbates of 1/9 monolayer. For the Pt/TaC(111) surface, a Pt monolayer was deposited on the TaC(111) surface. The bottom two layers are fixed, and the top layers were allowed to relax. A vacuum layer of 15 Å was added perpendicular to the slab to avoid artificial interactions between the slab and its periodic images.

The binding energies (BE) for all intermediates on the surfaces are defined as follows:

$$BE = E_{adsorbate/surface} - E_{adsorbate} - E_{surface} \quad (1)$$

where $E_{adsorbate/surface}$ is the total energy of the adsorbate together with the surface, $E_{adsorbate}$ is the total energy of the free adsorbate in the gaseous phase, and $E_{surface}$ is the total energy of the surface.

5.3. Results and discussion

5.3.1 Electrochemical studies of Pt/TaC thin films

The Pt-modified TaC thin films were prepared as model surfaces for electrochemical and stability testing. The CV results for 1 ML Pt-modified TaC surfaces in 0.05M H_2SO_4 and 0.1M KOH are shown in Fig. 5.1A and B, respectively. The CV results in acid and alkaline solutions without ethanol showed no oxidation peaks, indicating that 1ML Pt/TaC was stable at least up to

1V vs. RHE. In the presence of 1M ethanol in acid or alkaline electrolyte, two distinctive peaks were observed in the forward (anodic) and reverse (cathodic) scans for the Pt/TaC surfaces, characteristic of ethanol oxidation.[12,21,30]

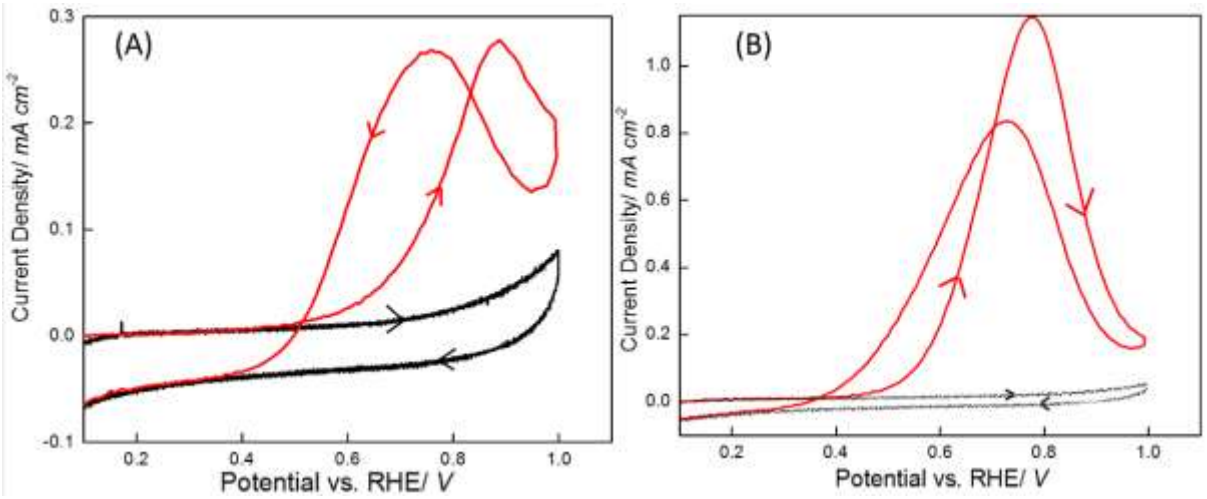

Figure 5.1 CV scans for 1 MLs Pt/TaC at a scan rate of 50 mV S^{-1}, shown in red collected in 0.05 M H_2SO_4/1 M ethanol while the CV scan shown in black collected in only 0.05 M H_2SO_4 (A); shown in red collected in 0.1 M KOH/1 M ethanol while the CV scan shown in black collected in only 0.1 M KOH (B); The arrow indicating the corresponding part of each plot to forward scan and backward scan, respectively.

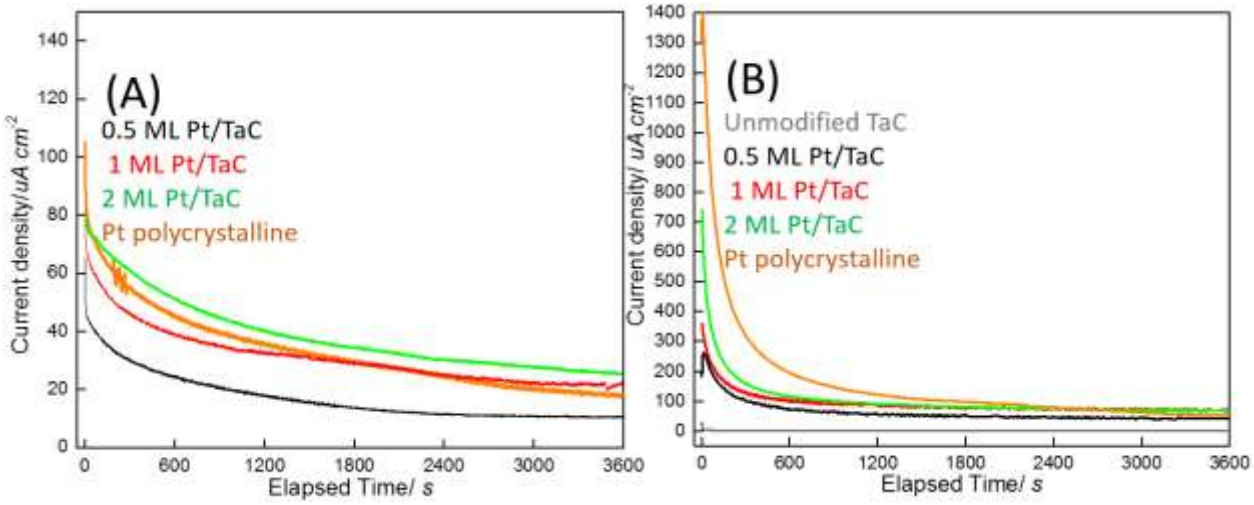

Figure 5.2 CA scans (A) in 0.05M H_2SO_4/1M ethanol and CA scans (B) in 0.1M KOH/1M ethanol of 0.5 ML Pt/TaC at 0.6V v.s RHE for one hour; The catalyst of unmodified TaC shown in grey color, 0.5 ML Pt/TaC in black, 1 ML Pt/TaC in green, 2 ML Pt/TaC in red and Pt bulk in orange; The current densities were normalized by the geometric surface area of the TaC thin films.

In order to compare the activity of Pt-modified TaC with different Pt coverage, EOR CA results for 0.5 ML, 1.0 ML, 2.0 ML Pt-modified TaC and Pt polycrystalline surfaces in acid and

alkaline are compared in Fig. 5.2. The acid EOR steady-state current density obtained at the potential of 0.6V vs. RHE for one hour (Fig. 5.2A) indicated that the activity increased along with an increase in the number of Pt overlayers. Among all tested samples, the highest activity was obtained by 2 ML Pt/TaC in acid. The 1 ML Pt/TaC film exhibited equivalent EOR activity as the Pt film. It is worth noting that the current density in Fig. 5.2 was normalized by geometric surface area of the low surface area thin films rather than their ECSAs, because it was difficult to use traditional ECSAs measurement methods (e.g. Copper stripping or H- UPD) to obtain statistically meaningful results for the low surface area Pt/TaC thin films. The ECSA-normalized EOR activity comparison for Pt-modified TaC and Pt bulk is later discussed in high surface area powder catalysts.

In alkaline (Fig. 5.2B) the activity for 1 and 2 ML Pt/TaC showed similar steady-state activity as the polycrystalline Pt film, while an unmodified TaC surface resulted in no EOR. The comparison of steady-state EOR current density in acid (Fig. 5.2A) and alkaline (Fig. 5.2B) indicated that the high pH environment resulted in an enhanced EOR activity. At 0.6 V vs. RHE, the EOR activity for the 2 ML Pt/TaC surface was 110 μA cm^{-2} in alkaline while it was only 35 μA cm^{-2} in acid. The enhanced EOR activity in alkaline was also reported on the Pt surface. The enhanced EOR activity for the MLs Pt/TaC surfaces in high pH may be attributed to the ease of ethoxy formation and the high hydroxide (OH^-) concentration as oxygen-donating species.[12,21,22,31] The absence of bisulfate poisoning in alkaline electrolyte should also result in enhanced EOR activity.[29, 30]

The XPS results for the model surfaces pre- and post- electrochemical testing in both acid and alkaline environments were compared to evaluate the electrochemical stability, shown in Fig. 5.3. Comparisons of the ratios of Pt4f to Ta4f integrated areas for pre- and post- electrochemical

testing resulted in a decrease by approximately10% after the testing. Such a small decrease in the Pt/Ta ratios could likely be attributed to screening by the adsorption of electrolytes on the surface.[34] The relatively small changes in the Pt/Ta ratios suggested that the Pt overlayers were stable for EOR in both acid and alkaline electrolytes.

The Ta4f XPS spectra for 0.5 ML Pt/TaC and 1 ML Pt/TaC pre- and post- EOR testing are compared in Fig. 5.3C and 3D. The peaks at 22.62 eV and 24.53 eV corresponded to TaC, while the peaks at 25.21 eV and 27.12 eV correlated to oxidized Tas. The observation of surface oxide peaks in the fresh samples was expected due to the passivation process after TaC synthesis. Further oxidization occurred during the electrochemical testing in 0.5 ML Pt/TaC, likely due to the oxidation of uncovered TaC during EOR testing. In contrast, XPS results of the post- testing 1 ML Pt/TaC (Fig. 5.3D) showed that TaC was not further oxidized, indicating that deposited ML Pt prevented the TaC substrate from being oxidized. Overall, the results in Fig. 5.3 indicated that the ML Pt/TaC film was electrochemically stable for EOR under acid and alkaline conditions.

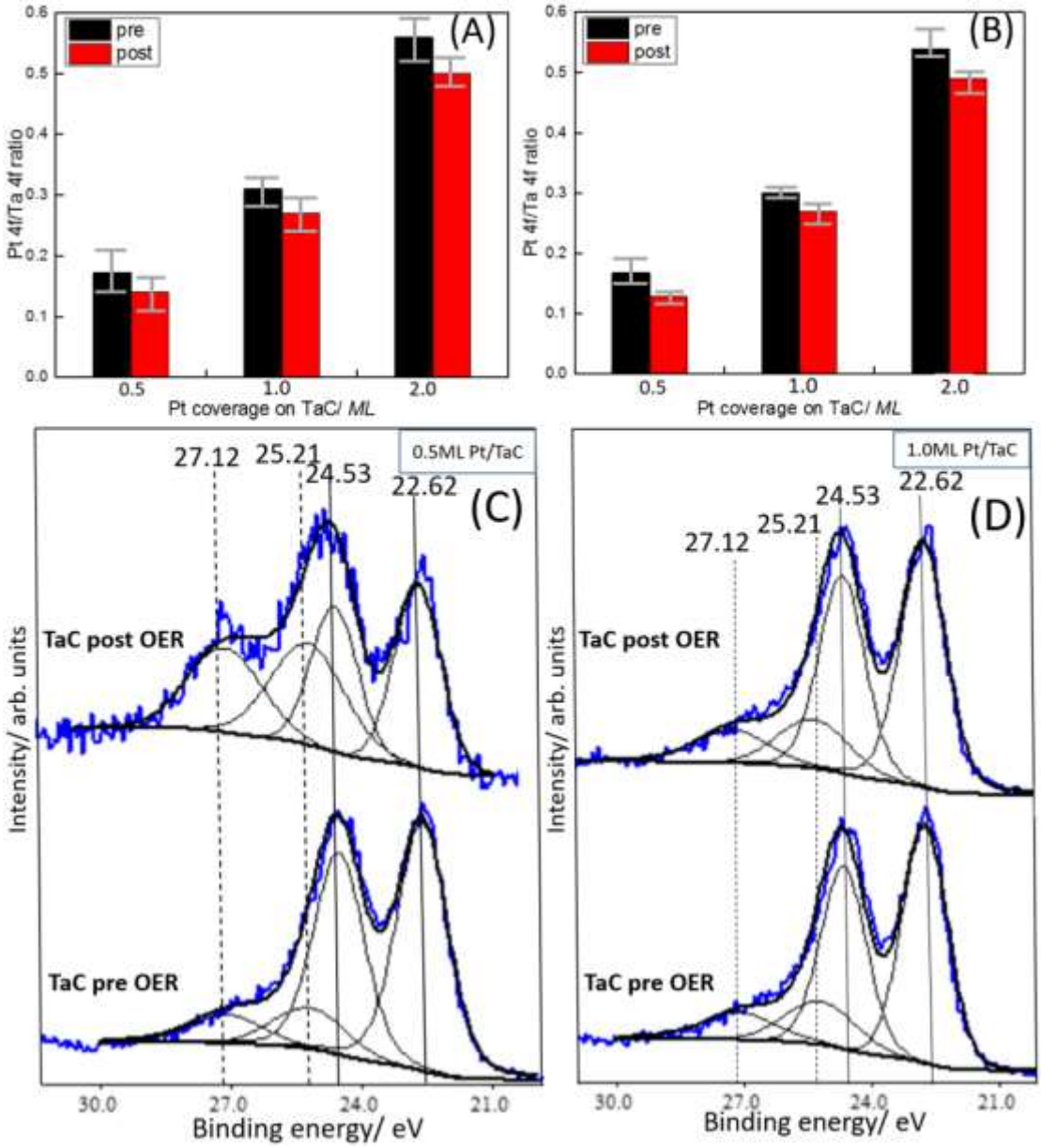

Figure 5.3 The ratio of Pt4f to Ta4f integrated areas from XPS measurements for pre- and post- EOR electrochemical testing for different ML Pt/TaC in acid (A) and base (B). XPS Ta4f spectra for pre- and post- EOR stability testing in base for 0.5 ML Pt/TaC (C) and 1 ML Pt/TaC (D). Electrochemical testing including 20 times CV scans followed by one-hour CA testing at 0.6V vs. RHE CV measurements.

5.3.2 Electrochemical studies of 1.5 wt% Pt/TaC powder catalysts

Because high surface area powder catalysts are more industrially relevant, 1.5 wt% Pt/TaC and the benchmark commercial 40 wt% Pt/C catalysts were studied by electrochemical LSV and

CA testing in both acid and alkaline, shown in Fig. 5.4. In order to account for the Pt dispersion effect on the EOR activity, the current density was normalized by the electrochemical surface areas (ECSAs) of both catalysts.

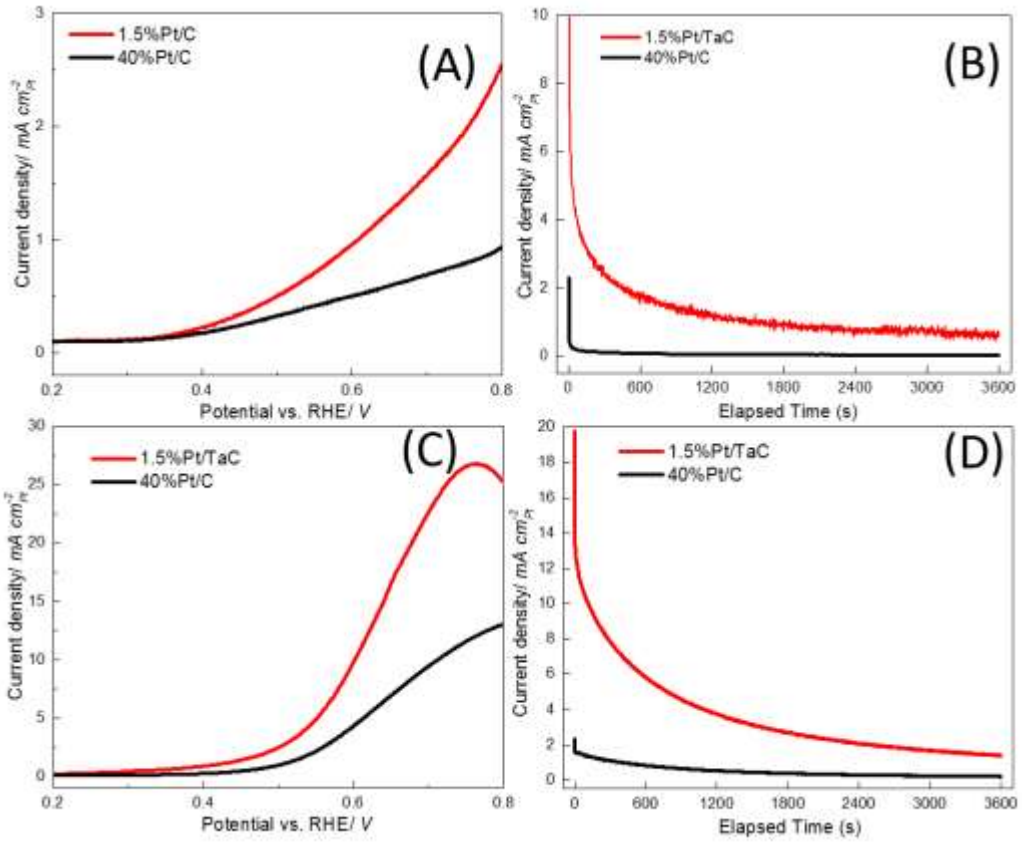

Figure 5.4 LSV scans (A) and one-hour CA testing at 0.6V vs. RHE (B) for 1.5 wt% Pt/TaC shown in red color and commercial 40 wt% Pt/C shown in black color in 0.5M H_2SO_4/1M EtOH; LSV scans (C) and one-hour CA testing at 0.6V vs. RHE (D) in 0.1M KOH/1M EtOH. The current density was normalized by their respective Pt ECSA of 1.5wt% Pt/TaC and commercial 40 wt% Pt/C.

As shown in Fig. 5.4A, enhanced LSV current density was achieved in 1.5 wt% Pt/TaC compared to that of 40 wt% Pt/C. Although the onset potential was similar for the two catalysts in acid, the LSV current density of 1.5 wt% Pt/TaC was significantly higher at 0.6 V. The enhanced acid EOR activity for 1.5 wt% Pt/TaC was further illustrated in the CA results (Fig. 5.4B). The same trends were observed in alkaline as in acid. The 1.5 wt% Pt/TaC catalyst increased current

density more rapidly than Pt in the LSV (Fig. 5.4C) and had higher current density at 0.6 V vs. RHE (Fig. 5.4D).

In order to uncover underlying reasons for the enhanced activity obtained by 1.5 wt% Pt/TaC compared to 40 wt% Pt/C, *in-situ* IRRAS-LSV experiments under the acid and alkaline EOR conditions were performed to identify the EOR intermediates and final products at different potentials. It is worth noting that the difference in onset potentials from electrochemical LSV testing (Fig. 5.4A and C) and *in-situ* IRRAS-LSV testing (Fig. 5.5 and Fig. 5.6) can be explained by the differences in transport conditions and difference scan rates. Although it is not suitable to directly compare the quantitative results obtained from the electrochemical LSV testing and the *in-situ* IRRAS-LSV experiment, the qualitative trend should remain valid.

For 40 wt% Pt/C in acid (Fig. 5.5A), vibrational modes associated with acetic acid (CH_3COOH) ν_S(C-O) at 1280 cm^{-1} and ν(C=O) at1715 cm^{-1} and acetaldehyde (CH_3CHO), ν_{as}(C-C-O) at 933 cm^{-1} and ω(C-H) at 1108 cm^{-1} were detected. At the same time, downward features, ν(C-O) at 1044 cm^{-1} for ethanol and (H-O-H) at 1635 cm^{-1} for water, indicated that these two molecules were consumed. The C_1 product, carbon dioxide (CO_2), ν_{as}(C-O-O) mode at 2341 cm^{-1}, was produced at 0.65 V vs. RHE. The peak assignments for 40 wt% Pt/C matched well with previous reports.[35] All peaks are summarized in the Table 5.1.

The C_1 and C_2 peaks both started at the potential of 0.65 V, indicating a parallel reaction pathway for C_1 and C_2. Regarding the C_1 reaction pathway, adsorbed carbon monoxide, ν(CO) at 2041 cm^{-1}, from the C-C bond scission was observed starting at 0.38 V vs. RHE and the peak area continued to increase along with an increase in applied potential until 0.65 V. This indicated that adsorbed CO remained on the Pt surface until a potential of 0.65 V was reached. Starting from 0.65 V, the CO_2 feature at 2341 cm^{-1}, the C_1 reaction pathway final product, was observed. The

peak area of the 2341 cm^{-1} mode then grew with increasing potentials while the peak area of the CO feature at 2041 cm^{-1} started decreasing. Regarding the C_2 reaction pathway, the C_2 oxidation products (CH_3CHO and CH_3COOH) were detected at a potential of 0.65 V.

On 1.5 wt% Pt/TaC, the IR peaks for acetaldehyde, acetic acid, and carbon dioxide were also observed. Other peaks associated with C_1 and C_2 species are listed in the Table 5.1. The EOR reaction pathways started at 0.47 V on 1.5 wt% Pt/TaC, which was approximately 0.2 V lower compared to that of 40 wt% Pt/C (Fig. 5.5A). The adsorbed CO peak at 2041 cm^{-1} was not detected throughout the entire potential range on 1.5 wt% Pt/TaC, indicating that the adsorbed CO can be easily oxidized on the 1.5 wt% Pt/TaC surface, unlike that on 40 wt% Pt/C [36,37]. This suggested that the kinetics for the C_1 reaction pathway on 1.5 wt% Pt/C should not be limited by adsorbed CO intermediates. Therefore, enhanced current density on the 1.5 wt% Pt/TaC (Fig. 5.4) was ascribed to faster kinetics due to higher tolerance to strongly adsorbed surface intermediates that poisoned the surface sites, as in the case of 40 wt% Pt/C.

The CO_2 (C_1) selectivity is defined as the ratio of distributed charge associated with CO_2 production to the total charge associated with the products from both C_1 and C_2 pathways. The C_1 selectivity for 1.5 wt% Pt/TaC and 40 wt% Pt/C were further quantified because it could be used to evaluate the catalytic efficiency for EOR. A higher C_1 selectivity represents a more efficient EOR catalyst. Among all products, the C_1 product (CO_2) is produced from the total ethanol oxidation as the most efficient reaction pathway and 12 moles electrons (highest faraday efficiency) are produced. In comparison, C_2 products are from partial ethanol oxidation, with one mole ethanol oxidation only resulting in only 2 (CH_3CHO as the final product) or 4 (CH_3COOH as the final product) moles electrons. The integrated IR peak areas for acetaldehyde (933 cm^{-1}), acetic acid (1280 cm^{-1}), and CO_2 (2341 cm^{-1}) can be used to illustrate the qualitative trend for the C_1 species

selectivity, as described in literature.[38,39] Based on the CO_2 selectivity for EOR on 40% Pt/C and 1.5% Pt/TaC in acid, shown in Fig. 5.5C, CO_2 was not produced on 40% Pt/C below 0.6 V and the peak area ratio was only 2% above 0.6 V [38]. In comparison, the CO_2 peak area ratio on 1.5% Pt/TaC was 7-9% at potentials starting at 0.47 V, indicating that this catalyst underwent a more efficient reaction pathway through the C-C bond breakage. The higher C_1 selectivity on the Pt/TaC surface could be attributed to the lower activation energy barrier for the C-C breakage compared to the Pt surface, supported by lower activated energy barrier calculated by DFT calculation (Fig. 5.8).

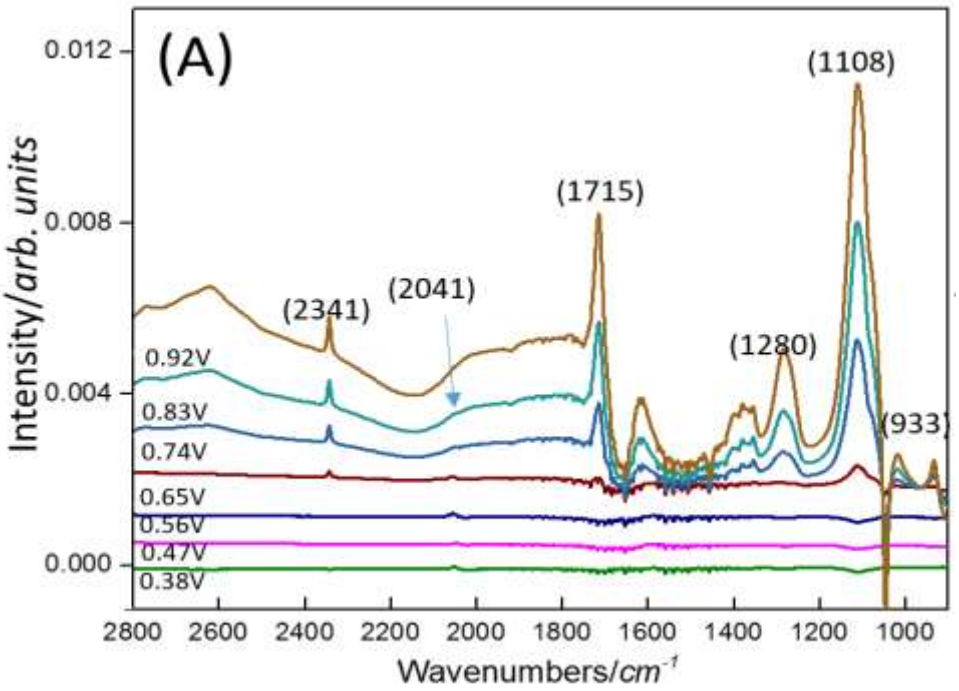

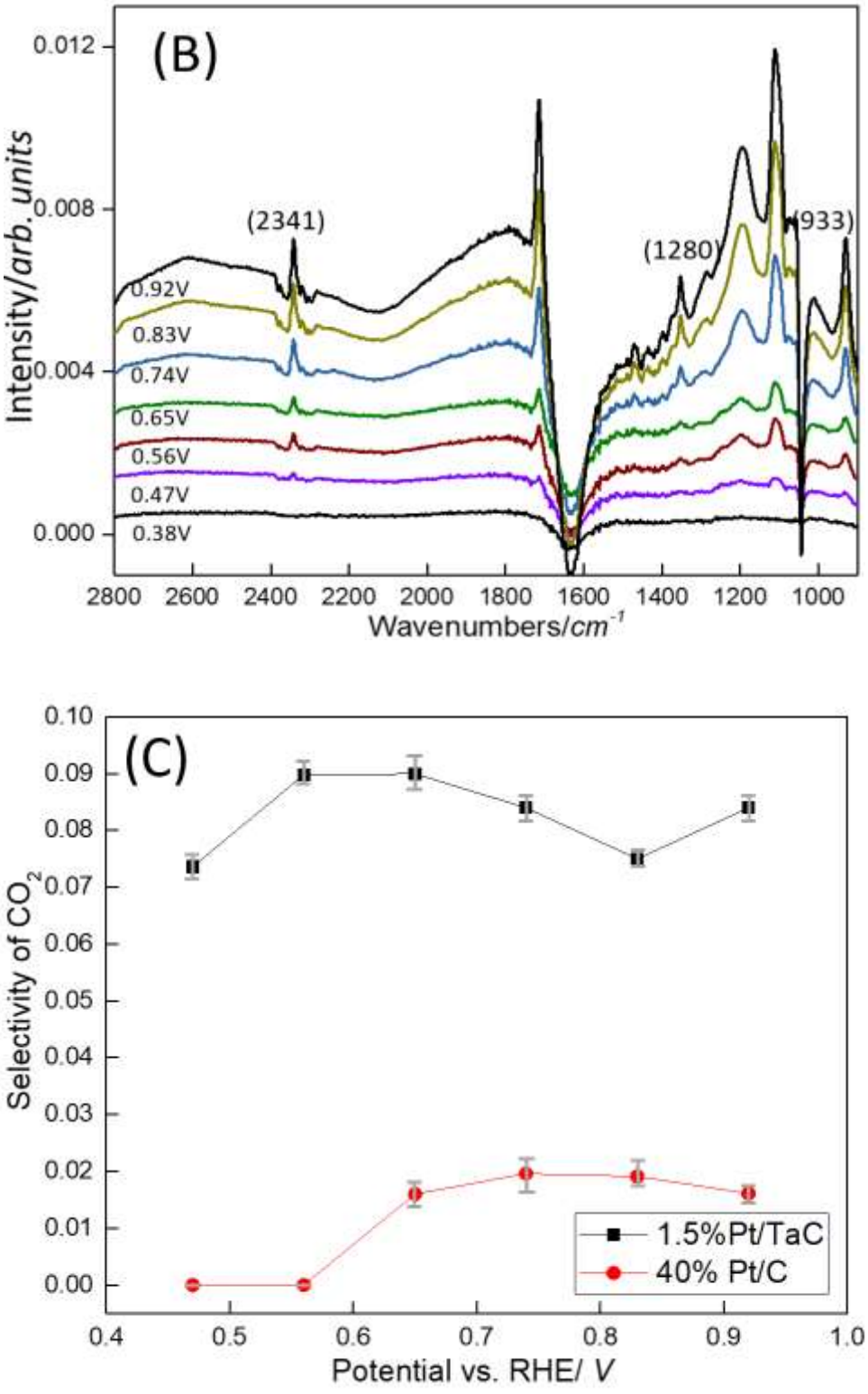

Figure 5.5 *In-situ* IRRAS spectra of 40wt% Pt/C (A) and of 1.5wt% Pt/TaC (B) in acid EOR LSV testing; the selectivity of CO_2 along with applied potential (C) on 1.5 wt% Pt/TaC indicated in black squares and commercial 40 wt% Pt/C indicated in red circles.

In-situ IRRAS-LSV experiments were also performed on 40 wt% Pt/C (Fig. 5.6A) and 1.5 wt% Pt/TaC (Fig. 5.6B) in alkaline electrolyte. On the 40% Pt/C catalyst, acetate (CH_3COO^-) in alkaline, instead of acetic acid in acid, was identified as the main C_2 product, as indicated by peaks of ν_{as}(O-C-O) at 1550 cm^{-1} and ν_S(O-C-O) at 1415 cm^{-1}. The other C_2 vibrational peaks, ν_{as}(O-C-O) at 933 cm^{-1} and ω(C-H) at 1108 cm^{-1}, were attributed to CH_3CHO. C_2 product peaks at 1550 cm^{-1} and 933 cm^{-1}peaks on 40 wt% Pt/C were detected starting at the potential of 0.57 V while the onset potential was lower starting at 0.37 V for 1.5 wt% Pt/TaC. All Peaks are summarized in the Table 5.1.

Regarding the C_1 reaction pathway, unlike the case in acid electrolyte, the product selectivity could not be compared in alkaline electrolyte due to the overlapping IR peaks of C_1 and C_2 products. The carbonate anion signal at 1510 cm^{-1}[140–45] and the bicarbonate signal at 1350 cm^{-1}[141,43,46,47], resulting from C_1 species in alkaline, were convoluted with the acetate bands of ν_S(O-C-O) at 1415cm^{-1} and ρ(CH_3) 1348 cm^{-1}. The 2341 cm^{-1} CO_2 feature was supposed to be the C_1 EOR product in acid environment, but it was detected starting at the potential of 0.97V vs. RHE in alkaline on both catalysts (Fig. 5.6). This might be attributed to the neutralization of the electrolyte thin layer between the IR window and the working electrode.[48]

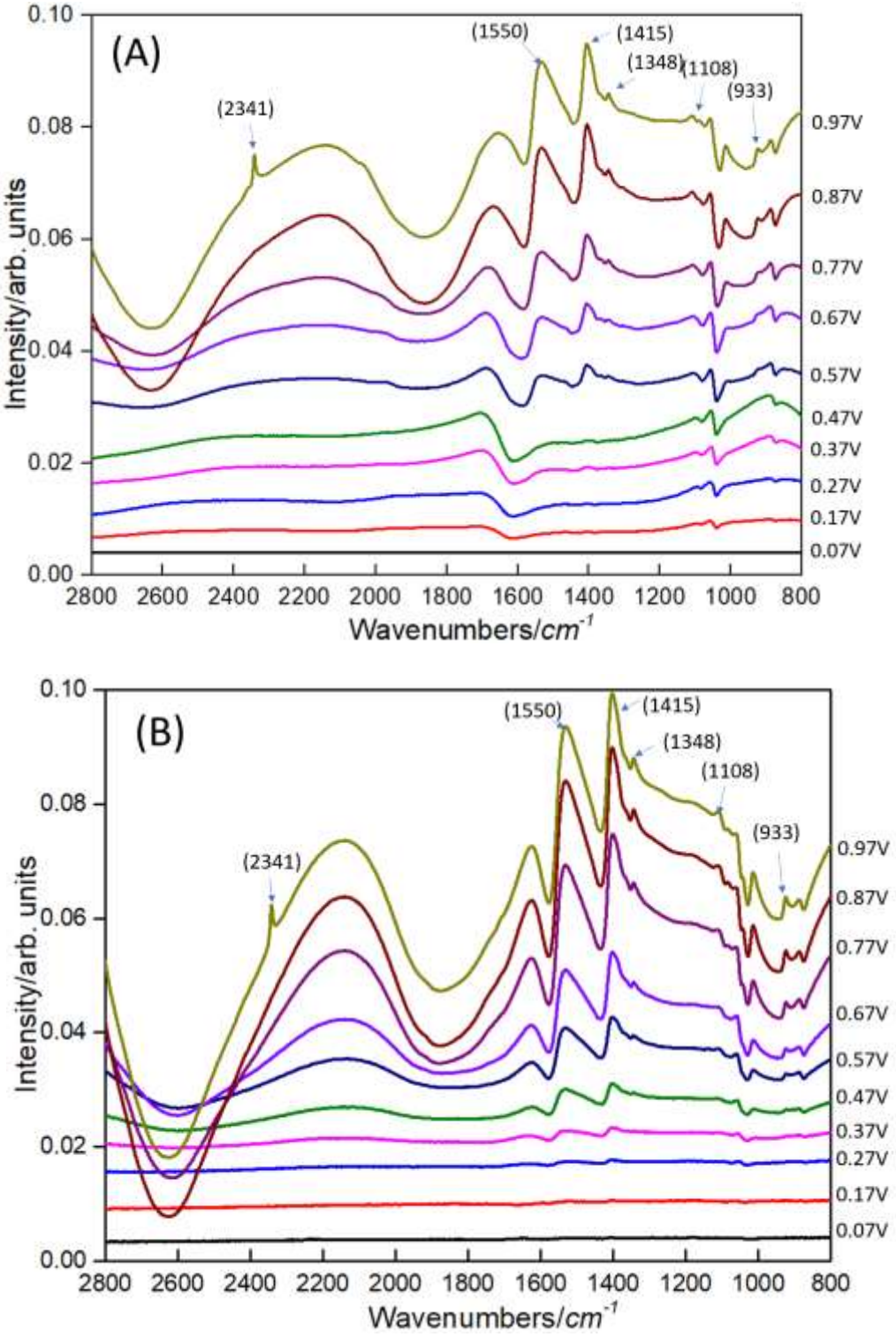

Figure 5.6 *In-situ* IRRAS spectra of 40 wt% Pt/C(A) and of 1.5 wt% Pt/TaC (B) in alkaline EOR LSV testing.

Table 5.1 Peak assignments for the IR spectra

Wave number(cm-1)	**mode**	**Reference**
2750	OH ions in the solution	[42–44,48]
2341	CO_2 asymmetric stretching in solution	[12,43,47]
2041	adsorbed CO linearly bonded	[12]
1870	Related to adsorbed O-H	[42–44,48]
1715	C=O stretching in CH_3CHO and CH_3COOH in solution	[12,21,49]
~1635	H-O-H bending of H_2O	[21]
~1630	C=O stretching of adsorbed acetaldehyde and acetyl	[49]
1550	O-C-O asymmetric stretching of acetate in solution	[40]
1415	O-C-O symmetric stretching in acetate	[40,49]
1383	CH in-plane bending mode of adsorbed acetate/ acetate in solution	[40,49,44]
1355	CH_3 symmetric deformation in CH_3CHO	[12,21]
1348	Weak peak associated acetate in solution	[40,48]
1280	C-O stretching in CH_3COOH	[12,48,49]
1108	C-H wagging in CH_3CHO	[49]
1044	C-O stretching of CH_3CH_2OH	[50]

933	C-C-O asymmetric stretching of CH_3CHO	[49,51]

5.3.3 DFT calculations

In order to further understand the electrochemical and *in-situ* IRRAS results, DFT calculations were performed to compare the binding energies of the intermediates from C-C and C-H bond scissions in ethanol on Pt(111) and Pt/TaC(111) surfaces. Based on the EOR mechanism proposed in the previous reports[5253] the possible surface intermediates included CH_3CH_2OH, CH_3CH_2O (ethoxy), CH_3CHOH, CH_2CH_2OH, CH_3, CH_2OH, CH_3CHO, CH_3CO, CH_2CO and CO. The high symmetry adsorption sites of both surfaces were considered: atop, bridge, fcc, and hcp sites. The most stable adsorption configurations of these possible intermediates on Pt(111) and Pt/TaC(111) surfaces are shown in Fig. 5.7. The binding energies and key geometric parameters of all the species at the most stable positions are listed in Table 5.2.

Table 5.2 DFT calculations of binding energies (eV) of potential EOR intermediates on Pt(111) and Pt/TaC(111) surfaces.

Surfaces	Species	Configurations	Binding energies/eV
Pt(111)	CH_3CH_2OH	atop, O-bound	-0.31
	CH_3CH_2O	atop, O-bound	-1.82
	CH_3CHOH	atop, C_α-bound	-2.28
	CH_2CH_2OH	atop, C_β –bound	-2.45
	CH_3	atop, C-bound	-2.38
	CH_2OH	atop, C-bound	-2.37

	CH_3CHO	bridge, C-bound and O-bound	-0.71
	CH_3CO	atop, C-bound	-2.37
	CH_2CO	bridge, C-bound	-1.48
	CO	fcc, C-bound	-2.02
	H	fcc, H-bound	-0.46
Pt/TaC(111)	CH_3CH_2OH	atop, O-bound	-0.42
	CH_3CH_2O	atop, O-bound	-1.92
	CH_3CHOH	atop, C_α-bound	-1.42
	CH_2CH_2OH	atop, C_β –bound	-1.92
	CH_3	atop, C-bound	-1.66
	CH_2OH	atop, C-bound	-1.50
	CH_3CHO	atop, O-bound	-0.48
	CH_3CO	atop, C-bound	-1.90
	CH_2CO	bridge, C-bound	-0.51
	CO	hcp, C-bound	-1.35
	H	bridge, H-bound	-0.28

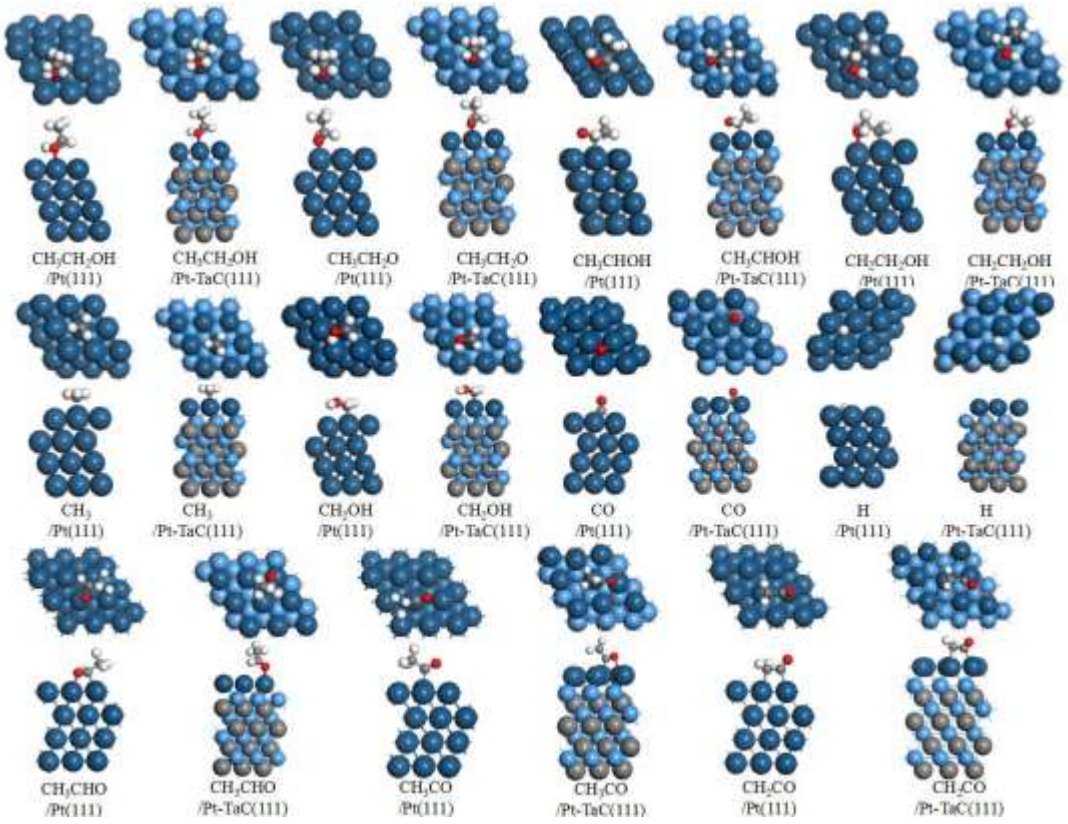

Figure 5.7 Top and side views of the most stable configurations of the possible intermediates on Pt(111) and Pt/TaC(111) surfaces.

As shown in Fig. 5.7, ethanol preferred to bind at the atop site on both surfaces. The ethanol interaction with Pt/TaC(111) was slightly stronger than Pt(111) with the binding energy of -0.42 eV and -0.31 eV, respectively. The binding energy of ethoxy was also slightly higher on Pt/TaC (-1.92 eV) than that on Pt (-1.82 eV). Interestingly, for other intermediates (CH_3CHOH, CH_2CH_2OH, CH_3, CH_2OH, CH_3CHO, CH_3CO, CH_2CO and CO), the binding energies on the Pt/TaC(111) surface were smaller than those on the Pt(111) surface, suggesting that Pt/TaC(111) should have a higher tolerance to the site-blocking by EOR intermediates, agreeing well with the *in-situ* IRRAS-LSV results. For example, the CO binding energies were calculated to be -2.02 and -1.35 eV on the Pt(111) and Pt/TaC(111) surfaces, respectively. The higher CO binding energy on the Pt(111) surface indicated that Pt sites are more likely to be blocked by CO on the Pt(111) surface[36,37], which required higher potential to oxidize the adsorbed CO. On the other hand, the lower CO

binding energy on Pt/TaC suggested that the CO poisoning effect was alleviated on the Pt/TaC surface, resulting in more facile CO oxidation on Pt/TaC, in agreement with the observation in *in-situ* IRRAS-LSV (Fig. 5.5).

Furthermore, activation energies of the C_α-H and C-C bond scission were calculated to further understand the reaction pathways for ethanol decomposition on Pt(111) and Pt/TaC(111) surfaces. The activation energies and reaction energies for elementary reactions are shown in Table 5.3. The potential energy diagrams for the initial decomposition of ethanol on Pt(111) and Pt/TaC(111) surfaces are shown in Fig. 5.8. On both surfaces the activation energies for C-H bond cleavages were lower than that for C-C bond cleavages, suggesting that the primary reaction pathways for both surfaces should follow the C-H bond scission. This explains the low selectivity towards C_1 products as observed in the *in-situ* IRRAS results. In addition, Pt/TaC(111) had lower activation energies for both C-H and C-C bond scissions compared to Pt(111). For example, the formation of CO_2 from the C-C bond scission should be more facile on the Pt/TaC(111) surface with a smaller barrier of 2.31 eV as compared to 2.64 eV on Pt(111), which supported the higher EOR activity and CO_2 selectivity obtained from the electrochemical measurement and *in-situ* IRRAS-LSV results.

Table 5.3 Activation energies (E_a) and reaction energies ($\triangle E$) for the elementary steps of ethanol decomposition on Pt(111) and Pt/TaC(111) surfaces.

Reactions	Pt(111)		Pt-TaC(111)	
	E_a (eV)	$\triangle E$	E_a (eV)	$\triangle E$
$CH_3CH_2OH \rightarrow CH_3CHOH + H$	0.78	0.19	0.62	0.13
$CH_3CH_2OH \rightarrow CH_3 + CH_2OH$	2.64	0.31	2.31	1.31

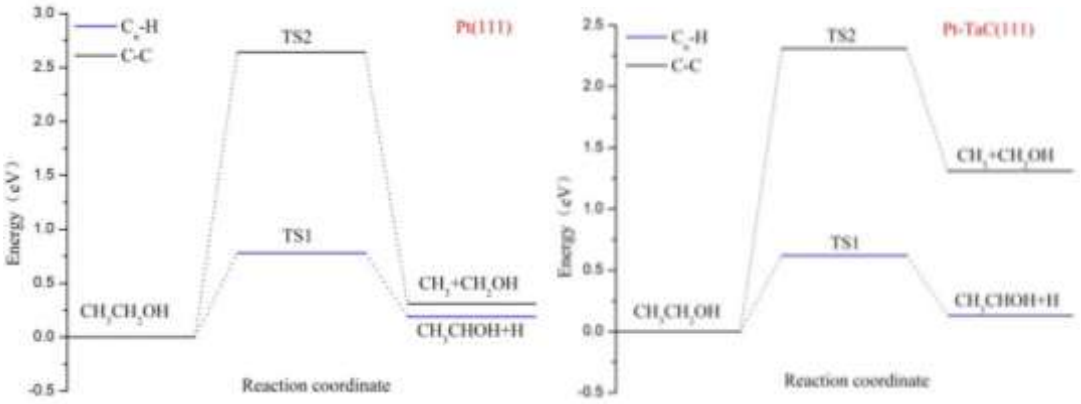

Figure 5.8 The potential energy diagrams for C_α-H and C-C bond scission of ethanol on Pt(111) and Pt/TaC(111) surfaces.

5.4 Conclusions

In summary, ethanol oxidation reaction has been investigated in acid and alkaline electrolytes by combining the electrochemical, XPS and *in-situ* IRRAS measurements with DFT calculations. Compared with the Pt foil and 40wt% Pt/C, the corresponding Pt/TaC thin film and powder catalyst show enhanced EOR activity and stability in both acid and alkaline electrolytes. *In-situ* IRRAS-LSV results suggest a higher CO tolerance and higher CO_2 selectivity on the Pt/TaC surface. DFT calculations reveal that the binding energy of CO is considerably weaker on the Pt/TaC(111) surface, consistent with a higher CO tolerance for Pt/TaC. The binding energies of other possible EOR intermediates are also lower on Pt/TaC(111) than on Pt(111). These factors could explain the enhanced EOR activity observed on the 1.5wt% Pt/TaC powder catalyst. The combined experimental and theoretical results indicate that Pt-modified TaC should be promising and stable electrocatalysts for EOR in both acid and alkaline electrolytes. These results also provide useful guidelines for the design of carbide-based electrocatalysts for EOR.

References

(1) Akhairi, M. A. F.; Kamarudin, S. K. *Int. J. Hydrogen Energy* **2016**, *41* (7), 4214–4228.

(2) Beyhan, S.; Coutanceau, C.; Léger, J.-M.; Napporn, T. W.; Kadırgan, F. *Int. J. Hydrogen Energy* **2013**, *38*, 6830–6841.

(3) Wang, Y.; Zou, S.; Cai, W.-B. *Catalysts* **2015**, *5* (3), 1507–1534.

(4) Elezovic, N. R.; Radmilovic, V. R.; Krstajic, N. V. *RSC Adv.* **2016**, *6* (8), 6788–6801.

(5) Rees, N. V.; Compton, R. G. *Energy Environ. Sci.* **2011**, *4* (4), 1255.

(6) Barthelemy, H.; Weber, M.; Barbier, F. *Int. J. Hydrogen Energy* **2016**.

(7) Mahoney, E. G.; Sheng, W.; Cheng, M.; Lee, K. X.; Yan, Y.; Chen, J. G. *J. Power Sources* **2016**, *305*, 89–96.

(8) Moraes, L. P. R.; Matos, B. R.; Radtke, C.; Santiago, E. I.; Fonseca, F. C.; Amico, S. C.; Malfatti, C. F. *Int. J. Hydrogen Energy* **2016**, *41* (15), 6457–6468.

(9) Rousseau, S.; Coutanceau, C.; Lamy, C.; Léger, J.-M. *J. Power Sources* **2006**, *158* (1), 18–24.

(10) Xuan, J.; Leung, M. K. H.; Leung, D. Y. C.; Ni, M. *Renew. Sustain. Energy Rev.* **2009**, *13* (6), 1301–1313.

(11) Mellinger, Z. J.; Weigert, E. C.; Stottlemyer, A. L.; Chen, J. G. *Electrochem. Solid-State Lett.* **2008**, *11* (5), B63.

(12) Colmati, F.; Tremiliosi-Filho, G.; Gonzalez, E. R.; Berná, A.; Herrero, E.; Feliu, J. M. *Faraday Discuss.* **2008**, *140*, 379-97-37.

(13) Tackett, B. M.; Sheng, W.; Chen, J. G. *Joule* **2017**, 1–11.

(14) Weigert, E. C.; Stottlemyer, A. L.; Zellner, M. B.; Chen, J. G. *J. Phys. Chem. C* **2007**, *111* (40), 14617–14620.

(15) Kelly, T. G.; Chen, J. G. *Chem. Soc. Rev.* **2012**, *41* (24), 8021.

(16) Stottlemyer, A. L.; Liu, P.; Chen, J. G. *J. Chem. Phys.* **2010**, *133* (10), 104702.

(17) Kelly, T. G.; Stottlemyer, A. L.; Yang, X.; Chen, J. G. *J. Electrochem. Soc.* **2014**, *161* (8), E3165–E3170.

(18) Esposito, D. V.; Chen, J. G. *Energy Environ. Sci.* **2011**, *4* (10), 3900.

(19) Esposito, D. V.; Hunt, S. T.; Kimmel, Y. C.; Chen, J. G. *J. Am. Chem. Soc.* **2012**, *134* (6), 3025–3033.

(20) Kimmel, Y. C.; Xu, X.; Yu, W.; Yang, X.; Chen, J. G. *ACS Catal.* **2014**, *4* (5), 1558–1562.

(21) Lai, S. C. S.; Kleijn, S. E. F.; Öztürk, F. T. Z.; van Rees Vellinga, V. C.; Koning, J.; Rodriguez, P.; Koper, M. T. M. *Catal. Today* **2010**, *154* (1), 92–104.

(22) Lai, S. C. S.; Koper, M. T. M. *Phys. Chem. Chem. Phys.* **2009**, *11* (44), 10446–10456.

(23) Hwu, H. H.; Chen, J. G. *Chem. Rev.* **2005**, *105* (1), 185–212.

(24) Shubina, T. .; Koper, M. T. . *Electrochim. Acta* **2002**, *47* (22–23), 3621–3628.

(25) Kim, S. K.; Zhang, Y.-J.; Bergstrom, H.; Michalsky, R.; Peterson, A. *ACS Catal.* **2016**, *6* (3), 2003–2013.

(26) Kimmel, Y. C.; Esposito, D. V.; Birkmire, R. W.; Chen, J. G. *Int. J. Hydrogen Energy* **2012**, *37* (4), 3019–3024.

(27) Kresse, G.; Hafner, J. *Phys. Rev. B* **1993**, *47* (1), 558–561.

(28) Kresse, G.; Joubert, D. *Phys. Rev. B* **1999**, *59* (3), 1758–1775.

(29) Perdew, J. P.; Wang, Y. *Phys. Rev. B* **1992**, *46* (20), 12947–12954.

(30) Ma, L.; Chu, D.; Chen, R. *Int. J. Hydrogen Energy* **2012**, *37* (15), 11185–11194.

(31) Busó-Rogero, C.; Solla-Gullón, J.; Vidal-Iglesias, F. J.; Herrero, E.; Feliu, J. M. .

(32) Jiang, L.; Hsu, A.; Chu, D.; Chen, R. *Int. J. Hydrogen Energy* **2010**, *35* (1), 365–372.

(33) St. John, S.; Angelopoulos, A. P. *Electrochim. Acta* **2013**, *112*, 258–268.

(34) Kelly, T. G.; Hunt, S. T.; Esposito, D. V.; Chen, J. G. *Int. J. Hydrogen Energy* **2013**, *38* (14), 5638–5644.

(35) Iwasita, T.; Pastor, E. *Ekctrochimica Acta* **1994**, *39* (4), 531–537.

(36) Camara, G. A.; de Lima, R. B.; Iwasita, T. *J. Electroanal. Chem.* **2005**, *585* (1), 128–131.

(37) Holade, Y.; Sahin, N.; Servat, K.; Napporn, T.; Kokoh, K. *Catalysts* **2015**, *5* (1), 310–348.

(38) Camara, G. A.; Iwasita, T. *J. Electroanal. Chem.* **2005**, *578* (2), 315–321.

(39) Li, M.; Cullen, D. A.; Sasaki, K.; Marinkovic, N. S.; More, K.; Adzic, R. R. *J. Am. Chem. Soc.* **2013**, *135* (1), 132–141.

(40) Zhou, Z.-Y.; Wang, Q.; Lin, J.-L.; Tian, N.; Sun, S.-G. *Electrochim. Acta* **2010**, *55* (27), 7995–7999.

(41) Chen, Q.-S.; Sun, S.-G.; Zhou, Z.-Y.; Chen, Y.-X.; Deng, S.-B. *Phys. Chem. Chem. Phys.* **2008**, *10* (25), 3645.

(42) Christensen, P. A. P. a.; Hamnett, A. *J. Electroanal. Chem.* **1989**, *260* (2), 347–359.

(43) Christensen, P. A.; Hamnett, A.; Linares-Moya, D. *Phys. Chem. Chem. Phys. Phys. Chem. Chem. Phys* **2011**, *13* (13), 11739–11747.

(44) Christensen, P. A.; Linares-Moya, D. *J. Phys. Chem. C* **2010**, *114* (2), 1094–1101.

(45) Chbihi, M. E. M.; Takky, D.; Hahn, F.; Huser, H.; Léger, J. .; Lamy, C. *J. Electroanal. Chem.* **1999**, *463* (1), 63–71.

(46) Lbpez-Atalaya, M.; Morallh, E.; Casesb, F.; Vgzquez, J. L.; Perez, J. M. *J. Power Sources* **1994**, *52*, 109–117.

(47) Arihara, K.; Kitamura, F.; Ohsaka, T.; Tokuda, K. *J. Electroanal. Chem.* **2001**, *510* (1), 128–135.

(48) Christensen, P. A.; Jones, S. W. M.; Hamnett, A. *J. Phys. Chem. C* **2012**, *116* (46), 24681–24689.

(49) Li, M.; Cullen, D. A.; Sasaki, K.; Marinkovic, N. S.; More, K.; Adzic, R. R. **2012**.

(50) Plyler, E. K. *J. Res. Natl. Bur. StanJards* **1952**, *48* (4).

(51) Gao, P.; Chang, S.-C.; Zhou, Z.; J. Weaver, M. *J. Electroanal. Chem. Interfacial Electrochem.* **1989**, *272* (1), 161–178.

(52) Monyoncho, E. A.; Steinmann, S. N.; Michel, C.; Baranova, E. A.; Woo, T. K.; Sautet, P. *ACS Catal.* **2016**, *6* (8), 4894–4906.

(53) Wang, H. F.; Liu, Z. P. *J. Am. Chem. Soc.* **2008**, *130* (33), 10996–11004.

6. PALLADIUM-MODIFIED TUNGSTEN CARIBDE FOR ETHANOL ELECTROOXIDATION: FROM SURFACE SCIENCE STUDIES TO ELETROCHEMIOCAL EVALUATION

6.1 Introduction

To meet the demands for alternative energy devices researchers have investigated power sources with potentially higher efficiency, higher power density and lower operating temperatures for portable applications. Compared to hydrogen and methanol fuel cells, ethanol contains higher energy densities than hydrogen[1,2] and methanol[3] with non-toxicity[4] while also fitting well into the current energy infrastructure[4]. Platinum (Pt) has been extensively studied for direct ethanol fuel cells (DEFC) as one of the most promising monometallic anode catalysts for the ethanol oxidation reaction (EOR).[5–7] However, Pt has limitations for large-scale applications due to its low natural abundance and high cost.[7,8] Furthermore, given that Pt suffers from poisoning by the EOR intermediates (e.g., CO and carbonyl-containing species)[6,9–11], the ethanol oxidation requires an applied potential higher than 0.65V vs. reversible hydrogen electrode (RHE).[12] This large overpotential reduces the net output voltage, which ultimately reduces the DEFC efficiency.

Palladium (Pd) [4,13–15] catalysts have been investigated as an alternative for Pt given that Pd has a similar electronic structure as Pt but with typically one-fiftieth the cost.[4,14,16] In terms of supported Pd catalysts, Pd-modified tungsten carbides (WC) has shown an enhanced tolerance than Pd/C to poisonous intermediates [17] for the methanol oxidation reaction (MOR)[18]. Regarding EOR, Pd-based catalysts have also been explored to enhance the EOR activity through a bifunctional mechanism by modifying Pd with other substrates and promotors[4,7,19–21].

In this manuscript, the first part focuses on the fundamental understanding of Pd-modified WC for ethanol activation using DFT calculations and surface science studies. By calculating and comparing the binding energies of possible intermediates through ethanol decomposition on Pd(111) and Pd/WC(0001) surfaces, DFT results show that, the Pd/WC(0001) surface is less likely to be poisoned by the intermediates from ethanol decompositions. Surface science results demonstrate that the Pd/WC surface increases ethanol activity toward the C-H and C-C bond breakage while unmodified WC primarily undergoes the undesired C-O bond scission. Furthermore, detected intermediates from the ethanol decomposition desorb at lower temperatures from Pd/WC than from the Pd surface. The promising results on model surfaces are then verified on powder catalysts containing five weight percent Pd-modified WC on Vulcan carbon (5 wt% Pd/WC/C), synthesized using both the one-pot (op) and the conventional incipient wetness impregnation (iwi) methods. The 5 wt% Pd-WC/C-op catalyst shows higher EOR activity and stability than the benchmark 40 wt% Pd/C and 5 wt% Pd/WC/C-iwi catalysts in alkaline electrolyte. I*n-situ* infrared reflection absorption spectroscopy (IRRAS) measurements further confirm the enhanced activity of the 5 wt% Pd-WC/C-op catalyst.

6.2 Computational and experimental methods

6.2.1 DFT calculations

Density functional theory (DFT) calculations were carried out using the Vienna *ab initio* simulation package (VASP)[22]. The electronic-ion interaction was modeled by the projector augmented wave (PAW) method[23]. The Perdew-Wang-91 (PW91) functional[24], with the generalized gradient approximation (GGA), was employed to deal with electronic exchange and correlation. The kinetic wave cutoff energy was set to 400 eV to describe the electronic wave functions. The Brillouin-zone integration was sampled using a 3×3×1 Monkhorst-Pack k-points grid with a Gaussian smearing of 0.1eV. Geometries were optimized until the energy converged to 1.0×10^{-5} eV/atom and the force to 0.01 eV/Å.

The Pd(111) surface was modeled using a four-layer, 3×3, super-cell. Similarly, a Pd/WC(0001) surface was modeled using a nine-layer, 3×3, super-cell, where a Pd monolayer was deposited on the WC(0001) surface. A vacuum layer of 15 Å was added perpendicular to the slab to avoid artificial interactions between the slab and its periodic images. The upper two layers for the Pd(111) surface and the upper five layers for the Pd/WC(0001) surface were allowed to relax while other layers were held fixed.

The binding energies (BE) for all intermediates on metal surfaces were calculated as follows:

$$BE = E_{adsorbate+surface} - E_{adsorbate} - E_{surface}$$

where $E_{adsorbate + surface}$ is the total energy of the adsorbate together with the surface, $E_{adsorbate}$ is the energy of the free adsorbate in the gaseous phase, and $E_{surface}$ is the energy of the clean surface.

6.2.2 Surface science measurements

Polycrystalline WC and Pd-modified WC surfaces were synthesized under ultra-high vacuum (UHV) conditions. Details regarding the synthesis have been described in a previous publication[25]. Temperature programmed desorption (TPD) measurements were performed on WC and Pd/WC surfaces with the initial dose of 2L ethanol at 100K. TPD quantification was achieved followed the same procedure described previously.[26] High-resolution electron energy loss spectroscopy (HREELS), with an incident beam energy of 6 eV, was implemented to identify the surface adsorbates and intermediates in a separate UHV chamber (base pressure $2*10^{-10}$ Torr). Details regarding apparatus parameter settings and data processing can be found in literature[25].

6.2.3 Powder catalyst synthesis and characterization

The 5 wt% Pd-WC/C-op catalyst with the 1:1 Pd:W molar ratio were synthesized using an "one-pot" wet impregnation method. Although the main principles of the synthesis were based on reported methods[10], detailed synthesis procedures and the carburization temperatures differed. Specifically, the synthesis started with mixing the target amount of Pd precursor ($PdCl_2$, Sigma-Aldrich, 99.999%) with the tungsten carbide precursor of ammonium paratungstate, $(NH_4)_{10}H_2(W_2O_7)_6$ (Sigma -Aldrich, 99.99%) in 250 ml deionized water purified to a resistivity above 17MΩ by a Barnstead-NAN-Opure system. The solution was agitated using a magnetic stir for 5 hrs. Then, 0.1 gram Vulcan XC 72 carbon was slowly added to the agitated solution. Due to the low density of Vulcan carbon, Vulcan carbon tend to suspend on the top solution, so the Vulcan carbon had to be poured intermittently along with a simultaneous sonication in an ice bath. After sonication, the solution was transferred to the magnetic stirrer and agitated for 4 hours, followed by heating the solution to 358 K to evaporate the solvent in air. The dried sample was loaded into

a ceramic container and then transferred into a horizontal quartz tube furnace. The temperature programmed synthesis was applied to the sample in a hydrogen flow of 100 mL min^{-1}. Initially, the temperature was ramped to 373 K in 30 minutes and held for 2 hours. The temperature was then raised to 673 K for 2.5 hours followed by being continuously ramped to 1223 K for 7 hrs. The sample was held at 1223 K for 1 hour to undergo thermally induced formation of tungsten carbide in a hydrogen environment. The temperature was decreased to 1123 K and held for 30 minutes to remove the surface carbon.[27] After cooling the sample down to room temperature, the sample was passivated in 1%O_2/99%N_2 for one hour.

The 5 wt% Pd/WC/C-iwi catalyst was prepared by incipient wetness impregnation (iwi)[28] of Pd precursor ($PdCl_2$, Sigma-Aldrich, 99.999%) on a target amount of unmodified WC/C. The unmodified WC/C catalyst was synthesized following the same procedure as synthesizing the 5 wt% Pd-WC/C-op catalyst with the exception that Pd precursor was not incorporated. Once the Pd precursor was later impregnated on the WC/C using the iwi method, the sample was dried at 373 K for two hours in a hydrogen flow environment of 100 mL min^{-1}. The temperature was then ramped to 623 K and held for one hour. The passivation process took place at room temperature in 1%O_2/ 99%N_2 for one hour. X-ray diffraction (XRD) patterns confirmed that tungsten precursors were fully carburized in both samples and the tungsten carbides were a mixture of WC and W_2C phases.

The catalyst ink was made by mixing the desired amount of powder catalysts with isopropanol, DI water and Nafion 117 solution (Sigma–Aldrich). In preparation of each sample, the electrode ink was sonicated in an ice bath for one hour. The ink, containing a 0.1mg catalyst (5 µg Pd loading), was dropped onto a glassy carbon electrode (GCE) with a geometric surface area of 0.196 cm^2. The electrode was air-dried overnight before electrochemical measurements.

The electrochemical surface area (ECSA) of each catalyst was determined using cyclic voltammetry (CV) in an Ar-saturated 0.5M H_2SO_4 electrolyte. The CV scan range was from 0.05V to 0.95V vs. RHE in 0.5M H_2SO_4 with a scan rate of 0.05 V s^{-1} and the cathodic peak from a Pd-O region of 0.9V to 0.5V vs. RHE was used for estimating the ECSA of Pd for each sample. Instead of the Pd-H region, the Pd-O region had been reported to be more appropriate to determine Pd ECSAs in carbon-supported Pd and Pd-based catalysts.[29,30] The monolayer charge of adsorbed oxygen is approximately 420 μC cm^{-2}, which is two times larger than the charge of the hydrogen monolayer (Q_H= 210 μC cm^{-2})[3132].

6.2.4 Electrochemical measurements and stability test

Electrochemical measurements were performed at room temperature in an alkaline (0.1MKOH) electrolyte. Experiments were carried out with and without 1M ethanol (EtOH) in a three-electrode single-cell set-up with graphite (Sigma-Aldrich, 99.995 % trace metal basis) as the counter electrode and a reversible hydrogen electrode (RHE) as the reference electrode. Princeton Applied Research Versa STAT 4 was used to conduct linear scanning voltammetry (LSV), cyclic voltammetry (CV) and chronoamperometry (CA) measurements. The working electrode was first cycled and cleaned in the Ar-purged electrolyte, without the presence of ethanol, between 0.05 and 0.9 V using a scan rate of 50 mV s^{-1}. Next, a target amount of anhydrous ethanol was added to achieve 1M ethanol in the alkaline electrolyte while the solution was continuously purged with Ar for 20 minutes. CV testing was conducted in a range between 0.05 to 0.9 V vs. RHE with a scan rate of 50 mV s^{-1} for 40 cycles followed by either LSV or CA testing at a potential of 0.6V vs. RHE for one hour. Working electrodes were rotated at 400 revolutions per minute (rpm). The cell resistance was measured by using electrochemical impedance spectroscopy (EIS). All reported

potentials were corrected by the cell resistance accordingly. The reported activities were normalized either by Pd mass loading or the Pd ECSA.

6.2.5 In-situ infrared reflection absorption spectroscopy (IRRAS)

In-situ IRRAS measurements were carried out with a Nicolet iS50 FT-IR spectrometer equipped with an A-type MCT detector cooled with liquid nitrogen. An unpolarized light beam was used with a resolution of $4cm^{-1}$ and averaged 288 scans for each spectrum. Intensity was defined as $I = -\log(R/R_o)$ where R and R_o are the reflected IR intensities from the sample and reference single beam spectrum, respectively. A ZnSe hemisphere was used as the IR window that the working electrodes were pressed against. The working electrodes were made from depositing the appropriate amount of 5 wt% Pd-WC/C-op ink and the benchmark 40 wt% Pd/C ink on glassy plates. Spectra were collected from 0.05 V to 1 V vs. RHE at a scan rate of 1 mV s^{-1} in alkaline electrolyte contained 0.1M KOH/1M ethanol.

6.3 Results and discussion

6.3.1 DFT calculations of ethanol and intermediates on Pd(111) and Pd/WC(111) surfaces

Binding energies for ethanol, ethoxy and possible intermediates (CH_3CHOH, CH_2CH_2OH, CH_3, CH_2OH, CH_3CHO, CH_3CO, CH_2CO and CO) from ethanol decomposition, are listed in Table 6.1. The optimized adsorption sites and the most stable adsorption configurations after the optimization are illustrated in Fig.6.1 and summarized in Table 6.1. Ethanol and ethoxy preferred to occupy the atop site via the oxygen atom on the Pd(111) and Pd/WC(0001) surfaces . All other intermediates in Table 6.1 were absorbed to the Pd(111) and Pd/WC(0001) surfaces via the carbon atom, except that adsorbed CH_3CHO bound on the surfaces through both carbon and oxygen atoms.

As compared in Table 6.1, calculated binding energies of adsorbed intermediates from ethanol decomposition were lower on the Pd/WC(0001) surface than on Pd(111). Pd was susceptible to poisoning by CO and carbonyl-containing intermediates.[6,9,10,33,34] DFT calculations showed that the CO binding energy was significantly lower on Pd/WC(0001) (-1.36 eV) than on Pd(111) (-1.98 eV), thereby suggesting that the Pd/WC surface should have a higher tolerance against CO poisoning. Similar to the observed trend for CO binding on the two surfaces, the lower binding energies of the adsorbed carbonyl-containing intermediates on the Pd/WC(0001) surface should alleviate intermediate poisoning of the active sites as well.

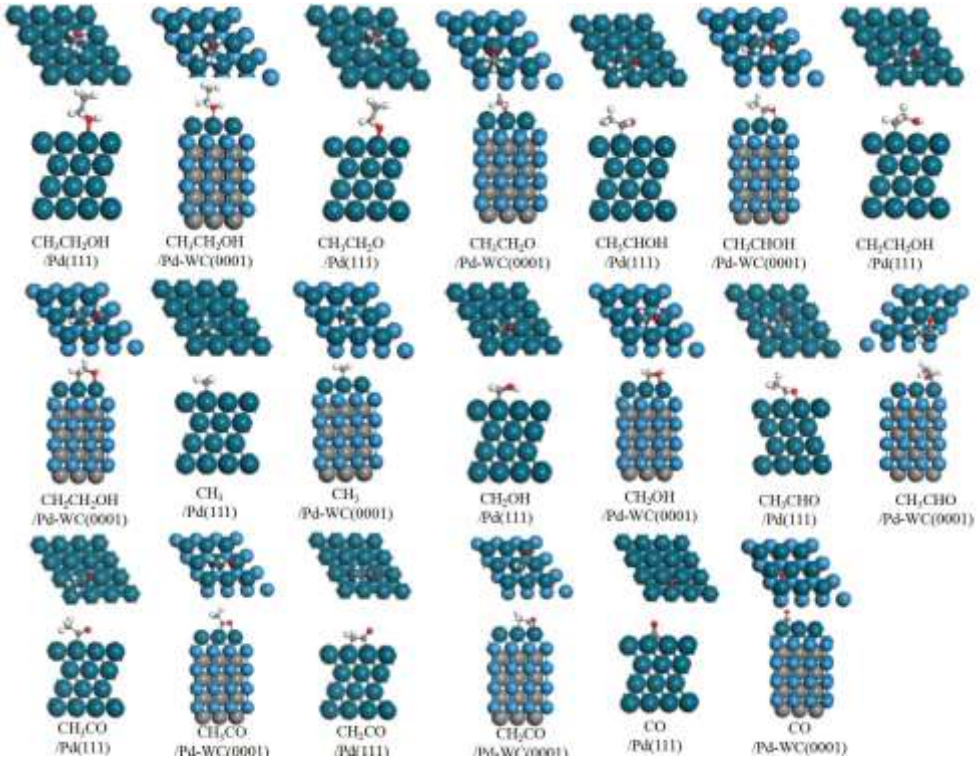

Figure 6.7 The adsorption configurations of ethanol and adsorbed intermediates from ethanol decomposition on Pd(111) and Pd/WC(0001) surfaces.

Table 6.1 DFT calculations of binding energies (eV) of CH_3CH_2OH, CH_3CH_2O, CH_3CHOH, CH_2CH_2OH, CH3, CH_2OH, CH_3CHO, CH_3CO, CH_2CO, CO on Pd(111) and Pd/WC(0001) surfaces.

Species	Binding Configurations	Binding energies/eV	
		Pd(111)	Pd/WC(0001)
CH_3CH_2OH	atop, O-bound	-0.3	-0.58
CH_3CH_2O	atop, O-bound	-1.55	-2.31
CH_3CHOH	atop, C_α-bound	-2.12	-2.05
CH_2CH_2OH	atop, C_β -bound	-2.28	-1.98
CH_3	atop, C-bound	-2.38	-2.24
CH_2OH	atop, C-bound	-2.25	-2.17
CH_3CHO	atop, C-bound and O-bound	-0.29	-0.16
CH_3CO	atop, C-bound	-2.14	-1.86
CH_2CO	bridge, C-bound	-1.14	-0.97
CO	fcc, C-bound	-1.98	-1.36

6.3.2 Surface science study of ethanol decomposition on WC and Pd/WC

6.3.2.1 TPD of ethanol reactions on WC and Pd/WC

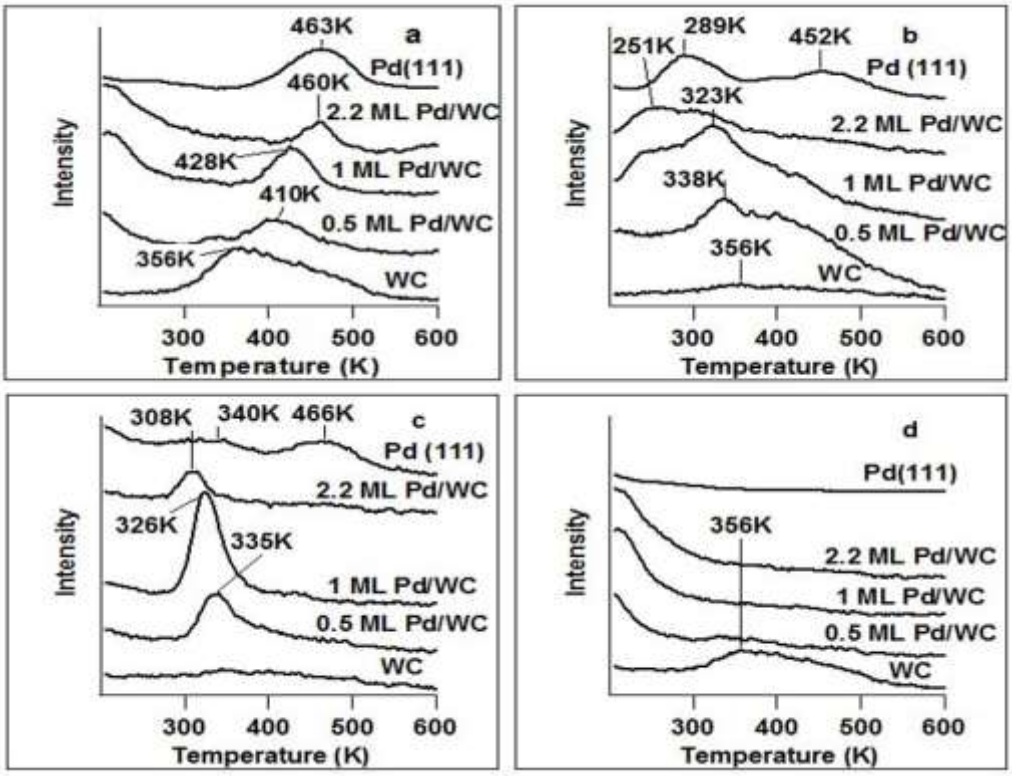

Figure 6.8 TPD spectra of (a) CO or C_2H_4, (b) H_2, (c) CH_4 and (d) C_2H_4 following a 2 L exposure of C_2H_5OH.

TPD experiments with 2 Langmuir (1L= 10^{-6} Torr·s) ethanol dosed at 100 K were conducted to examine the selectivity and activity of ethanol decomposition on unmodified WC and Pd-modified WC surfaces with different Pd coverages. The detection of various products in the TPD measurements indicated that ethanol decomposed via the following reaction pathways:

1. $aC_2H_5OH \rightarrow aCO + 3aH_2 + aC_{ad}$ (Reforming)
2. $bC_2H_5OH \rightarrow bCO + bCH_4 + bH_2$ (Methane Production)
3. $cC_2H_5OH \rightarrow 2cC_{ad} + cO_{ad} + 3cH_2$ (Complete Decomposition)
4. $dC_2H_5OH \rightarrow dC_2H_4 + dH_2 + dO_{ad}$ (Ethylene Production)

Where a-d were the amounts of chemisorbed ethanol decomposing via each given reaction pathway. The reforming pathway was desirable because the selective C-H and C-C bond breakage

was consistent with the first step of the proposed EOR mechanism[7] on the Pd surface while the C-O bond remained intact.

Fig.6.2 illustrated that the desorption temperatures of the decomposition products were generally lower on Pd-modified WC, compared with those on the Pd surface. For example, the CO desorption temperature was 410K on 0.5 ML Pd/WC, about 50K lower than that on the Pd(111) surface, as shown in Fig.6.2a. This indicated that CO bound more weakly on Pd-modified WC than on Pd(111), consistent with the DFT results of CO binding energies for the two surfaces (Table 6.2). The CO desorption temperature increased with an increase in Pd coverage, indicating that Pd/WC behaved more like Pd bulk at higher Pd coverages.

In addition to the desorption of CO, H_2 desorption (Fig.6.2b) occurred on all the surfaces while the desorption of CH_4 (Fig.6.2c) occurred only on Pd-modified WC surfaces. The C_2H_4 desorption peak was only detected on the unmodified WC surface at 356K (Fig.6.2d), indicating that the WC surface was selective toward the C-O bond scission.

The TPD peak areas were quantified for each product based on procedures described previously[35] and the results were summarized in Table 6.2. The unmodified WC surface was primarily selective toward the cleavage of the C-O bond, leading to undesired ethylene production as the dominant reaction pathway. The undesired C-O bond scission was significantly reduced on Pd-modified WC surfaces. Instead, the C-C bond scission became the primary reaction pathway, as indicated by the reforming, methane production and total decomposition pathways. Among all samples, the 0.5 ML Pd/WC surface showed the highest overall activity, as well as the highest selectivity toward the reforming reaction pathway. The 1 ML Pd/WC surface was completely inactive toward the undesired pathway of ethylene production. The TPD results of the Pd/WC

surfaces showed the same trend of blocking the C-O bond scission pathway of WC, similar to previous TPD results of modifying WC with Pt[35] and Rh[36].

Table 6.2 Activity and selectivity of ethanol on WC and Pd-modified WC surfaces

Ethanol Activity (ML)					
Surface	Reforming	CH_4	Decomposition	Ethylene	Total
Pd(111)	0.105[37]	0.112[37]	N/A[37]	0[37]	N/A[37]
WC	0	0	0.030	0.064	0.094
0.5 ML Pd/WC	0.025	0.004	0.179	0.004	0.212
1 ML Pd/WC	0.015	0.006	0.112	0	0.133
2 ML Pd/WC	0.008	0.001	0.093	0	0.102

6.3.2.2 HREELS of ethanol decomposition on WC and Pd/WC

Fig.6.3 illustrated the HREELS spectra on the unmodified WC and Pd-modified WC surfaces with 2 Langmuir ethanol dosed at 100K, followed by heating each surface to temperatures between 100K and 500K. The HREELS peak assignments of ethanol on WC and Pd-modified WC were listed in Table 6.3. Unlike a previous study of methanol decomposition on the Pd/WC surface,[38] in which a mixture of methoxy and methanol were both observed on Pd/WC surfaces, ethoxy was the only species identified on all examined surfaces from ethanol decomposition. This was based on the absence of the OH stretching mode around 3300 cm^{-1}, indicating the decomposition of ethanol on the WC and Pd/WC surfaces at 100K.

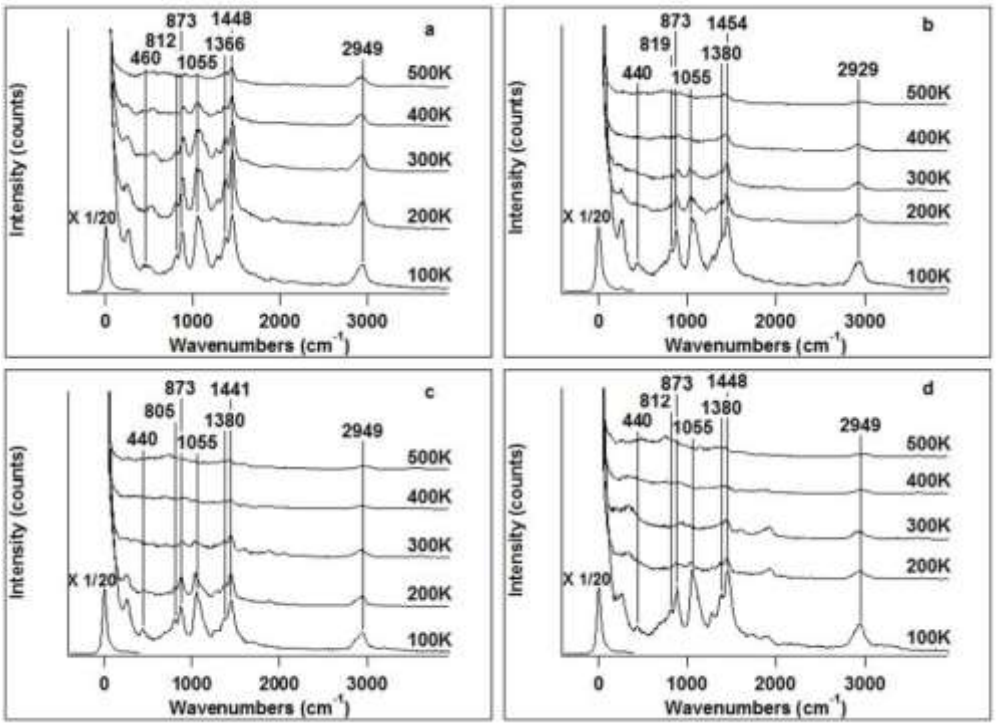

Figure 6.3 HREELS spectra of (a) WC, (b) 0.5 ML Pd/WC, (c) 1 ML Pd/WC, and (d) 2 ML Pd/WC.

On the unmodified WC surface (Fig.6.3a), ethoxy reacted at 400K when the C-C-O bond stretching modes at 873 and 1055 cm^{-1} started disappearing and leaving only CH_x. This was consistent with the TPD detection of the C_2H_4 desorption peak on the WC surface at 356K (Fig.6.2a). Pd-modified WC surfaces (Fig.6.3b, c and d) showed that the ethoxy reacted at temperatures as low as 200K, as indicated by the decrease of the ethoxy vibrational peak intensities with increases in temperatures beginning from 200K. Additionally, temperatures corresponding to the disappearance of the C-C-O stretching peaks began to decrease along with an increase in Pd coverage. The Pd-modified WC surfaces showed similar ethoxy reaction temperatures as the more expensive Pt-modified WC surface[39]. In general, the TPD and HREELS results illustrated that unmodified WC would not be an effective catalyst for EOR due to the high selectivity toward C-O bond scission. However, modifying the WC surface with only atomic thickness of Pd allowed the activation of ethoxy to occur at dramatically lower temperatures toward the cleavage of the C-

C and C-H bonds. Based on the promising DFT, TPD and HREELS results on model Pd/WC surfaces, power catalysts were synthesized and examined for EOR activity and stability in alkaline, as described below.

Table 6.3 HREELS assignments with vibrational frequency listed in cm^{-1}

Mode	Gas[40]	Solid[41]	Pd(111) [42]	WC	Pd/WC
ν(OH)	3660	3676			n. r.
$\nu_{as}(CH_3)$	2965, 2880	2989, 2943	n. r., 2925	2943	2949
$\nu(CH_2)$		2900	2925		
ν(CO)				2043	2043
$\delta(CH_2)$	1450	1490	1465		
$\delta as(CH_3)$	1390	1452, 1394	1465, 1400	1448,1366	~1450, 1380
νa(CCO)	1060	1089	1040	1055	1055(1042)
νs(CO)	1033	1030			
νs(CCO)	880	885	855	873	~873
$\gamma(CH_2)$		801	745	812	~819
δ(CCO)		419	450	460	440

6.3.3 Electrochemical evaluations of Pd-modified WC/C catalysts for alkaline EOR

6.3.3.1 Electrochemical measurements

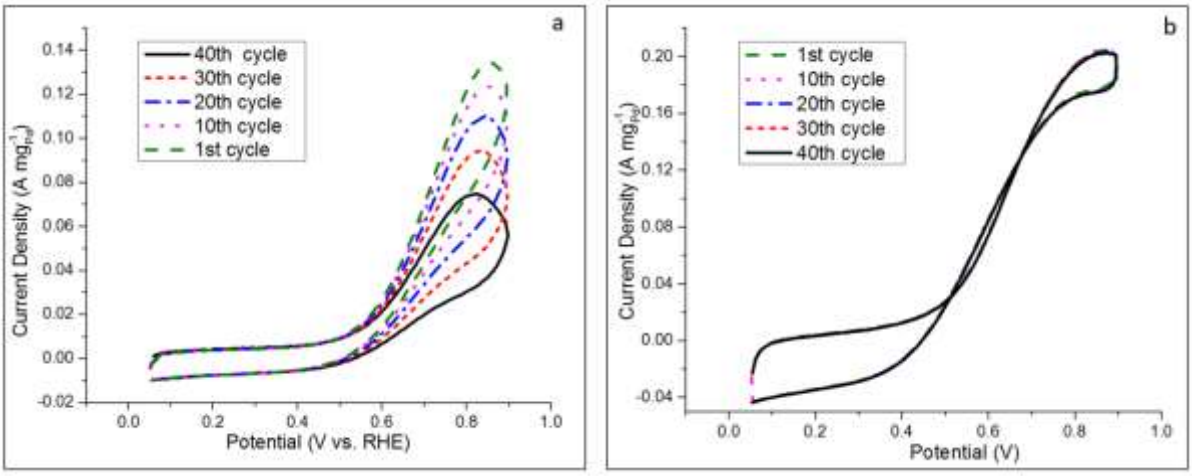

Figure 6.4 CVs of selected cycles from 1st to 40th cycle for (a) 5 wt% Pd/WC/C-iwi in and (b) 5 wt% Pd-WC/C-op in 0.1M KOH/ 1M ethanol.

As shown in Fig.6.4, CV measurements were performed to examine the EOR stability of 5 wt% Pd/WC/C-op and 5 wt% Pd-WC/C-iwi in 0.1M KOH/1M EtOH. The mass current density was normalized by the Pd loading in each sample. The EOR mass current density (Fig.6.4a) for 5 wt% Pd/WC/C-iwi decreased with an increase in the CV scanning cycle from 1st to 40th cycles. This indicated poor EOR stability of 5 wt% Pd/WC/C-iwi, which was synthesized from the conventional iwi method. In contrast, 5 wt% Pd-WC/C-op resulted in no degradation in mass current density after 40 CV cycles, demonstrating high stability for the catalyst made from the "one-pot" wet impregnation synthesis procedure.

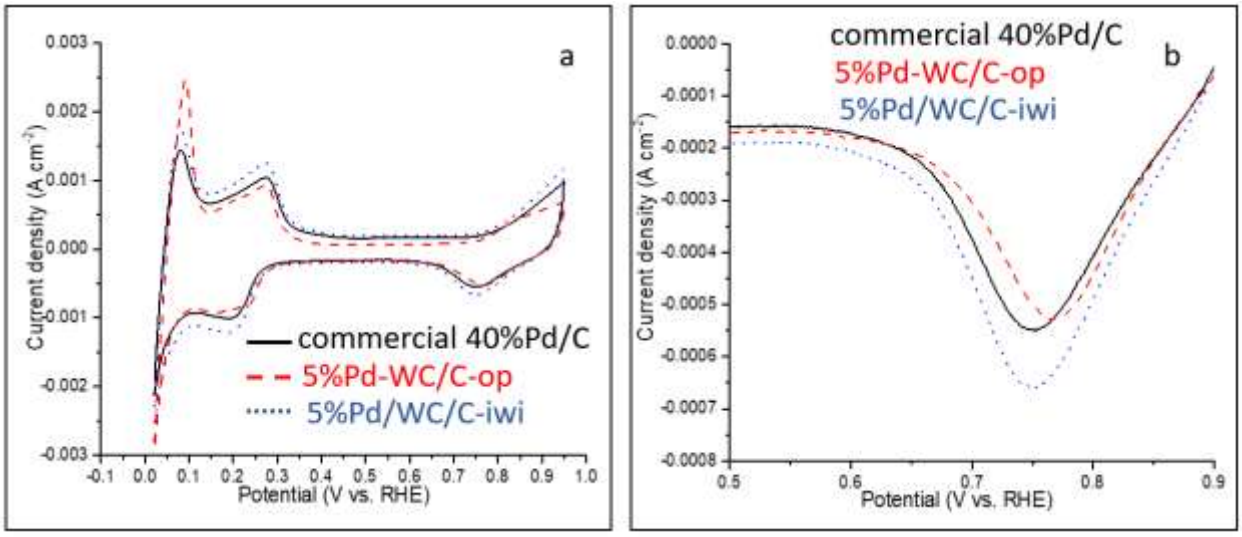

Figure 6.5 (a) CV recorded at a scanning rate of 50mV s^{-1} in Ar-saturated 0.5 M H_2SO_4 for 5 wt% Pd-WC/C-op indicated in red dashed line, 5 wt% Pd/WC/C-iwi indicated in the blue dotted line and commercial 40 wt% Pd/C in the black solid line; (b) ECSA of each catalyst determined by a cathodic peak in a range from 0.9 V to 0.5V vs. RHE. The current density (A cm^{-2}) for 5 µg Pd loadings and normalized by the geometric surface area (0.196cm^2) of the glassy carbon electrode.

CV scans for catalysts samples in Ar-saturated 0.5 M H_2SO_4 are shown in Fig.6.5a. The cathodic peaks from a Pd-O region from 0.9V to 0.5V vs. RHE (Fig.6.5b) were used for determining the Pd ECSA for all samples. The monolayer formation only occurred between chemisorbed oxygen with Pd atoms in the Pd-O region for Pd-based powder catalysts, unlike Pt-based catalysts using Pt-H region for determining Pt ECSA[29,43]. ECSA of commercial 40 wt% Pd/C was determined to be 12.5 m^2/g, which was similar to the result reported in literature[44,45]. The ECSA of 5 wt% Pd-WC/C-op and 5 wt% Pd/WC/C-iwi was 11.0 and 15.1 m^2/g, respectively.

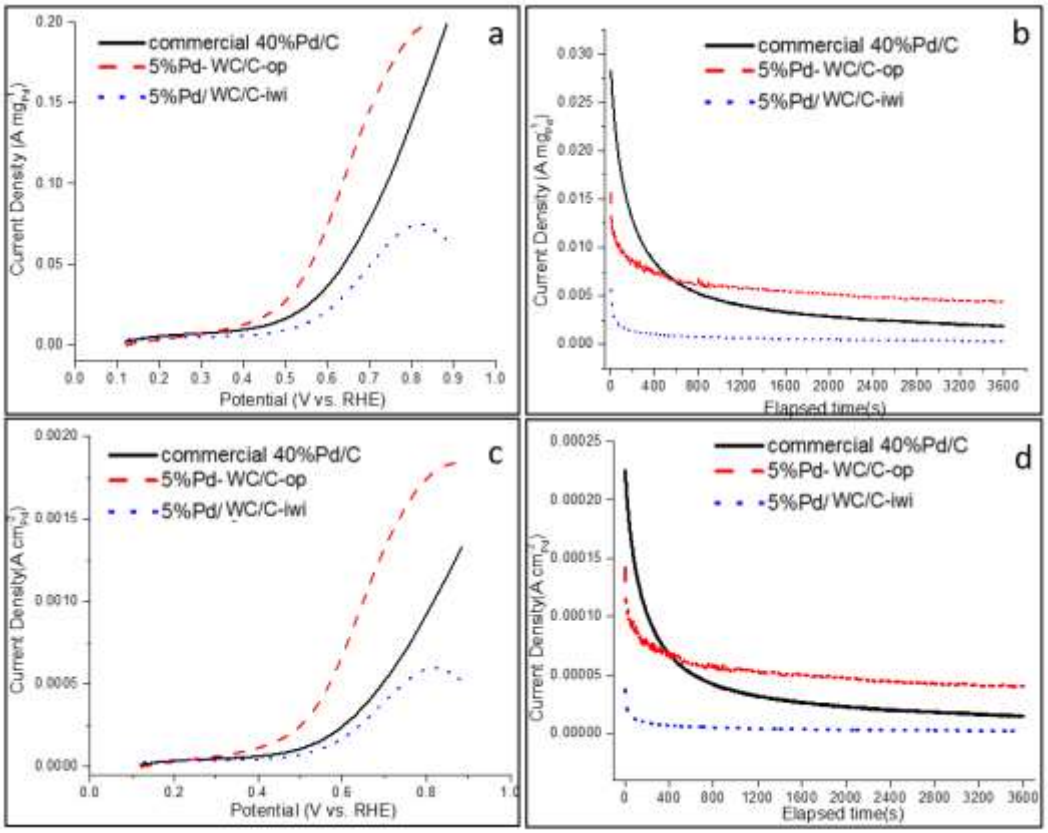

Figure 6.6 LSV EOR testing in 0.1M KOH/1M EtOH for the benchmark 40 wt% Pd/C with the solid black line, the 5 wt% Pd-WC/C-op indicated with the red dashed line and the 5 wt% Pd/WC/C-iwi with the blue dotted line with (a) mass current density normalized by their respective Pd loading EOR and (c) specific current densities normalized by their respective ECSA; CA testing at 0.6 V vs. RHE for one hour performed in 0.1M KOH/1M EtOH with (b) mass current density normalized by their respective Pd loading and (d) specific current density normalized by their Pd ECSA.

LSV and CA measurements in 0.1M KOH/1M EtOH were performed to examine the EOR activity of the prepared samples and compare them with the benchmark 40 wt% Pd/C catalyst, shown in Fig.6.6. The current density was normalized by the catalyst Pd loadings (Fig.6.6a and b) and by the Pd ECSA (Fig.6.6c and d). The current density for benchmark 40 wt% Pd/C at 0.6 V vs. RHE was 35 mA mg^{-1} (Fig.6.6a), similar to the results reported in literature[46–48]. The LSV current density for 5 wt% Pd-WC/C-op was higher than both 40 wt% Pd/C and 5 wt% Pd/WC/C-iwi. At a potential of 0.6V vs. RHE, the EOR mass current density was approximately twice that of commercial 40%Pd/C (Fig.6.6a), while the specific current density was almost three times

higher than the benchmark catalyst (Fig.6.6c). To compare the steady-state activity at 0.6V vs. RHE, the mass and specific activity of all tested catalysts from the CA measurements (Fig.6.6b and 6d) showed the same trend as observed in LSV testing. After CA measurements at 400 seconds, the activity corresponding to 5%Pd-WC/C-op surpassed that of commercial 40%Pd/C. The high activity for 5%Pd-WC/C-op became more evident as the test time elapsed, indicating its high EOR stability in alkaline electrolyte.

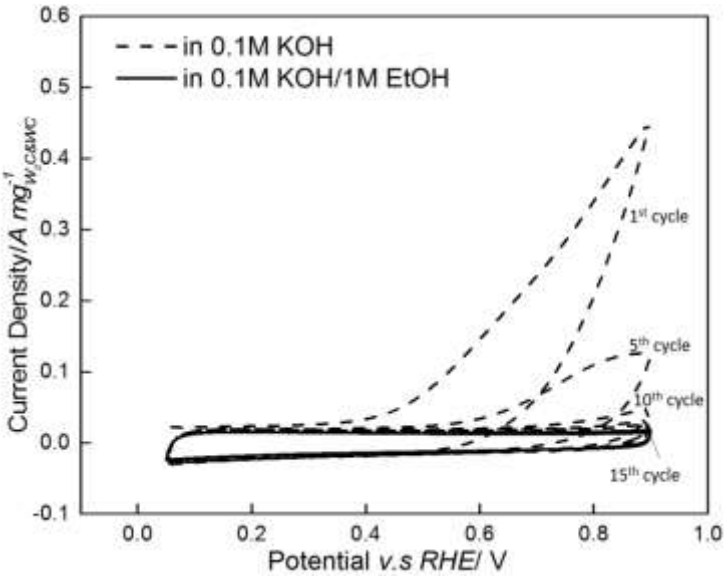

Figure 6.7 CVs for unmodified WC/C in 0.1M KOH shown in the dash line followed by CVs in 0.1M KOH/ 1M EtOH in solid black lines.

In order to understand the underlying reasons for the different activity and stability among the synthesized samples, unmodified WC/C, used as the substrate to synthesize 5 wt% Pd/WC/C-iwi, was examined by alkaline EOR CV testing. According to Fig.6.7, the oxidation current density for unmodified WC/C started at approximately 0.4V vs. RHE in alkaline electrolyte (dotted line), suggesting that unmodified WC underwent oxidation starting from 0.4V in alkaline environment. The WC oxidation process was irreversible. The anodic oxidation peaks shrank with an increase in the number of CV cycles, which may have been due to the continued dissolution of passivated

tungsten oxides that occurred at potentials above 0.8 V.[49] Since 5 wt% Pd/WC/C-iwi was synthesized from incipient wetness impregnation of the Pd precursor on the synthesized WC/C substrate, the observed low EOR stability (Fig.6.4a) could be attributed to WC oxidation and further dissolution of tungsten oxides. This process could further result in Pd particles loss, thus resulting in a decrease in current density with increases in the number of the CV cycles. The high stability obtained by 5 wt% Pd-WC/C-op could be attributed to the direct chemical bond formation between Pd atoms and WC during the "one-pot" synthesis.[10]

6.3.3.2 In-situ IRRAS evaluation coupled with LSV measurements

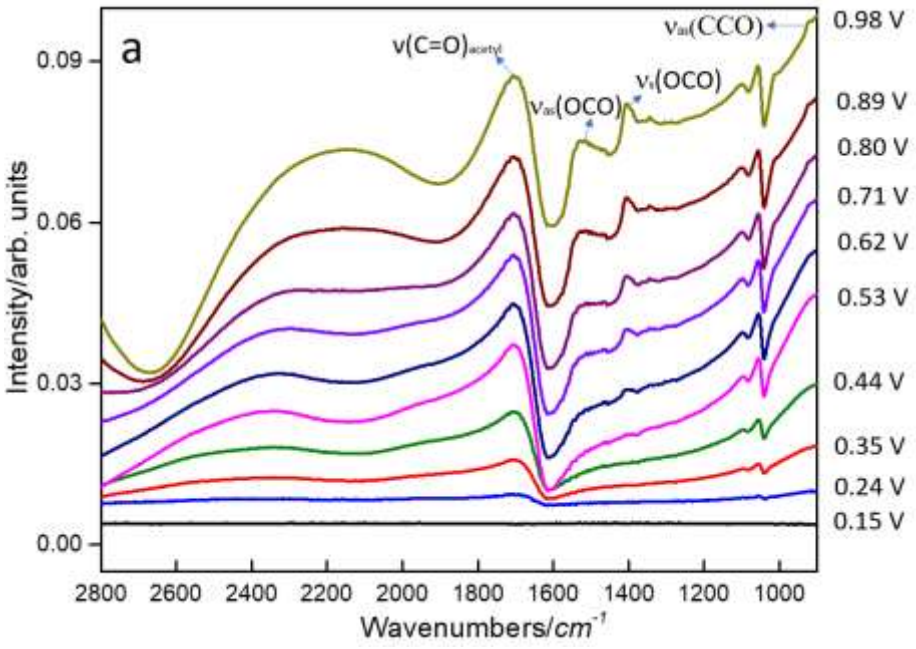

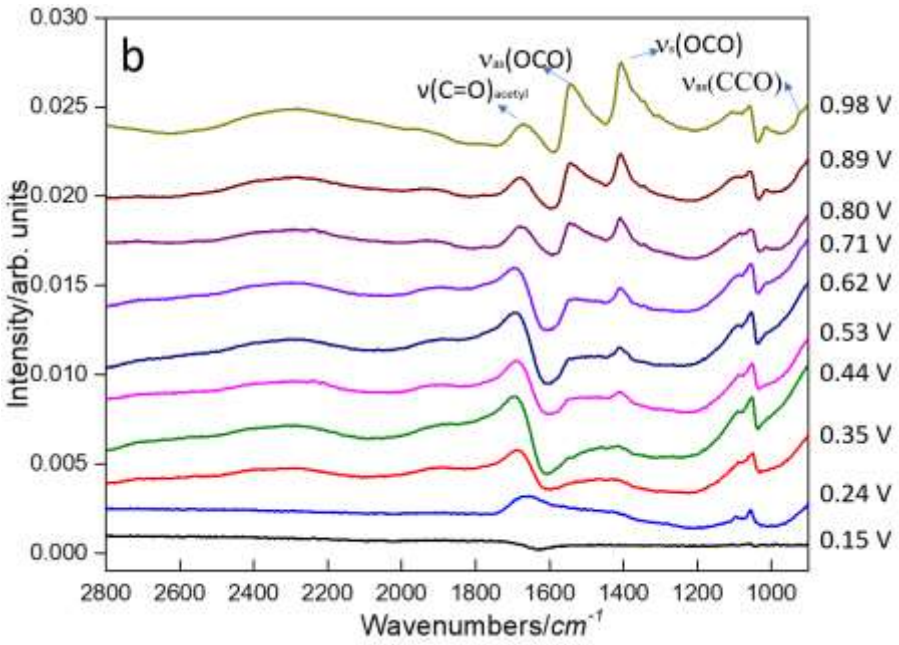

Figure 6.8 *In-situ* IRRAS spectra of 40 wt% Pd/C (a) and of 5 wt% Pd-WC/C-op (b) collected in 0.1M KOH/1M EtOH coupled with LSV testing at a scan rate of 1mV s^{-1}.

In-situ IRRAS-LSV measurements were performed on 40 wt% Pd/C (Fig.6.8A) and 5 wt% Pd-WC/C-op (Fig.6.8B) in alkaline electrolyte. For the benchmark 40% Pd/C catalyst, consistent to the literature[50], acetate (CH_3COO^-) was identified by peaks of ν_{as}(O-C-O) at 1550 cm^{-1} and ν_S(O-C-O) at 1415 cm^{-1} as one of the main C_2 products in alkaline. The vibrational peak of ν_{as}(O-C-O) at 933 cm^{-1} was attributed to acetaldehyde (CH_3CHO). Peak assignments are summarized in Table 6.4. The C_2 product peaks started being detected at the potential of 0.62 V for 40 wt% Pd/C. For 5 wt% Pd-WC/C-op, the onset potential was 0.44 V, which was approximately 0.2 V lower than that the benchmark Pd/C catalyst. However, their carbonyl intermediates, ν(C=O) between 1610-1640 cm^{-1}, started being detected at the same potential of 0.24 V for both catalysts. Therefore, consistent with the DFT and surface science conclusions, the Pd-modified WC catalyst bound to the reaction intermediates more weakly, potentially resulting in less catalyst poisoning by the EOR intermediates.

Table 6.4 peak assignments for the *in-situ* IRRAS spectra

Wave number/cm^{-1}	Vibrational normal mode	Reference
1610-1640	C=O stretching (ν) of adsorbed acetaldehyde and acetyl	[50,51]
1550	O-C-O asymmetric stretching(ν_{as}) of acetate in solution	[13]
1415	O-C-O symmetric stretching (ν_{s}) in acetate	[13,51]
1355/ 1368	CH_3 symmetric deformation in CH_3CHO	[51–53]
~1348/1383	CH in-plane bending mode (ρ) of adsorbed acetate/ acetate in solution	[13,51,54]
1044	C-O stretching (ν) of CH_3CH_2OH	[55]
933	C-C-O asymmetric stretching (ν_{as}) of CH_3CHO	[51,56]

6.4 Conclusions

DFT calculations demonstrated that the intermediates from ethanol decomposition bound more weakly on Pd/WC(0001), suggesting that this surface should be more tolerant to the poisoning effect from the adsorption of intermediates. The TPD and HREELS experiments on the model surfaces revealed that the desorption temperature for detected intermediates from ethanol decomposition were lower on Pd-modified WC than Pd bulk, confirming the potential of using Pd/WC as an EOR catalyst. Electrochemical evaluations of powder catalysts illustrated that the 5 wt% Pd-WC/C-op catalyst resulted in a higher EOR activity in alkaline than the benchmark 40 wt% Pt/C catalyst. The enhanced stability of the 5 wt% Pd-WC/C-op was obtained via the "one-pot" synthesis procedure compared to 5 wt% Pd/WC/C-iwi made from the conventional iwi synthesis method. The electrochemical stability of 5 wt% Pd-WC/C-op was primarily attributed to the chemical bonding formation between Pd and WC during the high-temperature carburization process. *In-situ* IRRAS revealed that the enhanced EOR activity for 5 wt% Pd-WC/C-op was

attributed to the weaker bonding of surface intermediates. Overall, results presented in this study demonstrated the feasibility of designing EOR catalysts from fundamental DFT and surface science studies.

References

(1) Hamnett, A. *Catal. Today* **1997**, *38* (4), 445–457.
(2) Reddington, E.; Sapienza, A.; Gurau, B.; Viswanathan, R.; Sarangapani, S.; Smotkin, E. S.; Mallouk, T. E. *Science (80-.).* **1998**, *280* (5370).
(3) Song, S.; Zhou, W.; Liang, Z.; Cai, R.; Sun, G.; Xin, Q.; Stergiopoulos, V.; Tsiakaras, P. *Appl. Catal. B Environ.* **2005**, *55* (1), 65–72.
(4) Akhairi, M. A. F.; Kamarudin, S. K. *Int. J. Hydrogen Energy* **2016**, *41* (7), 4214–4228.
(5) Song, S.; Tsiakaras, P. *Appl. Catal. B Environ.* **2006**, *63* (3–4), 187–193.
(6) Rousseau, S.; Coutanceau, C.; Lamy, C.; Léger, J.-M. *J. Power Sources* **2006**, *158* (1), 18–24.
(7) Wang, Y.; Zou, S.; Cai, W.-B. *Catalysts* **2015**, *5* (3), 1507–1534.
(8) Alonso, E.; Field, F. R.; Roth, R.; Kirchain, R. E. In *2009 IEEE International Symposium on Sustainable Systems and Technology*; IEEE, 2009; pp 1–6.
(9) Spendelow, J. S.; Goodpaster, J. D.; Kenis, P. J. A.; Wieckowski, A. *J. Phys. Chem. B* **2006**, *110* (19), 9545–9555.
(10) Lin, L.; Sheng, W.; Yao, S.; Ma, D.; Chen, J. G. *J. Power Sources* **2017**, *345*, 182–189.
(11) Tackett, B. M.; Sheng, W.; Chen, J. G. *Joule* **2017**, 1–11.
(12) Antolini, E. *J. Power Sources* **2007**, *170* (1), 1–12.
(13) Zhou, Z.-Y.; Wang, Q.; Lin, J.-L.; Tian, N.; Sun, S.-G. *Electrochim. Acta* **2010**, *55* (27), 7995–7999.
(14) Shen, P. K.; Xu, C. *Electrochem. commun.* **2006**, *8* (1), 184–188.
(15) Fang, X.; Wang, L.; Shen, P. K.; Cui, G.; Bianchini, C. *An in situ Fourier transform infrared spectroelectrochemical study on ethanol electrooxidation on Pd in alkaline solution*; **2010**.
(16) Antolini, E.; Cooper, B. H.; Trejo, J. M.; Mariscal, R.; Fierro, J. L. G.; Xin, Q.; Kwak, C.; Akins, D. L. *Energy Environ. Sci.* **2009**, *2* (9), 915.
(17) Mellinger, Z. J.; Weigert, E. C.; Stottlemyer, A. L.; Chen, J. G. *Electrochem. Solid-State Lett.* **2008**, *11* (5), B63.
(18) Mellinger, Z. J.; Kelly, T. G.; Chen, J. G. *ACS Catal.* **2012**, *2* (5), 751–758.
(19) Moraes, L. P. R.; Matos, B. R.; Radtke, C.; Santiago, E. I.; Fonseca, F. C.; Amico, S. C.; Malfatti, C. F. *Int. J. Hydrogen Energy* **2016**, *41* (15), 6457–6468.
(20) Abdel Hameed, R. M. *J. Colloid Interface Sci.* **2017**, *505*, 230–240.
(21) Qin, Y.-H.; Xiong, Z.-Y.; Ma, J.; Yang, L.; Wu, Z.; Feng, W.; Wang, T.-L.; Wang, W.-G.; Wang, C.-W. *Int. J. Hydrogen Energy* **2017**, *42* (2), 1103–1112.
(22) Kresse, G.; Hafner, J. *Phys. Rev. B* **1993**, *47* (1), 558–561.
(23) Kresse, G.; Joubert, D. *Phys. Rev. B* **1999**, *59* (3), 1758–1775.

(24) Perdew, J. P.; Wang, Y. *Phys. Rev. B* **1992**, *46* (20), 12947–12954.
(25) Mellinger, Z. J.; Kelly, T. G.; Chen, J. G. *ACS Catal.* **2012**, *2* (5), 751–758.
(26) Stottlemyer, A. L.; Ren, H.; Chen, J. G. *Surf. Sci.* **2009**, *603* (16), 2630–2638.
(27) Kimmel, Y. C.; Esposito, D. V.; Birkmire, R. W.; Chen, J. G. *Int. J. Hydrogen Energy* **2012**, *37* (4), 3019–3024.
(28) Yu, W.; Porosoff, M. D.; Chen, J. G. .
(29) Álvarez, G. F.; Mamlouk, M.; Scott, K. *Int. J. Electrochem.* **2011**, *2011*, 1–12.
(30) Sheng, W.; Kattel, S.; Yao, S.; Yan, B.; Liang, Z.; Hawxhurst, C. J.; Wu, Q.; Chen, J. G. *Energy Environ. Sci.* **2017**.
(31) Breiter, M. W. *J. Electroanal. Chem. Interfacial Electrochem.* **1977**, *81* (2), 275–284.
(32) Rand, D. A. J.; Woods, R. *J. Electroanal. Chem.* **1971**, *31* (1), 29–38.
(33) Nørskov, J. K.; Abild-Pedersen, F.; Studt, F.; Bligaard, T. *Proc. Natl. Acad. Sci. U. S. A.* **2011**, *108* (3), 937–943.
(34) Esposito, D. V; Chen, J. G. .
(35) Kelly, T. G.; Stottlemyer, A. L.; Yang, X.; Chen, J. G. *J. Electrochem. Soc.* **2014**, *161* (8), E3165–E3170.
(36) Kelly, T. G.; Stottlemyer, A. L.; Ren, H.; Chen, J. G. *J. Phys. Chem. C* **2011**, *115* (14), 6644–6650.
(37) Davis, J. L.; Barteau, M. A. *Surf. Sci.* **1987**, *187* (2–3), 387–406.
(38) Mellinger, Z. J.; Kelly, T. G.; Chen, J. G. *ACS Catal.* **2012**, *2* (5), 751–758.
(39) Stottlemyer, A. L.; L., A. *Controlling the bond scission sequence of oxygenates for energy applications*; 2010.
(40) Sexton, B. A. *Surf. Sci.* **1979**, *88* (2–3), 299–318.
(41) Barnes, A. J.; Hallam, H. E. *Trans. Faraday Soc.* **1970**, *66* (0), 1932–1940.
(42) Davis, J. L.; Barteau, M. A. *Surf. Sci.* **1990**, *235* (2–3), 235–248.
(43) Senthil Kumar, S. M.; Soler Herrero, J.; Irusta, S.; Scott, K. *J. Electroanal. Chem.* **2010**, *647* (2), 211–221.
(44) Álvarez, G. F.; Mamlouk, M.; Scott, K. *Int. J. Electrochem.* **2011**, *2011*, 1–12.
(45) Wang, F.; Li, C.; Sun, L.-D.; Xu, C.-H.; Wang, J.; Yu, J. C.; Yan, C.-H. *Angew. Chem. Int. Ed. Engl.* **2012**, *51* (20), 4872–4876.
(46) Hu, F. P.; Wang, Z.; Li, Y.; Li, C.; Zhang, X.; Shen, P. K. *J. Power Sources* **2008**, *177* (1), 61–66.
(47) Zheng, H. T.; Li, Y.; Chen, S.; Shen, P. K. *J. Power Sources* **2006**, *163* (1), 371–375.
(48) Bianchini, C.; Shen, P. K. *Chem. Rev.* **2009**, *109* (9), 4183–4206.
(49) Weidman, M. C.; Esposito, D. V.; Hsu, Y.-C.; Chen, J. G. *J. Power Sources* **2012**, *202*, 11–17.
(50) Yang, Y. Y.; Ren, J.; Li, Q. X.; Zhou, Z. Y.; Sun, S. G.; Cai, W. Bin. *ACS Catal.* **2014**, *4* (3), 798–803.
(51) Li, M.; Cullen, D. A.; Sasaki, K.; Marinkovic, N. S.; More, K.; Adzic, R. R. **2012**.
(52) Lai, S. C. S.; Kleijn, S. E. F.; Öztürk, F. T. Z.; van Rees Vellinga, V. C.; Koning, J.; Rodriguez, P.; Koper, M. T. M. *Catal. Today* **2010**, *154* (1), 92–104.
(53) Colmati, F.; Tremiliosi-Filho, G.; Gonzalez, E. R.; Berná, A.; Herrero, E.; Feliu, J. M. *Faraday Discuss.* **2008**, *140*, 379-97-37.
(54) Christensen, P. A.; Linares-Moya, D. *J. Phys. Chem. C* **2010**, *114* (2), 1094–1101.
(55) Plyler, E. K. *J. Res. Natl. Bur. StanJards* **1952**, *48* (4).
(56) Gao, P.; Chang, S.-C.; Zhou, Z.; J. Weaver, M. *J. Electroanal. Chem. Interfacial*

Electrochem. **1989**, *272* (1), 161–178.

7. CONCLUSIONS AND FUTURE DIRECTIONS

7.1 Key findings and contributions summary

Based on HER projects illustrated in chapter three and four, HER experimental investigation on metal-modified TMCs confirms that HBE should be considered as effective descriptor for both PEM and AEM water electrolyzers. Based on EOR studies illustrated in chapter five and six, binding energy of C1 and C2 intermediates from ethanol decomposition can be used for EOR catalysts screening purposes.

More specifically, well-dispersed metal nanoparticles on high surface area nanocrystalline Mo_2C are successfully synthesized and characterized, described in the chapter three. 5%Pt/Mo_2C achieves similar HER mass activity as 40%Pt/C, suggesting Pt loading is successfully reduced by eight times with inexpensive Mo_2C by using this synthesis method. Among non-platinum group metals, Ni/Mo_2C shows promising HER activity. The market price of Ni, being 10,000 times cheaper than Pt, renders Ni/Mo_2C more economically viable, yet Ni/Mo_2C HER mass activity is slightly worse than 5%Pt/Mo_2C. However, the observed activity trend for metal-modified Mo_2C does not exactly follow the trend predicted from DFT calculations, which indicates that synthesized samples should better reflect the theoretical models in order to correlate experimental results with theoretical calculation results more accurately. We are of the opinion that using correlation as the basis for identifying effective descriptors relies upon utilizing well-defined surfaces from well-controlled methods in the synthesis of catalysts. Therefore, in the future, more research efforts should be taken on synthesizing more-well defined power catalytic surfaces modified with atomic thickness metal through advanced synthesis techniques, such as

atomic layer deposition. Pt loading in power form can be further reduced and more accurate DFT prediction should be made. In chapter four, for thin films, well-defined surfaces are synthesized for acid and alkaline HER experiments. As expected, Pt and Au-modified TaC and VC show promising Pt-like acid HER activity and adhere to the previously established acid HER volcano curve. For a library of Pt or Au-modified TMC catalysts, their alkaline activity correlate HBE in a volcano-shape while not showing a strong correlation with OHBE. This suggests the adsorbed hydroxyl group does not directly participate in the rate-determining step of the alkaline HER. Rather, HBE should be considered as a more effective descriptor for governing HER activity in alkaline. This is the first example of a volcano trend on metal-modified carbides for alkaline HER showing that HBE is a good descriptor for this class of materials under both alkaline and acid conditions. We suggest that HBE is appropriate for screening purposes in finding novel HER catalysts suitable in both acid and alkaline electrolytes.

For EOR projects, In chapter five, Pt-modified TaC, in both model thin films and powder catalysts, illustrate higher ethanol oxidation activity and stability relative to Pt. *In-situ* infrared results show higher selectivity towards the highest efficient reaction pathway. DFT calculations suggest enhanced EOR activity obtained on Pt-modified TaC is attributed to enhanced tolerance towards ethanol decomposition intermediates, and a lower activation energy barrier for the highest efficiency reaction pathway. We suggest that the binding energy of intermediates from ethanol decomposition could be considered descriptors for finding active and novel EOR catalysts. In Chapter six, DFT calculations suggest that palladium-modified tungsten carbide exhibits enhanced tolerance toward ethanol decomposition intermediates relative to a Pd surface. Consistent with DFT, desorption temperatures for ethanol decomposition products are lower on the Pd/WC surface than on the Pd surface. Five weight percent (5 wt%) Pd/WC/C powder

catalysts illustrate higher ethanol activity and stability relative to commercial Pd/C in alkaline. *In-situ* infrared reflection absorption spectroscopy results show that 5 wt% Pd-WC/C(op) catalysts have lower EOR onset potential, attributable to the weaker bonding of surface intermediates.

7.2 Publications summary

The four projects described in chapter two to six resulted in two publications and were expected to lead to another two publications:

Zhang, Q., Tackett, B.M., Wu, Q., & Chen, J.G. (2016). "Trends in Hydrogen Evolution Activity of Metal-Modified Molybdenum Carbides in Alkaline and Acid Electrolytes". *ChemElectroChem*. Link: http://doi.org/10.1002/celc.201600171

Zhang, Q., Jiang, Zhao., Liang, Zhixiu., &Chen, J.G. (2018) "Theoretical and Experimental Investigation of Pt-modified TaC as an Electrocatalyst for Ethanol Oxidation in Acid and Alkaline Electrolytes". *AppliedCatalysisB*. Link: https://www.sciencedirect.com/science/article/pii/S0926337318303813

Zhang, Q., Tackett, B.M., Jiang, Zhao., Chen, J.G. "Correlating the Hydrogen Evolution Reaction Activity in Alkaline Electrolytes with the Hydrogen Binding Energy on Metals-Modified Transitional Metal Carbides" *(Under the revision of the American Chemical Society Catalysis)*

Zhang, Q., Mellinger, J. Zachary., Liang, Zhixiu., Chen, J.G. "Pt modified-WC for Ethanol Electrooxidation: from Theoretical Calculation to Electrochemical Evaluations" *(Under the revision of the Journal of Electrochemical Society)*

7.3 A new class of materials exploration: transition metal nitrides (TMNs)

7.3.1 main motivations

Our group has developed strong interest in transition metal nitrides (TMNs) arising out of the following considerations: similar electronic and crystal structures between TMCs and TMNs[1] and clean surfaces without carbonaceous overlayer[2]. We hypothesize that the similarity in electronic and crystal structures between TMCs and TMNs could allow TMNs to inherit Pt-like catalytic properties. Therefore, we began the synthesis of transition metal nitride (TMNs) thin films and the exploration of possible electrochemical applications.

7.3.2 Preliminary results: characterization, hydrogen evolution reaction, stability testing

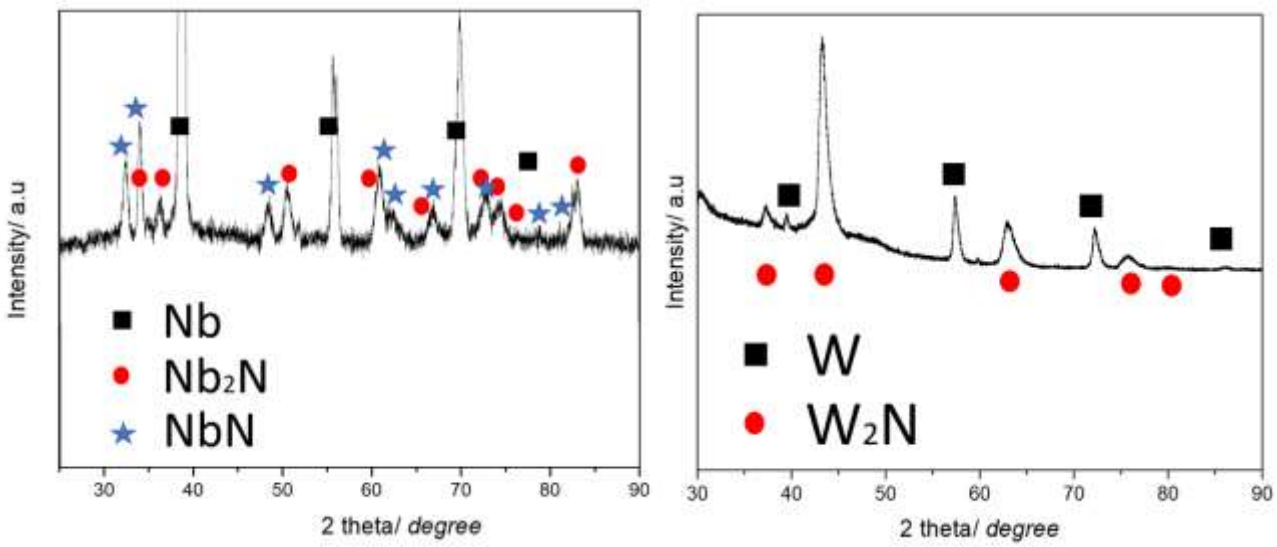

Figure 7.1 GI-XRD patterns of niobium nitride (left) and tungsten nitride (right).

Thus far, we have successfully synthesized niobium (Nb) and tungsten (W) nitride thin films. The samples were characterized by glancing incidence x-ray diffraction (GI-XRD).

Surface-sensitive GI-XRD shows a mixture phase of NbN and Nb_2N for the niobium nitride sample and pure phase W_2N (Fig. 7.1).

Unmodified W_2N and different Pt overlayers-modified W_2N were first measured for HER activity in both acid and alkaline. Due to similarities between the electronic and crystal structures of W_2N and W_2C[1,3], we expect Pt-modified W_2N will demonstrate promising, Pt-like, HER activity. As shown in Fig. 7.2, results of the linear scanning voltammetry (LSV) suggest that HER activity approaches that of Pt foil as Pt coverage on W_2N reaches two or three monolayers, indicating that TMNs could be developed as a promising substrate for HER.

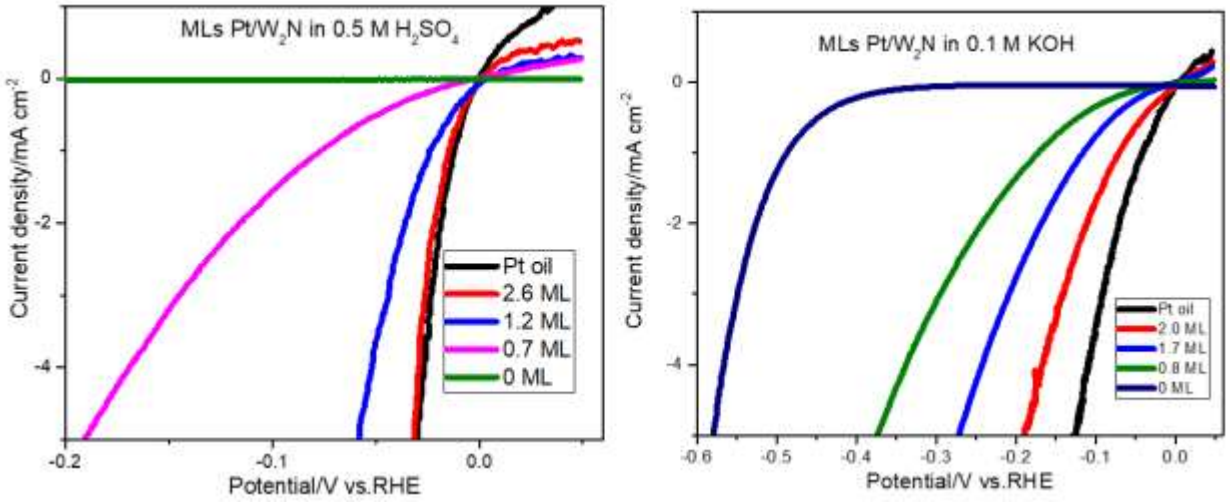

Figure 7.2 HER LSV curves for various MLs Pt-modified W_2N in 0.5 M H_2SO_4 (left) and in 0.1 M KOH (right).

Chrono-potentiometric (CP) titration experiments were conducted on unmodified W_2N as well as a mixture phase of Nb_2N&NbN thin film samples. "Pseudo-Pourbaix" diagrams as a function of pH were generated, as shown in Fig.7.2, including steady-state potential at an applied current of 0 mA and 0.04 mA. The diagrams aim to provide a basic understanding of TMN's stability over a wide range of pH and thus guide the future selections of TMNs for specific electrochemical applications.

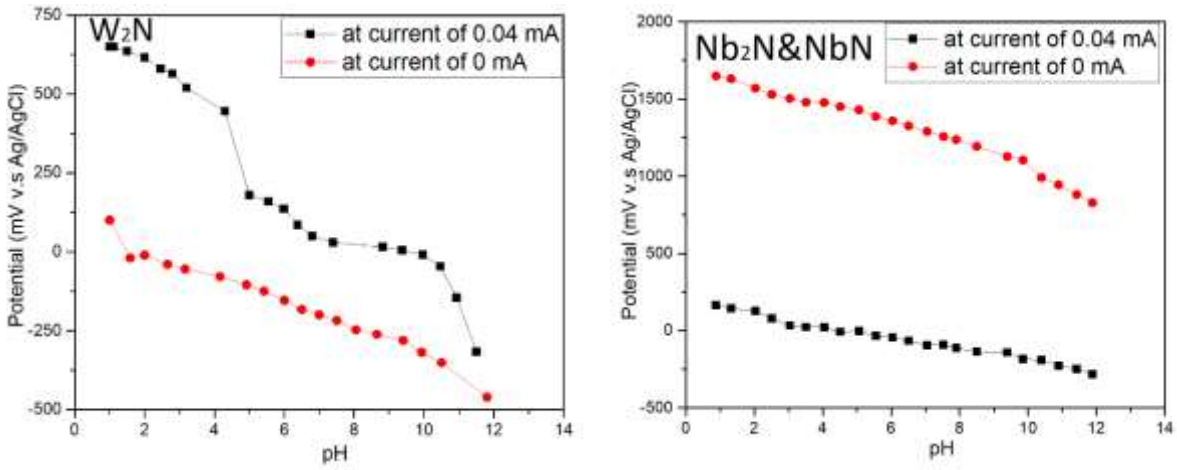

Figure 7.3 Comparison of CP titrations on W_2N (left) and Nb_2N&NbN (right).

At the 0 mA current, the oxidation and reduction reactions on each nitride surface were equal. The curve generated based on steady-state potentials at all selected pHs, was used as a baseline for the open circuit potential. Any applied potentials more negative than the baseline were an indication of the surface's immunity to oxide formation. The other titration curve, corresponding to a 0.04 mA current, can be regarded as the boundary between surfaces with passivation and surfaces with oxidation and dissolution. The region between the open circuit baseline and the passivation/oxidation boundary should be considered as the passivation region. The applied potentials should not exceed the potentials dictated by the passivation baseline. Otherwise, the nitride surface will undergo serious oxidation and degradation. If the applied potential is within the passivation region, the catalytic surface should function without much risk of surface oxidation. Based on the "Pseudo-Pourbaix" diagrams (Fig. 7.3), W_2N and mixture phased niobium nitride are suitable for hydrogen oxidation and reduction reactions as well as methanol and ethanol oxidation reactions. Relative to W_2N, the niobium nitride should be more resistant towards oxidation and contains a larger passivation region, especially in alkaline environment. Therefore, niobium nitride should also be stable under oxygen reduction reactions.

7.3.3 Future work

Preliminary results show that TMNs can be successfully synthesized, and HER activity for Pt-modified TMNs are promising. Two of the TMNs shows high stability, making them ideal candidates for many electrochemical applications. Future efforts should focus on synthesizing a full class of TMNs (e.g., TaN, TaN, TiN, VN, ZrN) and systematically investigating their stability and activity for various electrochemical applications.

References

(1) Guillermet, A. F.; Häglund, J.; Grimvall, G. *Phys. Rev. B* **1993**, *48* (16), 11673–11684.

(2) Lengauer, W. In *Handbook of Ceramic Hard Materials*; Wiley-VCH Verlag GmbH: Weinheim, Germany, **2008**; pp 202–252.

(3) Zhong, Y.; Xia, X.; Shi, F.; Zhan, J.; Tu, J.; Fan, H. J. *Adv. Sci.* **2016**, *3* (5), 1500286.

.